Design Optimisation of a Fabricated Waterjet Transition Duct

A Thesis submitted in partial fulfilment of the requirements for the Degree of

Masters in Engineering

in the University of Canterbury

by Denis V. Gostev

University of Canterbury

2018

Supervisor - College of Engineering Dean (academic) Dr Dirk Pons, University of Canterbury

Co-supervisor - Associate Professor Dr Digby Symons, College of Engineering, University of Canterbury

Industry Mentor - Principal Engineer Mladen Meduric, CWF Hamilton & Co. Ltd

---

Acknowledgements

I would first like to thank the CWF Hamilton & Co, Ltd, under the administration of Ben Reed, for financial support and providing resources and time for this study.

I would like to thank my thesis supervisor associate professor Dirk Pons of the College of the Canterbury University. Dirk always provided expertise, clear guidance and support at all stages. He also helped me to look to the research problem from different perspectives.

I would also like to thank the HamiltonJet expert Mladen Meduric, who diligently shared his deep knowledge of finite element analysis and provided expertise in manufacturing processes.

I would also like to acknowledge the help provided by the fabrication department of HamiltonJet, who provided support, facilities and resources in order to prepare samples. In particular, I would like to thank Thomas Donachie for his professionalism in welding of test samples and his great attitude.

Finally, this work would not have happened without great support and effort of my family.

Document version: Gostev_Denis_Methesis V22.Docx

Date: 27 August 2018

Abstract

Context – One of the key elements of the waterjet system is the *transition duct*, which provides the key structural interface between the boat hull and the waterjet inlet and pump. There is a potential issue with inadequate stiffness in the duct region, which may have reliability implications.

Need – There is a need to determine the optimum arrangement for the stiffeners that are required to reinforce the transition duct, considering all loads, ship classification society requirements for stress, installation constraints and manufacturing considerations such as weld types, weld access and stiffener profiles.

Approach – A finite element analysis was used to address the needs of stiffening the roof-plate and optimise the arrangement and geometry of stiffeners. The risk of metallurgical damage due to weld-on-weld was investigated by examination of the grain morphology using optical microstructure test in conjunction with hardness test. A risk management method was used to estimate the financial cost for solution implementation.

Findings – The study found significant roof-plate deflection caused by negative pressure generated by water flow. Therefore, the application of three stiffening plates is necessary to reduce this deflection. An arrangement of the stiffeners is unique to transition duct for the HT810 waterjet and the spacing between stiffeners is not equal. A fatigue endurance of the welded details is significantly influenced by the geometry of the stiffeners. The optimum geometry of the stiffeners was determined and adequate fatigue life was illustrated.

Implications – There are several important implications revealed for HamiltonJet production practices as well as for installation techniques for the shipyards. Firstly, there is a need to regularly monitor the weld quality at the HamiltonJet production line. This might be done by performing microstructural testing of the weld regions using techniques developed in this study. Quality of the welds might be improved by applying the weld toe grinding method as advised by DNV-GL guidelines. Secondly, there is the importance of analysing and including the detailed pressure distribution for each jet model during the optimisation of stiffening the transition ducts. Finally, the additional stiffening of the roof-plate by shipyards at the jet installation stage is no longer required and any field modifications to the transition duct must be consulted with HamiltonJet.

Contents

List of Figures

List of Tables

1. Introduction

1.1 Background

HamiltonJet pioneered the development of the modern marine waterjet propulsion system over 60 years ago. Since then, a wide range of waterjet models have been developed and extensive design and applications experience gained in a variety of high speed marine craft. With the advent of accessible computer-aided engineering tools such as general purpose computational fluid dynamics (CFD) codes, finite element (FE) analysis (FEA) and optimisation packages, opportunities exist to optimise the product for durability, manufacturability, installability and cost in order to meet new and changing customer demands and internal business interests.

One of the key elements of the waterjet system is the *transition duct* (Figure 1), which provides the key structural interface between the boat hull and the waterjet inlet and pump.

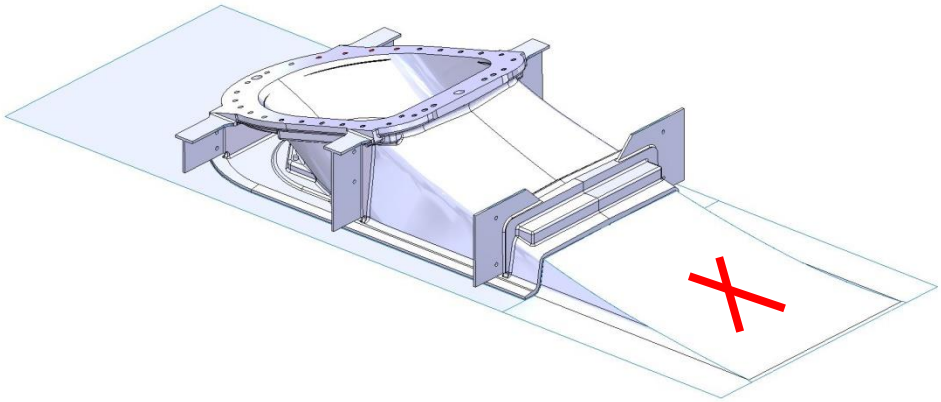

Figure 1. Transition Duct. The roof transition plates are denoted X.

The transition duct provides the lower section of the water inlet and transmits the waterjet loads to the hull via the bottom plate perimeter and various structural webs. The roof of the duct (marked with red cross in Figure 1) experiences low pressures from the momentum change of the incoming flow, and also from major intake screen blockages (e.g. from plastic bags, seaweed, etc.).

1.2 Problem

The background to this problem is that the water loads on the transition duct have in the past been estimated from first principles, and assumed to be relatively low. Hence, the design uses flat plates at the roof transitions, without reinforcement. However, the fluid loads can be highly cyclic and vary with power input and boat speed. There is a potential issue with lack of stiffness in the duct region, which may have reliability implications.

More recently it has become possible to apply CFD analysis to the water flow in the inlet. Consequently, the pressure loads can now be determined with greater precision than before, and are considered along with the principal thrust loads/reaction.

In-field failures of the inlet have not been observed. Nonetheless, the specific inlet duct under investigation was designed and first installed in 2010. The warranty period is 20 years – a considerable time period. This means that there is no product that has yet reached the warranty time life. There is insufficient empirical field data to validate the robustness of the current design that uses an unreinforced roof plate.

Another issue for HamiltonJet is that during an installation process, shipyards tend to layer their own stiffening ribs for added reinforcement. This means that HamiltonJet has limited control over such modifications as well as the quality of the fabrication. This can potentially reduce the service life of the intake and compromise the safety of the entire vessel. HamiltonJet covers its waterjets with a warranty and therefore any intrusion into the original construction of the jet is undesirable.

There is a need to improve the design of the roof plate, particularly against fatigue failure under cyclic negative pressure loads.

Structural elements on the transition duct such as roof plate stiffeners may not be optimum once the CFD pressures are applied, particularly for the high-speed case. Also, the optimum arrangement for stiffeners may not be desirable for the vessel hull structure as they may interfere with the bulkheads and frames of the hull that pass across, and are sometimes attached to, the transition duct roof.

1.3 Research question

There is a need to determine the optimum arrangement for the stiffeners that are required to reinforce the transition duct, considering all loads, ship classification society requirements for stress, installation constraints and manufacturing considerations such as weld types, weld access and stiffener profiles. Transition ducts are manufactured in two material types – aluminium and steel – in alloys that are compatible with vessel hull material.

1.4 Complexity

The complexity arises due to stiffening plates being welded to the transition ducts and the assumption that the first failure will be in the welds. The FEA model has to incorporate Classification Society guidelines on detailing of the applicable weldment types, which provides for an adequate method of stress extraction at prescribed points of interest. This whole process requires a relatively high level of knowledge of both the design guidelines and the analysis process itself.

1.5 Originality

The contribution of this project was the optimisation of fatigue properties of the transition duct.

2. Literature review

Successful optimisation of stiffeners for waterjet transient ducts requires deep knowledge in several topics such as best practice for stiffener positioning, FEA approaches and fatigue analysis for welded joints, and DNV-GL (Det Norske Veritas – international accredited registrar and classification society) requirements for fabrication of offshore aluminium and steel structures, etc. The literature review intends to cover all these aspects as separate topics.

2.1 Waterjet intake duct overview

The waterjet is a very powerful and reliable propulsion system that provides exceptional manoeuvrability and performance. It consists of four key compartments: water intake, rotor, stator, and water discharge nozzle (Figure 2). The intake duct is an extremely important jet element that is welded or bolted directly to the hull and supplies water flow to the rotor. Thus, performance of the rest of the propulsion system is directly linked to the quality of the flow delivered to the rotor by the intake duct [1]. However, due to several reasons such as local flow separation and nonuniformity, 7 to 9 % of the total power is lost in water intake. Therefore, understanding the factors that contribute to intake power loss is essential [2].

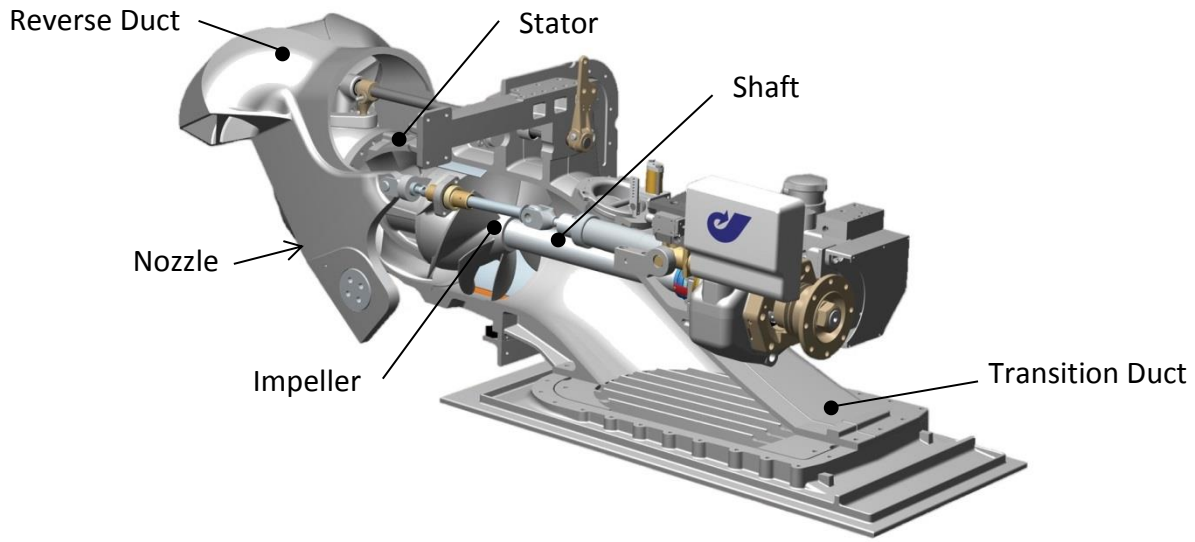

Figure 2. Typical Waterjet arrangement. (*Image HamiltonJet, adapted, used by permission*)

Two types of intake/transition duct are identified: *Ram* and *Flush* intakes [3]. A Ram intake, also known as Pod-Strut intake, is mainly used in hydrofoil craft. Such an intake has an inlet out of the hull on a strut.

For monohulls, catamarans or planning craft, a flush intake is preferable [1]. A flush intake has an inlet adjacent to the hull and it becomes part of the entire hull structure. Therefore, the intake (transition) duct, in addition to the flow supply function, has to meet the same requirements of the Classification Society guidelines for offshore structures as a hull of the boat.

While much information about waterjet intakes exists, most of it is the intellectual property of the manufacturers and is closed to the public domain.

However, a limited number of studies on intake ducts have been conducted and released.

2.1.1 Pressure distribution on the surface of the duct

Pressure distribution on the surface of the duct has been thoroughly studied in the past using different approaches and techniques. The most common method is obtaining the pressure on the surface of the transition duct in the self-propulsion condition [4]. This is an empirical approach using a scaled intake duct set in the test rig and pressure measured using wind tunnel [5].

Bachelor (2003) investigated pressure distribution on the surface of the duct as a part of research supported by HamiltonJet [6]. In particular, the study analysed the flow dynamics within the modified intake ducts of HamiltonJet HJ211 by utilising Quasi-3D and full 3D methods of CFD analysis and then comparing results with empirical data obtained from the wind tunnel rig (Figure 3). This project also re-used the data from earlier studies on the same duct [7–9].

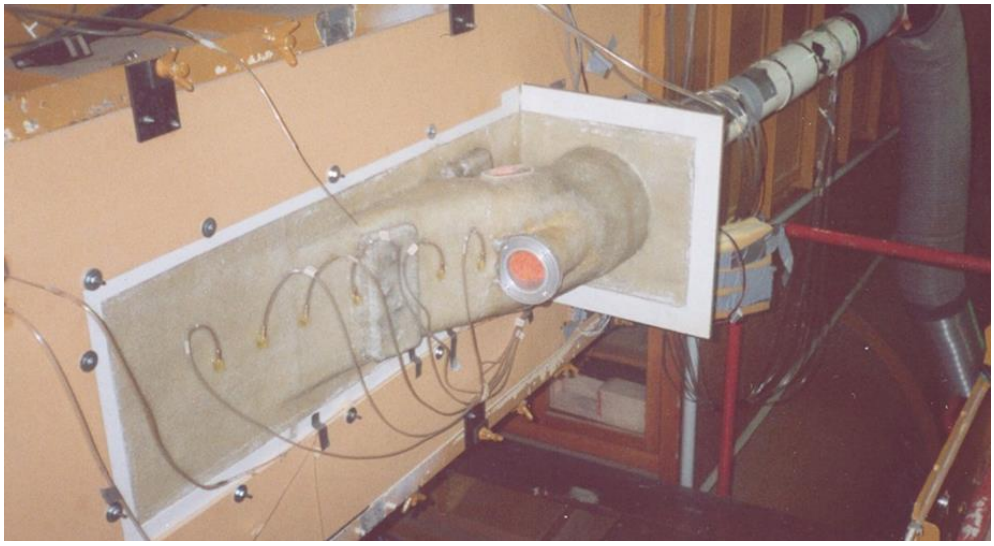

Figure 3. Wind tunnel test rig representing HJ211 intake (*Used with permission of HamiltonJet*)

The static pressure tappings along the roof curve were introduced to the roof as shown (Figure 4). To allow measurements to be conducted over certain areas of interest, a hotwire anemometer and a 5-hole direction probe mounted on an automated two-axis traverser were used as appropriate instrumentation for this experiment.

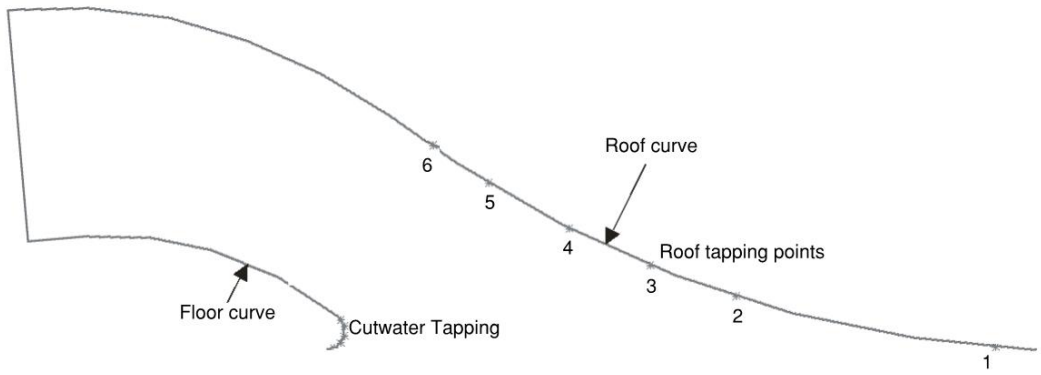

Figure 4. Pressure tapping allocation on the HJ211 jet (*Modified from [6]. Used with permission of HamiltonJet*)

All pressure measurements, along with other parameters, were recorded by a data acquisition system that consisted of Scanivalve rotary pressure switch, pressure transducer and PC.

A non-dimensionalised pressure coefficient (C_p) was determined and plotted as shown in Figure 5. Pressure coefficient, C_p, was defined as:

$$C_p = \frac{p - p_{ref}}{p_{tot} - p_{ref}} \quad (1)$$

Where p_{ref} is wall static reference pressure, and p_{tot} is free stream total head pressure. Both p_{tot} and p_{ref} were taken upstream of the intake.

Figure 5 shows results for static pressure coefficient along roof pressure tappings for different fan speeds under the same Intake Velocity Ratio (IVR), which is defined as:

$$IVR = \frac{V_{imp}}{V_b} \tag{2}$$

Where V_{imp} is mean duct velocity immediately upstream of the impeller, and V_b is a velocity of the boat.

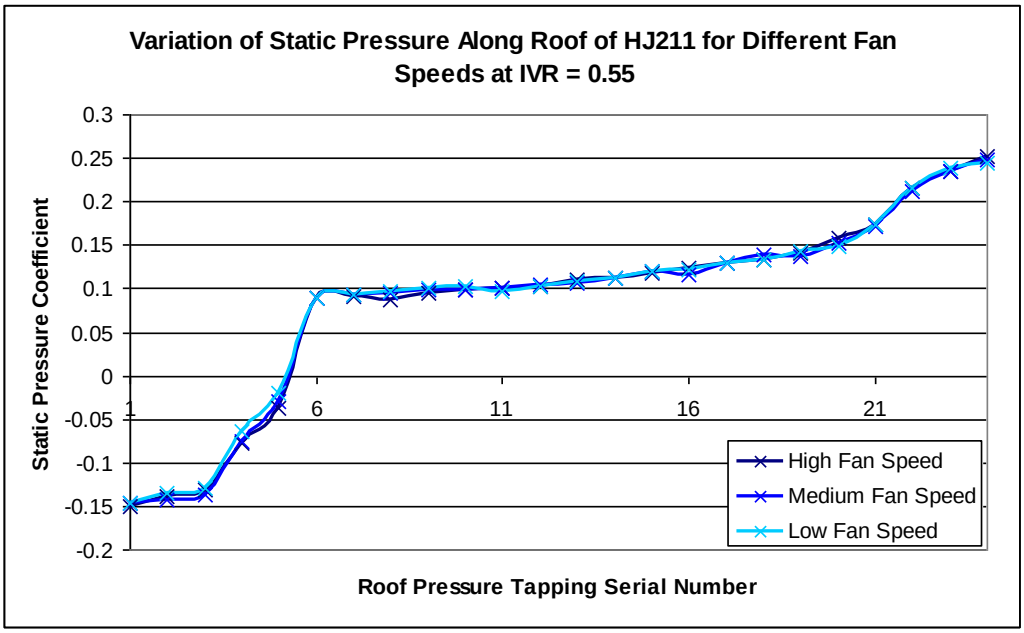

Figure 5. Static Pressure Coefficient plot (*[6] Used with permission of HamiltonJet*).

As seen in Figure 5, the pressure coefficient is below zero value for pressure tappings from 1 to 5. This indicates the presence of negative pressure at the corresponding area, and this is regardless of the flow intensity.

Another significant finding of this study [6] was that the decreasing of the front roof radius resulted in the greater non-uniformity of the flow at the impeller regardless of IVRs. This means that a smaller radius of the curve of the roof degrades the flow characteristics and reduces the jet efficiency.

Some studies applied numerical flow simulation to solve 3D incompressible Reynolds-averaged Navier–Stokes (RANS) equations on a multiblocked grid system of transition duct in order to obtain surface pressure distribution, streamlines and velocity vectors [1, 5].

All numerical results were compared with experiments and, as shown in Figure 6, good agreement was achieved.

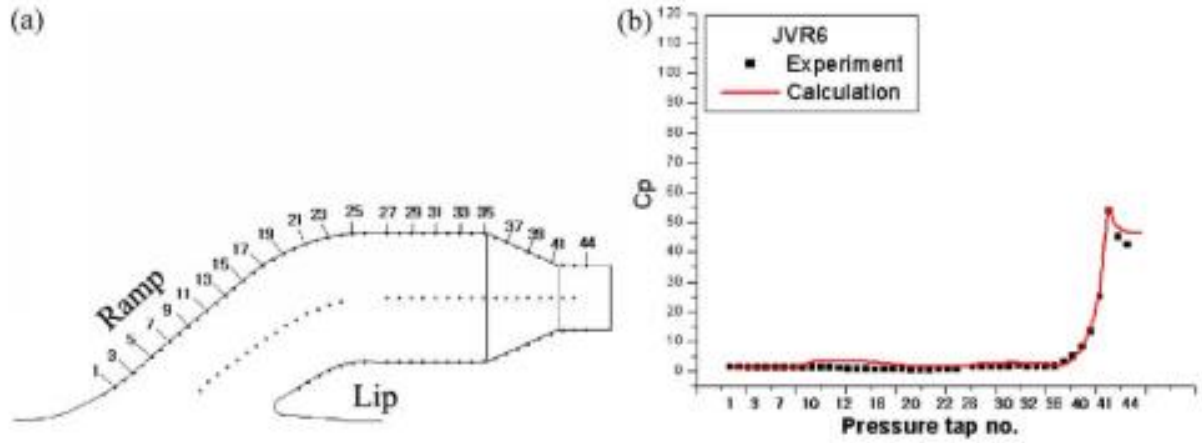

Figure 6. Pressure distribution on the ramp: a) Location of pressure tabs, b) at JVRZ6. *"Reprinted from Ocean Engineering, Volume 32, Issue 17-18, Warn-Gyu Park, Hyun Suk Yun, Ho Hwan Chun,Moon Chan Kim, 'Numerical flow simulation of flush type intake duct of waterjet', Copyright © 2005, with permission from Copyright Clearance Center's RightsLink®"*

Calculations were carried out for three Jet Velocity Ratios (*JVR*): 6, 7 and 8. This ratio is one of the key waterjet parameters and is defined as a ratio of jet velocity (V_j) over boat velocity (V_b):

$$JVR = \frac{V_j}{V_b} \tag{3}$$

where V_j is a velocity at a nozzle and can be measured using an external rake; V_j is boat velocity.

This study revealed a strong suction flow at the low part of the intake (Figure 7c).

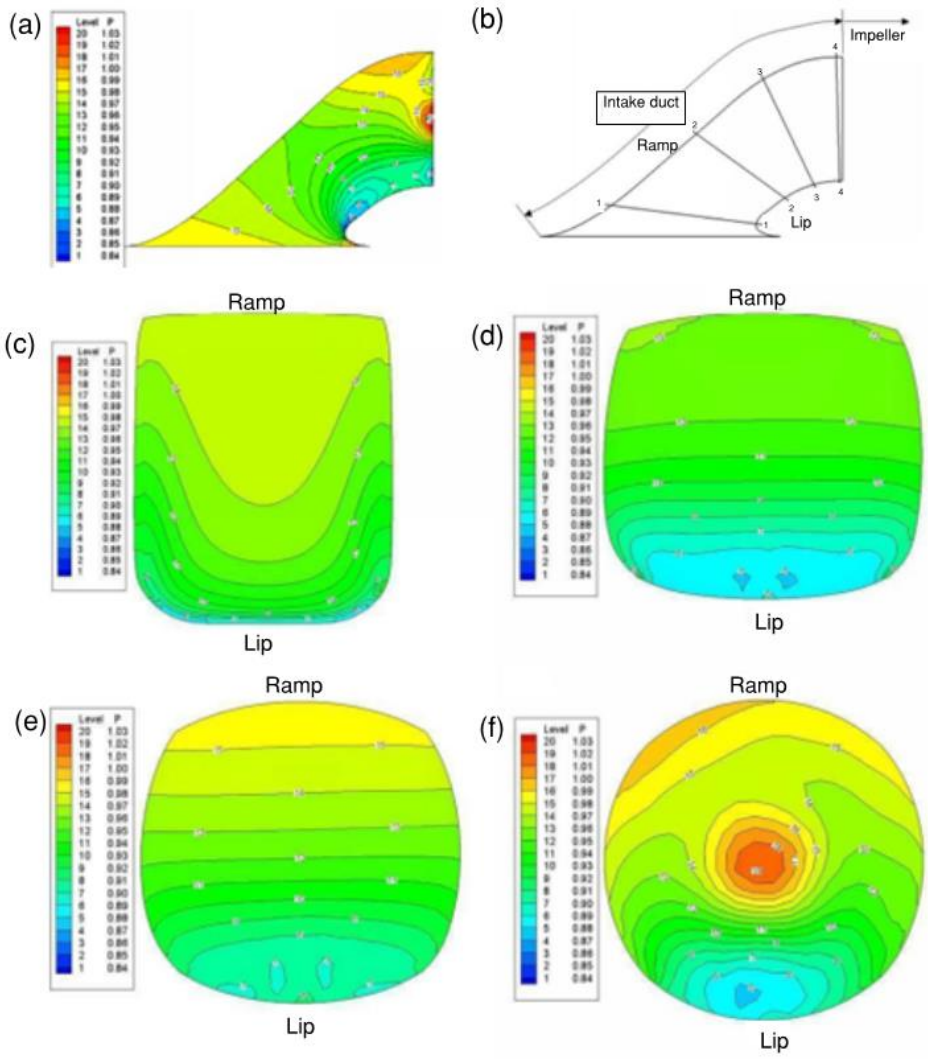

Figure 7. Pressure distribution contours in the intake duct. (a) Duct side view; (b) Cross sections; (c) Pressure contour at Section 1-1; (d) Pressure contour at Section 2-2; (e) Pressure contour at Section 3-3; (f) Pressure contour at Section 4-4. *"Reprinted from Ocean Engineering, Volume 32, Issue 14-15, Warn-Gyu Park,Jin Ho Jang,Ho Hwan Chun,Moon Chan Kim, 'Numerical flow and performance analysis of waterjet propulsion system', Copyright © 2005, with permission from Copyright Clearance Center's RightsLink®"*

Other studies in waterjet technology [10, 11] also cover pressure distributions in inlet duct. These studies focused on other aspects of waterjet-powered vessels such as design methods for modelling of the waterjet/hull interaction and simulation-based design for high-speed boats. However, pressure distribution in the inlet duct was a significant part of the research. Despite the different approaches and boundary conditions applied, all studies were consistent with the nature of pressure distribution in principle. Mapping of the pressure in inlet walls is similar in both studies (Figure 8).

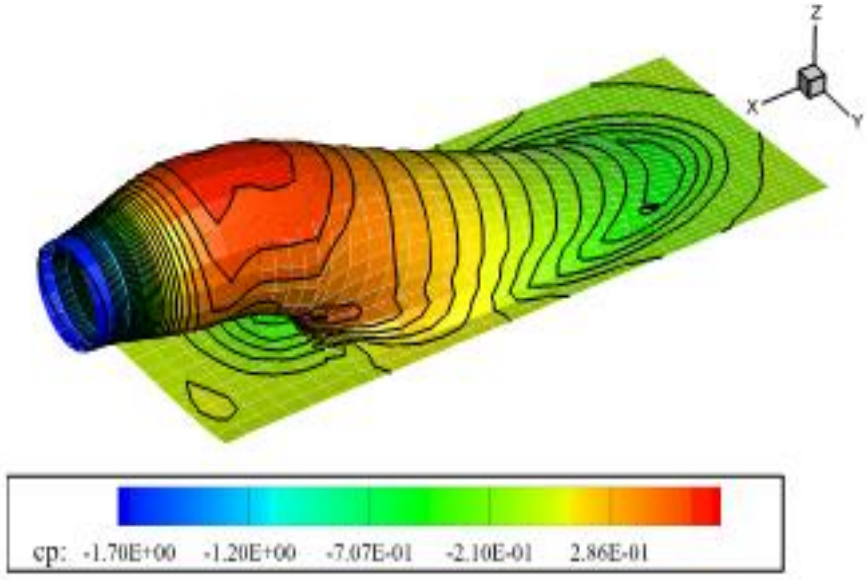

Figure 8. Water inlet pressure distribution. *"Reprinted from Ocean Engineering, Volume 88, Arash Eslamdoost,Lars Larsson,Rickard Bensow, 'A pressure jump method for modeling waterjet/hull interaction', Copyright © 2014, with permission from Copyright Clearance Center's RightsLink®"*

As shown in Figure 7 and Figure 8, contours of the pressure in the inlet duct spread in a similar order where negative (suction) pressure is at the bottom of the ram and the biggest positive pressure is in the impeller tunnel. In addition, as shown in Figure 8, the negative pressure at the bottom of the roof (inlet) occurs regardless of its geometry. Such negative pressure may lead to a downwards deflection (negative z axis in Figure 8) of the lower part of the duct.

2.2 Stiffeners type and positioning for shell structure under blast loading (pressure cycling)

One of the earlier studies for stiffener type selection and the best practical positioning [12] was conducted in 2008 in order to examine the dynamic response of reinforced steel plate which is subject to uniform blast loading. The main study emphasises was on an analysis of the effect of stiffener configurations on midpoint displacement. The study included six different configurations of stiffener location and orientation on the plate (Figure 9). The Abaqus package had been utilised for finite element analysis [12].

It was observed that the addition of the stiffeners reduced displacement at the midpoint. Addition of stiffeners in both direction decreased displacement significantly.

Another important finding is that density of the mesh can influence the computed result considerably for non-linear finite element analysis [12].

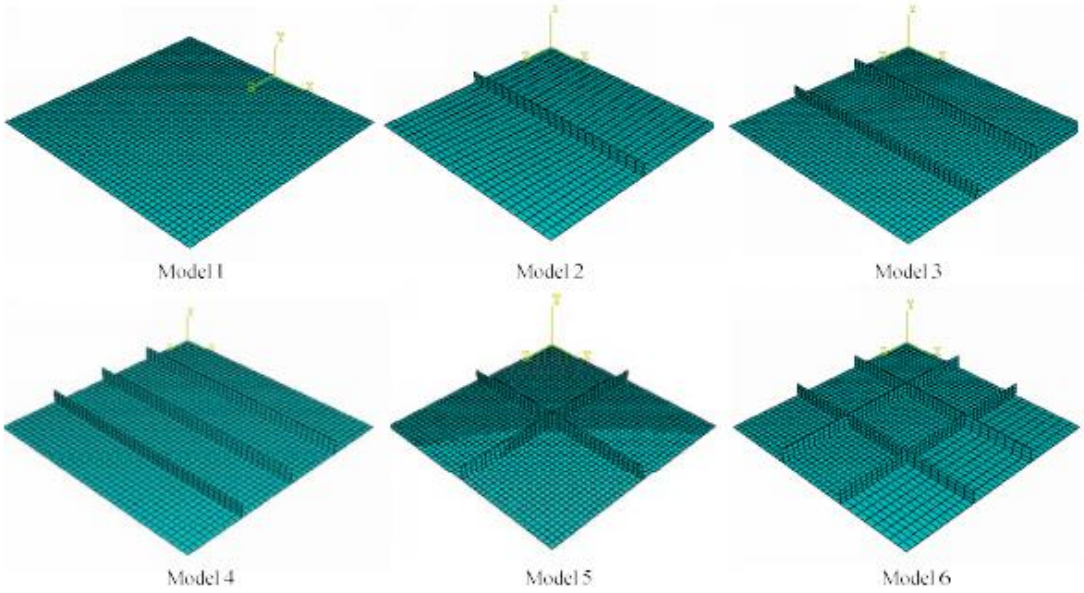

Figure 9. Stiffener configuration. *"Reprinted from Journal of Civil Engineering and Management, Volume 14, Issue 3, Abdelkrim Kadid, 'Stiffened plates subjected to uniform blast loading', Copyright © 2008, with permission from Taylor & Francis".*

The following study [13] was conducted using the Abaqus package for FEA with results verification by using the setup described in [14]. It agreed with [12] in that the arrangement of stiffeners can be important. It was also found that stiffeners concentrated at the middle strip of the plate drastically decrease displacement compared to the same numbers of stiffeners equally spaced on the plate. Furthermore, "for the same number of stiffeners, it is better to arrange stiffeners in two orthogonal directions" [13]. Additionally, it was pointed out that the effect of strain rate must be incorporated into finite element analysis solutions. The inclusion of rate dependence decreases midpoint displacement significantly.

2.3 Fatigue assessment for weld joints

Analysis of the welding endurance is a key element of the structural design of a ship. Welds are the weak area of the structure as they are likely to present crack-like defects and a high stress concentration region. In addition, tensile stresses are presented due to the thermal impact in the welding process itself [15].

Several approaches have been developed, documented and successfully utilised for the assessment of weld joints in fatigue. In this section, the most relevant methods will be described and the most appropriate approach for the current study will be defined.

2.3.1 Critical Distance Method

There are four methods of analysing a high-cycle fatigue action in T-welded joints described in [16]. These methods are:

- The crack modelling method
- The notch stress intensity factor
- Critical Distance Method (CDM)
- The stress averaging approach (SAA)

All four approaches were tested against "a large body of experimental data from the literature" and 2D and 3D models were constructed in ANSYS for FEA. The first two approaches (crack modelling method and stress intensity factor) are based on changes in linear elastic fracture mechanics (LEFM). CDM is based on stress values at critical distances from the weld, taken from FEA. The stress averaging approach uses a fictitious radius concept.

It was found that all described methods provide acceptable predictions of endurance limit for T-shape welded joints for both alloy and steels. However, the Critical Distance Method with FEA was defined as the most accurate and easiest approach.

The Critical Distance Method was proposed by Neuber H., at 1958. Then it was further developed by several scientists such as Tanaka K., 1983 and Taylor D., 1999, who found that "critical distance can be expressed in terms of a material length parameter, L, which is defined in terms of the plain-specimen endurance limit $\Delta\sigma_0$ and the fatigue crack propagation threshold ΔK_{th}" [16]:

$$L = \frac{1}{\pi}\left(\frac{\Delta K_{th}}{\Delta\sigma_0}\right)^2 \tag{4}$$

Material length parameter, L, is constant for a certain material and material condition [17].

The plain-specimen endurance limit, $\Delta\sigma_0$, is the critical stress and its value measured from unnotched specimens.

ΔK_{th} is the threshold stress intensity factor that can be found using equation below:

$$\Delta K_{th} = F\Delta\sigma_{0w}\sqrt{\pi(D+a)} \quad (5)$$

Where:

- D is length of the crack;
- a is material constant;
- $\Delta\sigma_{0w}$ is the fatigue limit of welded joints and it could be obtained by measuring the plain ground butt welds [16].

For predicting endurance limits, an elastic finite element analysis was used. FEA result is the examination of stress/distance curves that are "recorded along lines perpendicular to the local maximum principal stress, which corresponds to the direction normal to the local surface" [18].

While the Critical Distance Method is very accurate and relatively simple, it has one significant disadvantage – it requires a fine FE mesh.

2.3.2 Thermographic Method

Thermographic Method (TM), which is also known as the *Resitano Method*, for prediction of fatigue behaviour of the butt welded joints, was applied as described in [15]. This approach is based on the knowledge that temperature of the material varies during the cycling of the loads applied to that material [19]. It was found that in phase one, specimen superficial temperature normally increases when applied cyclic loads are above the fatigue limit of this specimen; then, in phase two, it reaches a stabilised asymptotic value ΔT_{AS}; and finally, in phase three, when plastic deformations approach the point of failure, the temperature of the specimen rapidly increases [15]. These phases are shown in Figure 10.

Asymptotic temperature ΔT_{AS} corresponds to the applied stress amplitude σ_0. Thus, fatigue limit can be assessed by the $\Delta T_{AS} - \sigma_0^2$ curve. As a further development, *Energy Approach* of the TM described in [21] enables rapid assessment of the entire *S-N* curve.

Energy Approach for TM assumes that fatigue failure happens when the energy is equal to a certain threshold value E_c , where energy E_c is proportional to the integral Φ of the ΔT-*N* curve.

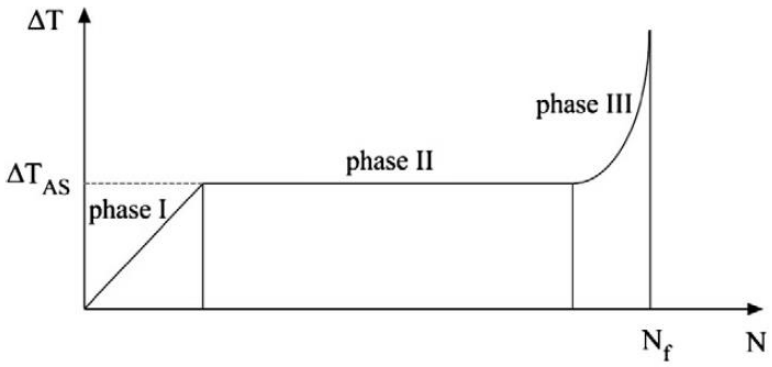

Figure 10. ΔT-N curves obtained by TM [20]. *"Reprinted from International Journal of Fatigue, Volume 32, Issue 17, X.G. Wang,V. Crupi,X.L. Guo,Y.G. Zhao, 'Quantitative Thermographic Methodology for fatigue assessment and stress measurement', Copyright © 2010, with permission from Copyright Clearance Center's RightsLink®"*

Value Φ can be obtained using the equation below, where N_f is the number of cycles to failure (Figure 10).

$$\Phi = \Delta T_{AS} * N_f \quad (6)$$

This method is empirical and requires utilisation of an infrared camera for temperature measurements and simple equipment for applying cyclic loads at a certain stress ratio *R* and frequency *f*.

Therefore, the Thermographic Method "takes temperature increment as the fatigue indicator, enables prediction of the fatigue limit of materials and mechanical components in a relatively short time". This method was found to be very useful in several applications such as fatigue assessment of weld details in ship structures, and estimation of thermoplastic effects for varieties of materials such as steel aluminium alloys and iron [20].

2.3.3 Fatigue assessment based on S-N data

Veritas (2010) advises that fatigue analysis must be based on S-N data, which was obtained by fatigue testing of certain welded detail and the linear damage hypothesis [22].

Fatigue strength in the S-N approach is normally "represented as table, curve or equation that represents a range of data pairs, each representing the number of cycles (N) of a constant stress range (S) that will cause fatigue failure" [23] . This approach uses experimental data to construct and publish S-N curves.

S-N curves are straight lines in a double logarithmic plot calculated using following equation:

$$N = 2 * 10^6 * \left(\frac{\Delta\sigma}{FAT}\right)^{-k}, \; N \leq N_k, \tag{7}$$

where $\Delta\sigma$ is nominal stress range, k is slope and FAT is stress range at $N = 2 * 10^6$ cycles.

Class of the *FAT* depends on the type of assessment concept used, details of the structural welds, parent material, and relevant normal or shear stresses acting on the structure [24].

Three different concepts of S-N curves are developed and described in DNV-recommended practices:

- Nominal stress S-N curve, where the nominal stress is the membrane stress that is used for S-N data plotting derived from fatigue testing.
- Hot spot stress S-N curve, where the hot spot stress is the geometric stress caused by certain construction detail.
- Notch stress S-N curve, where the notch stress is known as the total stress resulting from detailed geometry and a non-linear stress field caused by the notch at the weld toe.

Nominal stress approach

Nominal stress approach is a method of assessing the endurance limit by proceeding from nominal stress amplitudes in the specimen or structural component and comparing them with a nominal S-N curve [25]. The nominal S-N curve includes notch effect and size effect (influence of the shape) and residual stresses (influence of the surface). In some cases, where nominal stresses cannot be precisely defined, the acting forces and moments can be used for assessing fatigue limit. Fatigue limit results obtained from normal stress S-N curve and nominal stress spectrum, based on the simple hypothesis of damage accumulation, are normally agreed to relative Miner rules. Nominal stress spectrum results from a load spectrum, which takes into account the type of loading and cross-section of specimen.

American Bureau of Shipping (2003) [23] recommends using the nominal stress approach in cases where gross geometric changes such as cut-outs, tapers or misalignment are present.

Veritas, 2010, advises that for welded structures the local stress concentrations caused by the joints themselves and by the profile of the weld should be considered for the joint classification and corresponding S-N curve [22].

According to [26], the nominal stress approach has several advantages and limitations. Advantages are:

- Approach is easily applied when detail catalogue includes investigated weld detail and nominal stress can be determined.
- The S-N curve, which is characterised by *FAT* class, considers the failure location such as weld toe or weld root.

Limitations are:

- Detail catalogue covers *FAT* classes only for a limited number of weld details.
- Imperfections such as linear or angular misalignments are not fully covered by the fatigue resistance by *FAT* class.
- Meaningful definition of nominal stress is required.

Hot spot stress

Hot spot stress (structural stress) appears in areas of geometrical inhomogeneity that initiate fatigue cracks [27].

The hot spot stress is defined as a linearised stress that ignores the nonlinear stress peak caused by the notch. As shown in Figure 11, structural stress for plate-to-plate connection can be obtained by linearising the stress across the plate thickness [28].

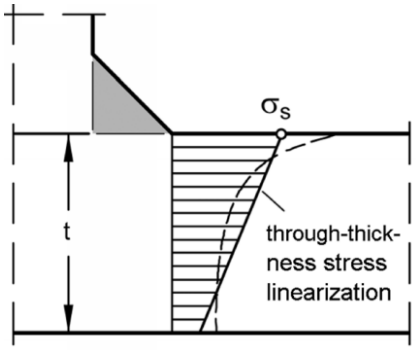

Figure 11. Structural stress linearisation. *"Reprinted from Welding in the World, Volume 58, Issue 6, Heikki Remes, Wolfgang Fricke, 'Influencing factors on fatigue strength of welded thin plates based on structural stress assessment', Copyright © 2014, with permission from Copyright Clearance Center's RightsLink®"*

Therefore, the structural stress σ_S can be calculated using equation 5:

$$\sigma_S = \sigma_m + \sigma_b = \frac{F}{A} + \frac{M}{W} = \frac{1}{t}\int_0^t \sigma(z)dz + 6/t^2 \int_0^t \sigma(z) * (\frac{t}{2} - z)dz, \quad (8)$$

where $\sigma_m$is membrane stress, σ_b is bending stress, and $\sigma(z)$ is given stress distribution; F is internal force, M is moment, A is the cross-section area, W is section modulus, and t is thickness of the plate.

There are different approaches for hot spot stress assessments available and successfully used today. One of them is shown in Figure 12, and it based on plate surface strain at the distance of 0.4 t and 1.0 t in front of the weld toe.

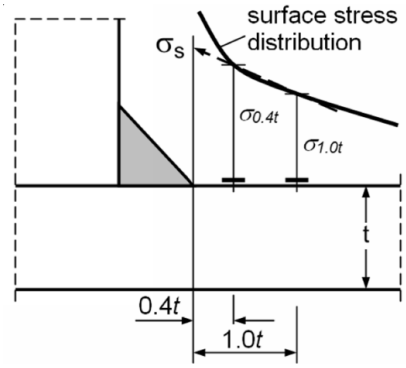

Figure 12. Surface strain approach at the specified distance. *"Reprinted from Welding in the World, Volume 58, Issue 6, Heikki Remes, Wolfgang Fricke, 'Influencing factors on fatigue strength of welded thin plates based on structural stress assessment', Copyright © 2014, with permission from Copyright Clearance Center's RightsLink®"*

Another structural stress assessment method was recently developed by Xiao and Yamada[28]. This approach is based on structural stress that is located at 1 mm below the notch tip (Figure 13). It is assumed that crack propagation at that depth leads to fatigue damage.

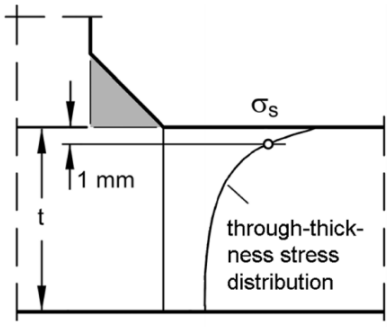

Figure 13. Xiao and Yamada approach. *"Reprinted from Welding in the World, Volume 58, Issue 6, Heikki Remes, Wolfgang Fricke, 'Influencing factors on fatigue strength of welded thin plates based on structural stress assessment', Copyright © 2014, with permission from Copyright Clearance Center's RightsLink®"*

Two approaches of hot spot stress assessment described above are appropriate for thick welded plates only. It was found that there is large scatter of fatigue strength presented in case of using think plates [28].

It must be noted that the stress change due to the weld profile is excluded from hot spot stress; instead, overall influence of the connection geometry on the nominal stress is considered [23].

There are some requirements for the applicability of the structural stress approach [24]:

- Meaningful extrapolation of hot spot stress for the detail of interest is essential.
- Magnification factor k_m must be considered in the finite element model in case of misalignment of anticipated joints.
- Appropriate path for the extrapolation of hot spot stress must be chosen from various paths that may exist for studied application. These paths are determined by finite element analysis and depend on the mesh size used.
- Only failure starting from the weld toe must be considered.

The following limitations exist for hot spot approach:

- There are no recommendations for using this approach for assessing joints in respect to failure starting at the weld root.
- FAT-values are available only for stresses acting normally on the weld. There are no data for welds under torsion.
- The hot spot stress approach is more time consuming due to extrapolation procedures than the nominal stress method.

Notch stress approach

The notch stress approach, which is also known as notch root approach, is used to assess fatigue strength based on comparison of crack initiation that proceeds from the elastic-plastic strain amplitudes located in a notch root and strain S-N curve of the unnotched material specimen [25]. As shown in the Figure 14, it is assumed that material at the notch root in relation to crack initiation, local deformation and local damage mechanically behaves similarly to miniaturized, unnotched or slightly notched specimen under axial load in relation to global damage, global deformation and complete fracture.

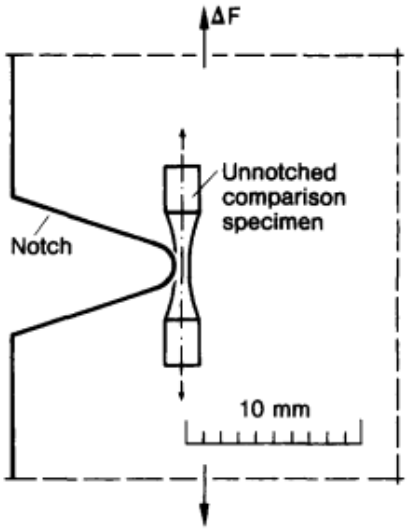

Figure 14. Notch stress approach. *"Reprinted from International Journal of Fatigue, Volume 18, Issue 3, D. Radaj, 'Review of fatigue strength assessment of nonwelded and welded structures based on local parameters', Copyright © 1996, with permission from Copyright Clearance Center's RightsLink®"*

It is required that a comparison specimen must have the same microstructure and surface conditions with consideration of residual stresses and material volume similar to volume in a notch root.

There is the basic idea of all notch stress approaches, which are considered as linear-elastic concepts, being a method with modelling of the weld root or toe using reference radius (Figure 15) to calculate von Mises or local principal stresses and evaluating results by allowable values described in [29].

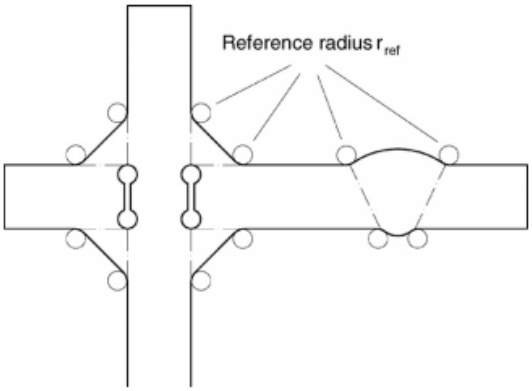

Figure 15. Reference radius in notch stress approach. *"Reprinted from International Journal of Fatigue, Volume 34, Issue 1, C.M. Sonsino,W. Fricke,F. de Bruyne,A. Hoppe,A. Ahmadi,G. Zhang, 'Notch stress concepts for the fatigue assessment of welded joints – Background and applications', Copyright © 2010, with permission from Copyright Clearance Center's RightsLink®"*

There two major reference radiuses that are commonly used:

- $r_{ref} = 1.00\ mm$ is based on the hypothesis of micro support. These radii are fictitious and determined for the worse case of a notch where the real radii are equal to 0.
- $r_{ref} = 0.05\ mm$ is based on relationship between notch stress, stress-intensity factor and crack tip blunting.

In addition, it is stated that selection of values 1.00 mm and 0.05 mm for reference radiuses are supported by empirical observations and assumptions [29]. Thus, the radius of 1.00 mm is often presented at welded joints of structural steels with plate thickness $t \geq 5\ mm$. Radius 0.05 mm is normally observed at welded joints of thin plates with thickness $t < 3\ mm$ made from low and medium strength ferritic steels used for car bodies. Such a small size corresponds approximately to the radius of the notch root of spot-welds, laser welded joints and material grain size.

2.4 Material properties and microstructure

In order to meet customer requirements, the transition duct for HT810 waterjet could be built in two materials: aluminium and steel. Each material option for the duct has its own benefits, downsides and manufacturing approaches. The current study is focused on the transition duct that is built in aluminium. Design of the aluminium intake duct contains sheet metal fabrication (Figure 16a) and cast parts (Figure 16b) welded together.

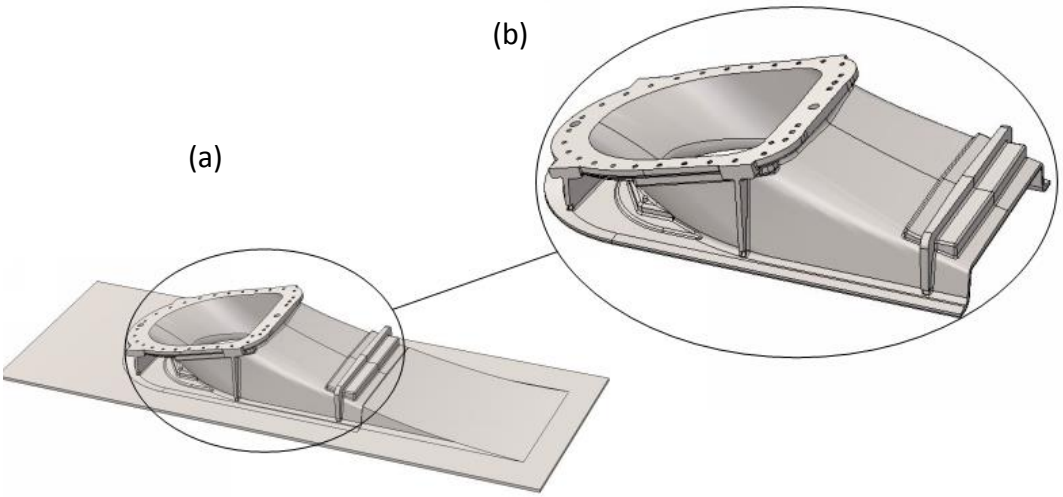

Figure 16. Transition Duct: a) Whole duct; b) Cast part

Aluminium grades for cast and sheet metal are different in order to meet best manufacturing practices. Thus, material for cast is aluminium to EC AC-44100 (LM6), and its properties suit the casting process better. Sheet metal part of the duct is aluminium 5083 that is tempered to H112 and it suits fabrication where forming is required. Additionally, both materials recommended and approved by classification societies such DVN.

The cast part of the intake is not considered in this study as it is out of the area concerned.

2.4.1 Properties

Aluminium 5083 is well known and it is proven to be highly resistant to extreme marine and industrial chemical environments. Its chemical composition (Table 1) provides exceptional performance in harsh environments as well as providing great strength, even after welding.

However, using this grade of aluminium for applications where material can exceed temperature over 65 °C is not recommended.

Table 1. Aluminium 5083 chemical composition. *Copyright 2018 Aalco Metals Limited.*

Element	Percentage, %
Si	0.4
Fe	0.4
Cu	0.1
Mn	0.4-1.0
Mg	4.0-4.9
Zn	0.25
Ti	0.15
Cr	0.05-0.25
Al	Balance (92.55min)

According to BS EN 485-2:2008, for plate 6.3 – 80 mm thick and in the soft O/H111 condition, minimum yield is 115 MPa, tensile strength is 270 – 345 MPa, and Hardness Brinell is 75 HB.

This material is often used for fabrication of marine structures, rail cars, vehicle bodies, etc. Thus it is important to know what the most suitable welding type generally used is. Based on properties (Table 2) and empirical data available these days, the best types of welding for aluminium 5083 are Arc or Resistance (friction) welding. In practice, braze welding or

soldering should be avoided. Filler metal 5183 is recommended where both welded plate are the same 5083 aluminium or from the same sub-group.

Table 2. Basic Physical Properties of Aluminium 5083 H112 [30]

Density	2650 kg/m^3
Melting point	591 - 638°C
Modulus of Elasticity	70.3 GPa
Thermal Conductivity	117 W/m.k
Thermal Expansion	25x10^{-6} /K
Electrical Resistivity	0.058x10-6 Ω.m
Ultimate Tensile Stress	300 MPa
Tensile Yield Stress	190 MPa

For the investigated jet model, aluminium material 5083 is required to be tempered to H112. This tempering is a strain-hardening process where non-heat-treatable alloy increases its strength by strain hardening such as drawing and rolling at room temperature. Additionally, strain hardening treatment achieves some stabilisation in strength level [31].

2.4.2 Microstructure of Aluminium 5083

There are several published studies [32–34] that investigate 5083 alloy microstructure and changes in microstructure caused by Gas Metal Arc Welding (GMAW), Metal Inert Gas Welding (MIG) and friction stir welding (FSW).

All studies show that a grain of a raw (base) material is relatively uniform and insignificantly elongated in rolling direction. The size of grains is about 20–30µm long and 20µm across. Such microstructure is the same for both 5083-H11 and 5083-O grades. Additionally, a large number of inclusions were observed during analysis [35]. The size of inclusions lies in the range >10–100µm and their presence is irregularly scattered in the material. It was found to be difficult to estimate the number of meaningful densities due to an insufficient amount of inclusions presented.

Changes in the size and form of grains were observed after the friction stir welding/process [34, 35]. Thus, the grain size in the Thermomechanically Affected Zone (TMAZ) decreases up to 10µm and it decreases up to 3µm in a nugget zone. The shape of the grains after FSW has equiaxed form.

Similar to FSW, changes in microstructure of alloy 5083-O were observed after Gas Tungsten Arc Welding (GTAW) and Gas Metal Arc Welding (GMAW) [32]. However, this study revealed the difference in the microstructure of GMAW and GTAW samples. Inclined columnar grains were seen along the welding path in the GMAW sample. This effect is described as a result of non-uniform heating and cooling during welding. Closer to the middle of the weld columnar crystals modify to equiaxed form with the average grain size of about 11µm in the fusion zone.

The GTAW sample showed different effects of the welding on the microstructure where distribution of equiaxed grains from parent material to middle of the weld is non-uniform. It was noticed that the grain size in fusion zone was slightly smaller than in the thermomechanically affected zone and its value was 38µm.

Another distinct difference between GMAW and GTAW was a presence of a perceivable number of porosities in the GMAW sample. Fatigue analysis conducted for both samples shows that the existence of porosity makes the structure of Al5083 bonded by GMAW less mechanically reliable than the structure of samples that were joined by GTAW.

2.4.3 Correlation between microhardness and strength of material

A reliable correlation between hardness and other material properties such as tensile strength and yield strength is the one of the key relationships between main mechanical material properties. In some cases micro hardness testing is a preferred method over extensive tensile testing. One such case is when a test needs to be non-destructive and performed on fully assembled components. A good example is a structural integrity test in service. Another case is when microhardness testing could be the only choice because new materials are manufactured in a small number of samples, which makes it insufficient to administer tensile testing. Finally, hardness tests are generally fast and inexpensive [36].

There has been a large body of research focussing on obtaining reliable relationships between hardness and other mechanical properties. In 2011, Zhang et al. [36] consolidated existing findings and performed experimental studies on work-hardened metals and some bulk metallic glasses. This paper classifies four types of relationship between hardness and strength:

- Annealed material:

$$3\sigma_y < H_V < 3\sigma_{UTS} \tag{9}$$

Work-hardened material (state between cold-rolled and Equal Channel Angular Pressing (ECAP)):

$$H_V \approx 3\sigma \tag{10}$$

Where σ represents either yield or ultimate tensile strength

- Alloys processed by high-pressure torsion:

$$H_V < 3\sigma \tag{11}$$

For work-hardened materials the ratio lies in the range from 2.3 to 3.7.

- Bulk Metallic Glasses (BMG):

$$H_V > 3\sigma \tag{12}$$

Based on information described in this paper it is possible to state that material hardness is approximately three times that of the material's strength.

2.4.4 Metallographic properties of material

Revealing the grain structure of common 5000 and 2000-series aluminium alloys may present a challenge when using common etchants. Structural aluminium alloys normally require a metallographic etchant based on HCl, HNO3, and HF, which is commonly referred to as Keller's reagent. This etchant, however, at times does not provide consistent satisfactory results, particularly when the structure of the material is inhomogeneous, has patches of nonrecrystallised and recrystallised grains, or contains clusters of intermetallic particles. Moreover, materials with a poor final polish and a smeared surface may also respond differently to Keller's etchant [37].

Mohammadtaheri (2012) proposed a new technique for revealing grain boundaries in aluminium alloys. This technique consists of two steps. First, at 70 °C the material is pre-etched for 3 min in a solution of 1 g NaCl in 50 mL H3PO4 (40%). Second, the material is

etched with 100 mL H2O + 1g NaOH + 4gKMnO (Weck's reagent). This new technique produced a uniform response to grain boundaries in 2000 and 5000 series aluminium alloys compared with other reagents. Mohammadtaheri (2012) concludes that such results were achieved due to: (a) the effect of the pre-etchant on precipitates and grain boundaries of the material and (b) the subsequent effect of Weck's reagent on grain contrast. Overall, the main advantage of this technique was that polarised light and sensitive tint, or a heat treatment which can affect the microstructure of the material are not required for achieving the final result.

A more recent technique for the microstructure evolution of A6082-T6 BFSW Welds was proposed by Tamadon et al. in 2017 [38]. This technique involved multiple steps, including the removal of the oxide film, followed by delineating the grain boundaries. In addition, some key sequence factors that were considered in the process involved (a) duration of immersion; (b) increasing the temperature up to 70 °C during etching; (c) using immersion in an ultrasonic bath as a measure for improving the uniform etching and removing the oxide layer. The optimisation method described in [38] included setting the chemical composition which was followed by etching until an over-etched surface was achieved. Then the etching time and temperature were progressively reduced until the surface of the material became clear.

2.5 Literature knowledge gap

While there are some useful empirical data about certain aspects of stiffeners fabrication as a solution for reinforcing thin aluminium plates, there is still uncertainty about the stiffening of waterjet units.

One general issue of the waterjets is non-uniform pressure caused by water flow. Although different jets have unique design and geometry, it is common to observe negative pressure at a lower part of intake. Furthermore, the design of waterjets appears to be an intelligent property of jet manufacturers. Hence, rigorous evaluations of the duct stiffening approaches available are lacking in open sources. Therefore, the following knowledge gaps need to be addressed:

1. There is no fatigue analysis conducted on the current transition duct using the latest CFD data.
2. Existing studies cover only basic arrangements of the stiffeners for plane surfaces and uniform pressure distribution. However, the roof-plate of the transition duct of HT810 jet has curved geometry and complex boundary conditions. Furthermore, pressure applied on the internal surfaces of the duct is non-uniform.
3. What is the most cost-effective and practical fabrication approach for stiffeners?
4. Could welding of the stiffeners degrade the fatigue resistance?
5. Do the introduced weld details comply with requirements of the classification societies?
6. Does weld-on-weld contribute to reducing the fatigue strength?

3. Methodology

3.1 Case details

The specific case under examination is HT810 jet – one of the three large jets of HT-series (Figure 17). This is characterised as a large jet with power inputs up to 5500kW (7372hp).

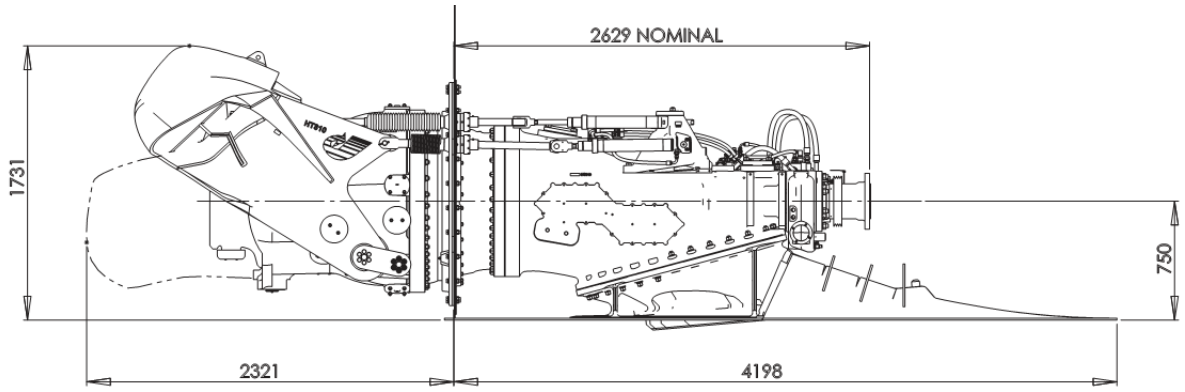

Figure 17. TH810 overall dimensions. Transition duct – steel version.

HT waterjets are generally suitable for 60–80m craft using two or more engines and waterjets. As an example, a high-speed catamaran SEACOR LYNX (Figure 17) with HT810 quad jets.

Figure 18. High-speed catamaran SEACOR LYNX. *Copyright © 2007, with permission from HamiltonJet.*

3.2 Study approach

The research and development needs for this unit are the same as those described in the previous section, namely the need to stiffen the roof plate against roof deflection and fatigue failure under cyclic negative pressure loads. CFD data had recently become available for this particular unit and mapped onto the model (Figure 19).

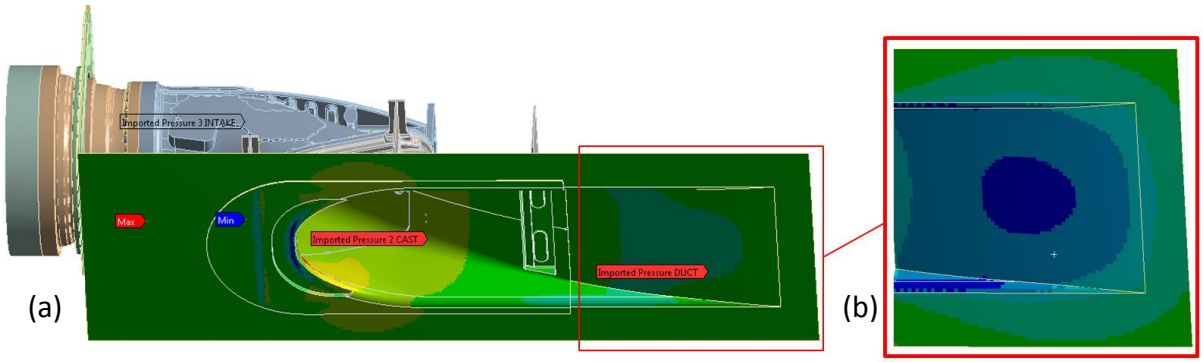

Figure 19. Pressure distribution: a) pressure applied onto entire jet; b) detailed (scaled) pressure onto intake plate

Figure 19 shows only pressure distribution where the area highlighted in blue has a suction effect (negative pressure). Pressure mapping was based on the data extracted from CFD analysis and provided by the R&D Department of HamiltonJet in a form of spreadsheet.

An initial solution for this problem was adding stiffness to the roof plate. With this solution some complexity arose due to stiffening plates being welded to the transition ducts and the possibility that this introduced new failure modes to the welds. Therefore, the fatigue endurance of welded elements needed to be assessed in order to meet the requirements of DNV, Eurocode and ABS Classification Societies. Therefore, there is a need to design a suitable arrangement for the stiffeners that considers orientation, quantity and profile of stiffeners. This also needed to take into account multiple maritime load scenarios, manufacturability (weld process, weld access, weld defects, adverse heat treatment, toe grinding), ship classification society requirements for allowable stress, and commissioning/installation for the end-user.

In order to find the most appropriate solution for the optimisation of the existing roof-plate design, a study was conducted in several steps. First, and one of the most important steps, was to study and understand the requirements of DNV, Eurocode (EN 1999-3-1) and ABS Classification Societies. The second step was FE analysis of the load cases dictated by

authorities and applicable to the waterjet in conjunction with the pressure on the intake duct caused by the water flow. The pressure was obtained from a Computational Fluid Dynamics analysis (CFD) conducted outside of this study and provided by the Company in spreadsheet form. This pressure is non-uniform and acted differently along the jet. Additionally to the second step, a comparison analysis was conducted. The goal of this analysis was to compare consequences of the application of the loads only and combination of the loads and pressure on the default configuration of the intake duct. The third step was an optimisation of the intake stiffening that included analyses for stiffener orientation, positioning, quantity and geometry of the stiffeners. The fourth step was a calculation of the fatigue life for the most appropriate solution and comparing the obtained results with requirements of DNV, Eurocode (EN 1999-3-1) and ABS Classification Societies. Finally, the following step included two sub-steps. The first was validation of the manufacturability of the solution, the cost associated with its implementation and possible cost lost if solution is not applied. The second was validation of the weld quality by performing optical microstructure and hardness tests.

3.3 FEA approach and assumptions

3.3.1 Assumptions

ANSYS was utilised as primary software for finite element analysis and optimisation study. CAD files for the Jet HT810 model were provided by the Company at a scale 1:1. However, some internal and external jet components were excluded from the model in order to simplify mesh and reduce solving time for all load cases applied to the jet. In cases where loads acted on missing components *Remote Loads* were applied on a mating surface.

All dimensions or coordinates of the CAD model or ANSYS were based on the Coordinate system located at the face of the Intake as shown in Figure 20.

It is assumed that the fixed support applied to the adjusting hull structure is absolutely rigid. However, the absolute rigid fixation of the jet to the hull is unlikely in a real jet installation process and final results of the analysis need to be accounted for.

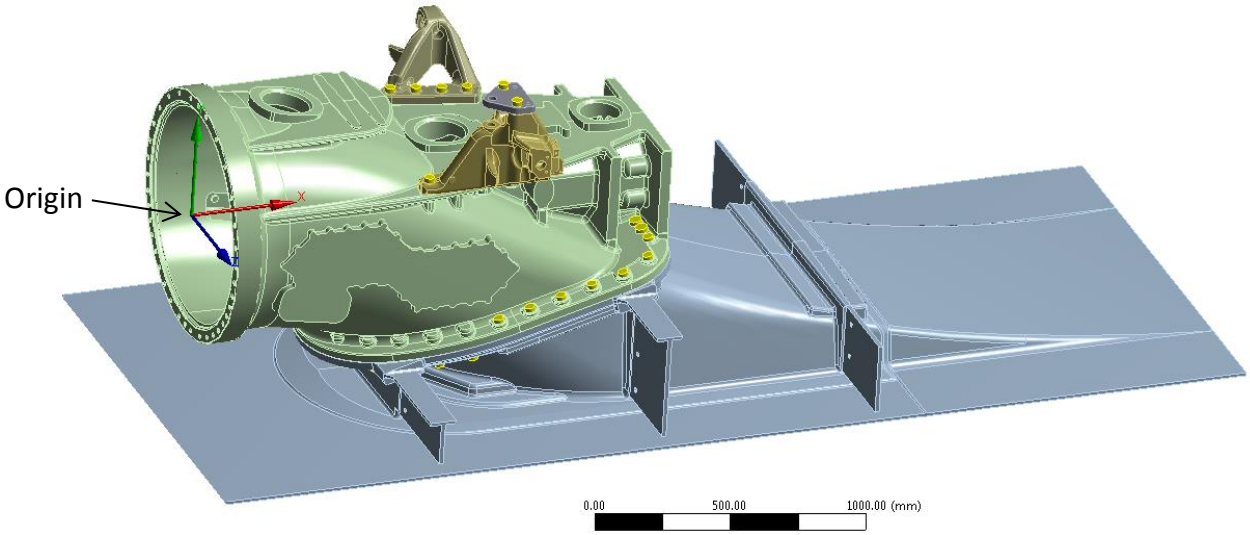

Figure 20. Coordinate system of the model

Welded joints between cast body and fabricated sheet metal parts of the Transition Duct were set in analysis as a Multiple Point Connection (MPC). This type of *Bonded* connection assumes that all nodes of mating parts are rigidly connected in the weld region (Figure 21).

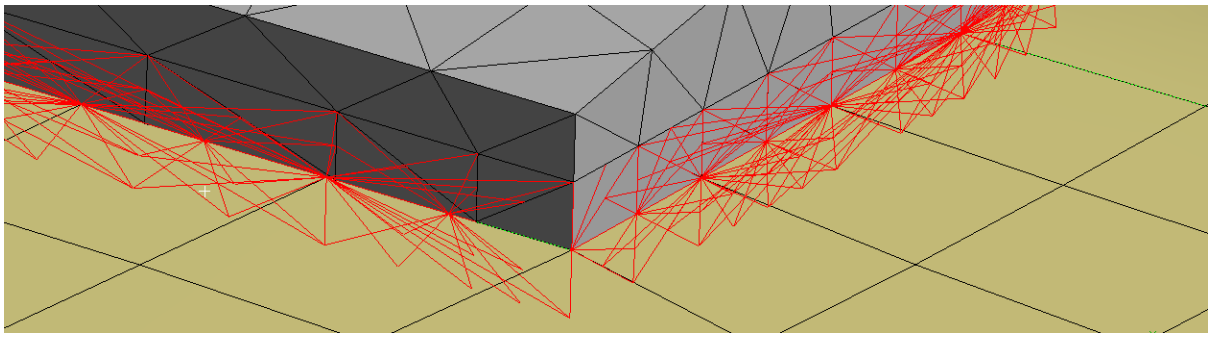

Figure 21. Graphic representation of the MPC connection, where rigid links shown in red, cast (solid model) and sheet metal (shell model) are shown in grey and yellow respectively.

Welds in the fabricated sheet metal part of the Transition Duct were not modelled. Instead, a mono surface was modelled in order to represent the fabricated part. While the weld geometry is not included in the study, all weld geometry issues and imperfections are accounted for by formulations described in DNV-GL [39].

Sheared topology was used for joining stiffening plates and roof-plate instead of the MPC connection. Such assumption allows a better distribution of the loads/stresses.

3.3.2 Shell element technique

According to Eurocode (EN 1999-3-1), thin shell elements were applied to sheet metal parts, such as a sheet metal part of the Transition Duct and stiffening plates, to solve elastic structural stresses. Parabolic 8-noded elements were applied to the shell structure with mesh size being equal to the plate thickness of 12 mm.

3.3.3 Submodel technique

The conducted analyses for the load cases on the default jet configuration revealed that it required considerable ANSYS solving time and computer resources due to complexity of the model. In order to significantly simplify the model, the Submodel technique was utilised for further optimisation study.

The submodel technique with imported pressure and boundary displacement from parent model (Figure 22) successfully eliminated the complexity and multiple recalculations of the entire model setup for each design candidate.

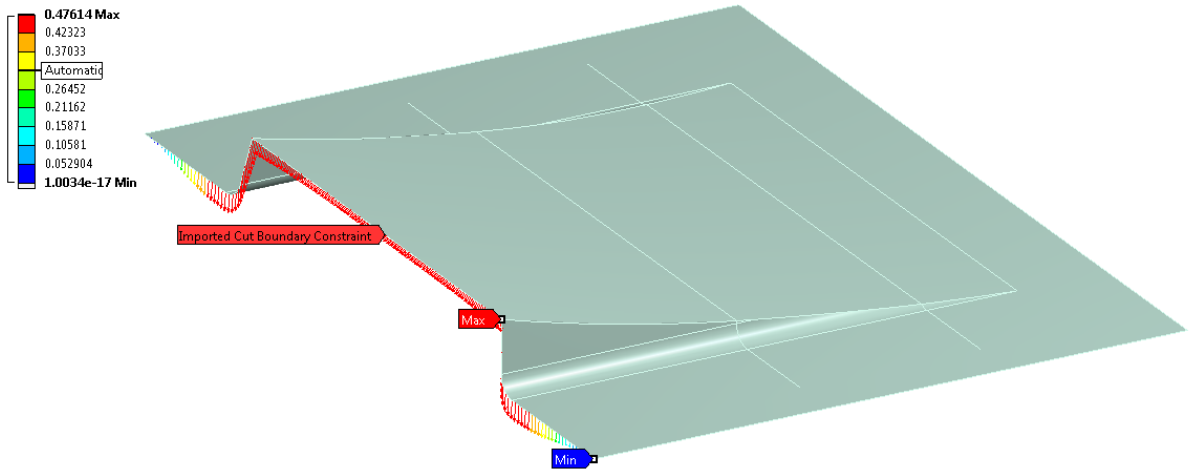

Figure 22. Submodel of the intake duct for optimisation study

The submodel represents only a shell intake duct and it was “cut” from the rest of the jet in the area that was close to the cast (Figure 22). The imported “Cut boundary Constraint” was taken from the results for Full Ahead mode. Imported displacement was then assigned to the cut side of the submodel, pressure was imported, and the fix support was applied to the external edges in the same way as per the full jet model. Meshing applied to the model had high quality with 22,042 nodes and 19,514 mesh elements.

In order to prove that the submodel represents full jet model and was appropriate to be used for further optimisation study, the Full Ahead results obtained by the submodel were compared with results from the corresponding study for the full model.

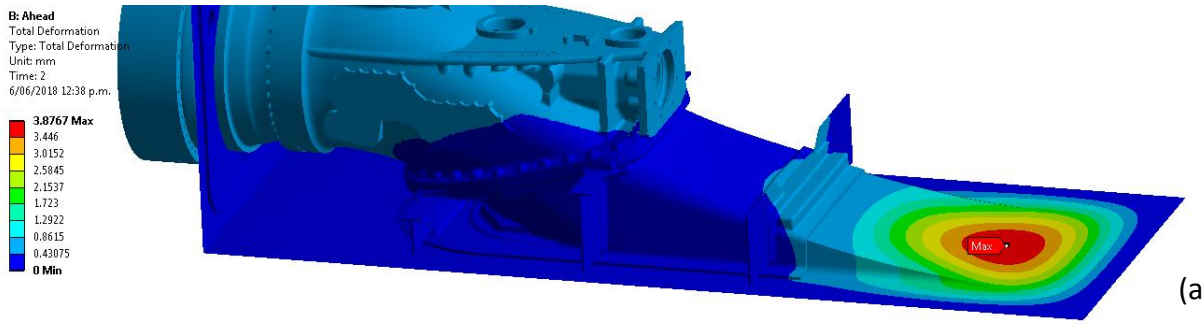

(a)

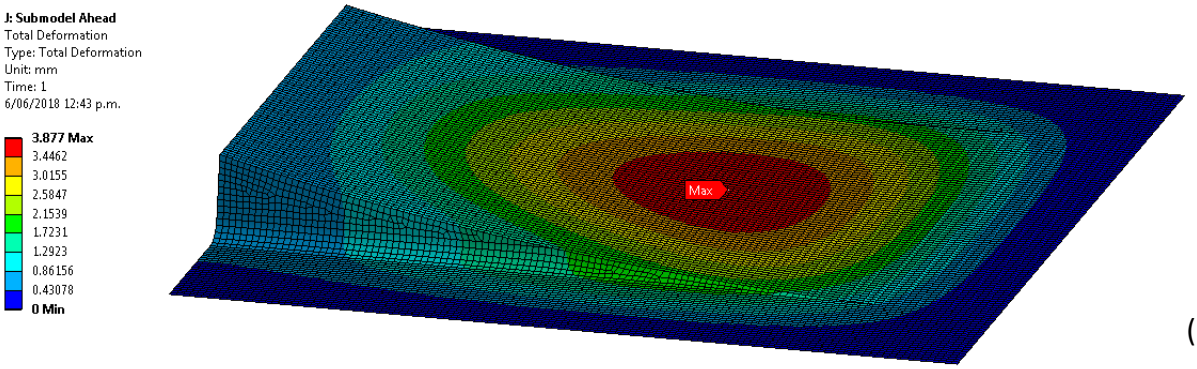

(b)

Figure 23. Full Ahead LC results: a) Full jet model; b) Submodel

As shown by Figure 23, the results of the submodel were equal to the results of the full jet model. Therefore, the submodel was used for further optimisation study with a high degree of confidence.

3.3.4 Data retrieval approach

In order to obtain data needed for further fatigue calculation, DNV-GL dictates to derive stress range parallel to the weld at the hot spot and stress range perpendicular to the weld at the hot spot at the distance of 0.5*t* (where *t* is a plate thickness) from the joint line (welded connection). Hot spots were revealed using the Probe Tool (Figure 24).

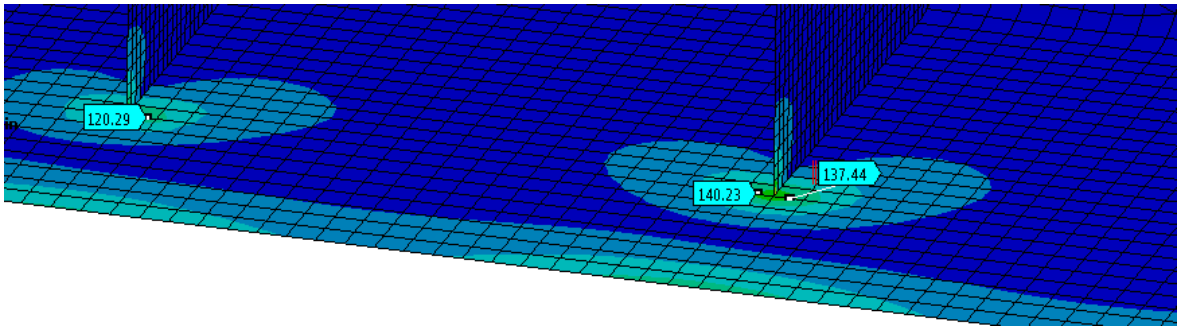

Figure 24. Revealing the Hot spots by Probe tool

Every time the node with the highest stress was defined, a new Coordinate System was created at the node location. Furthermore, to reveal the stress range at the weld toe, which is normally located on the top surface of the plate, every node related (local) Coordinate system was offset by 6 mm in Y-direction (Figure 25). In some points of interest such as weld in the middle of the stiffening plates or weld-on-weld regions, Coordinate systems were additionally angled according to the roof curve.

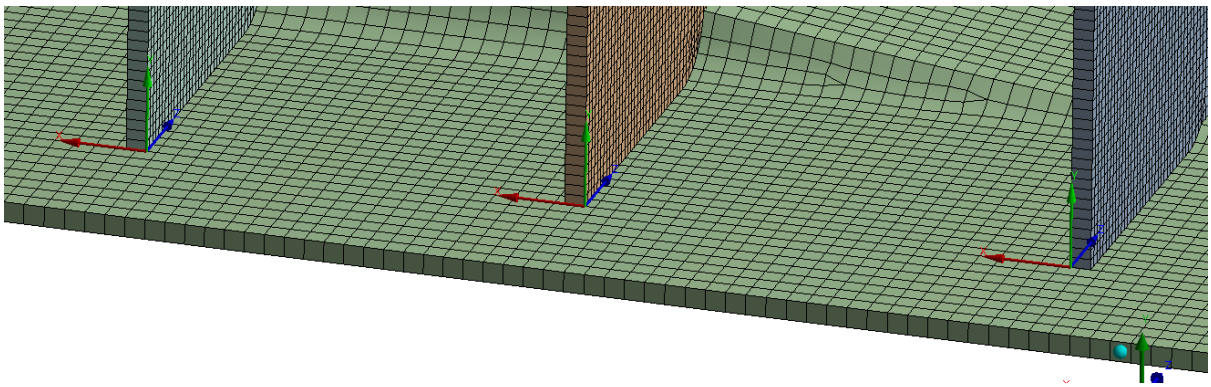

Figure 25. Node-related Coordinate systems

Such an approach provides a useful opportunity to obtain exact values of stress range parallel to the weld and stress range perpendicular to the weld as well as shear stress parallel to the weld at the particular node at the area of interest.

All local Coordinate systems and their legends are shown in Figure 26:

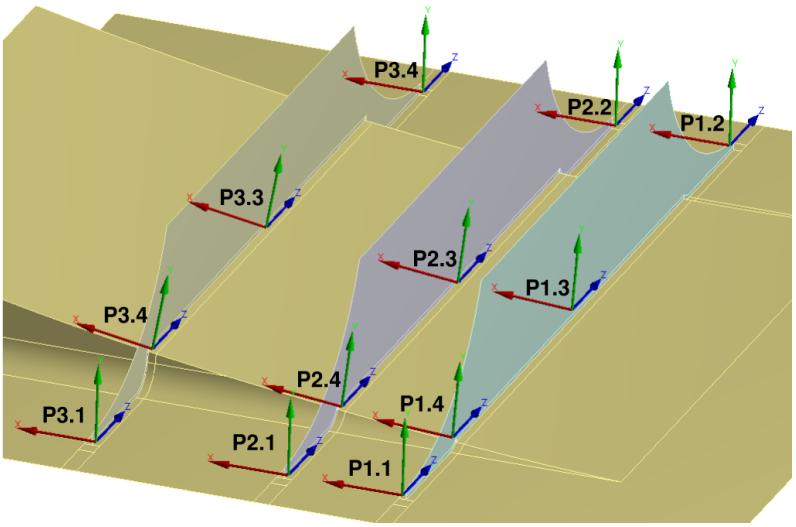

Figure 26. Locations and legends for local Coordinate Systems

In order to assist with the selection of the appropriate node that must be at the distance 0.5*t* (where *t* is a plate thickness) additional split lines were applied at the distance of 12 mm from the joints (Figure 27).

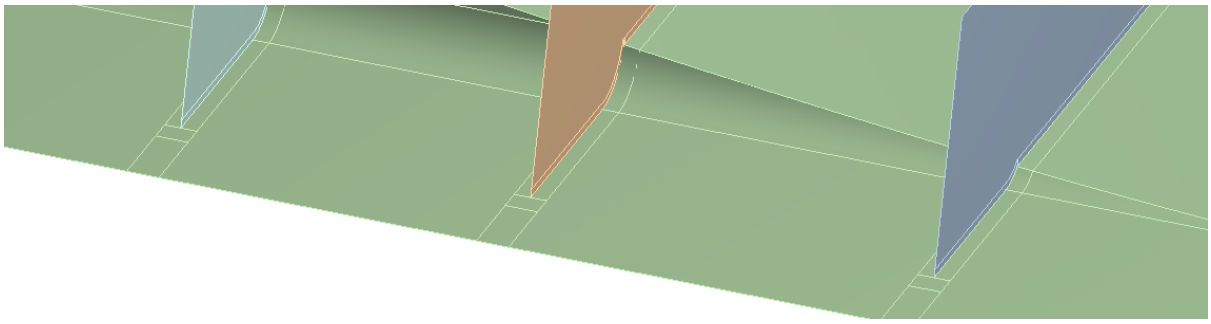

Figure 27. Split lines around joints

This improves a mesh of the shell elements in joint-surrounding areas. Therefore, it allows the selection of mid-node, which is located exactly on the required distance 0.5*t* from the joint line.

3.4 DNV-GL and ABS Classification Societies requirements for fatigue design of offshore aluminium structures and waterjets

3.4.1 Introduction to Classification Societies

The marine industry is one of the key elements of a world transport network. Safety of the marine fleet, offshore structures, and goods and people transferring is a priority for the industry. A number of countries have their own marine authorities and professional bodies, while others belong to larger Classification Societies in order to promote safety and obtain

necessary knowledge for ongoing management of risks. These authorities and organisations provide verification, classification, certification and training, as well as designing and establishing standards and best practices. Therefore, complying with the appropriate requirements and standards of the marine authorities is of high importance for manufacturers, particularly for those who distribute their products and goods to different countries where marine safety regulations may be different.

HamiltonJet provides a number of different waterjet solutions worldwide and thus has to meet requirements of a number of global authorities such ABS (American Bureau of Shipping), which covers North and South America, and DNV-GL, which covers Europe and some Asian regions.

3.4.2 DNV-GL fatigue requirements for aluminium offshore structures and welded elements

DNV-GL prescribes a detailed fatigue analysis of any individual type of structural detail that may be involved in substantial dynamic loading. Additionally, all welded joints or attachments should be individually investigated as a potential source of fatigue cracking.

Two methods of fatigue design are recommended by DNV-GL (CN30-7). The first method is based on empirical data (S-N curve) and the second is based on Palmgren-Miner's rule (estimation of cumulative damage).

Additionally, the long-term stress range distribution must be calculated for fatigue analysis due to its importance of accounting for high and low cycle fatigue.

However, paragraph 1.4 of the CN30-7 allows the omission of the detailed fatigue analysis if the largest local (hot spot) stress range for a particular detail that is in dry area ("in air") or cathodic protected does not exceed the endurance limit at 10^7 cycles.

3.4.3 Static load conditions

DNV-GL (CN30-8) defines the following static load conditions in Table 3 that must be applied to the waterjet duct:

Table 3. Static load conditions for waterjet (CN30-80)

Load Condition (LC)	Description	Allowed combined axial and bending stress (MPa)	Allowed shear stress (MPa)
LC 1	Crash stop	$180 * f_1$	$100 * f_1$
LC 2	Maximum load from reversing	$160 * f_1$	$90 * f_1$
LC 3	Maximum load from steering	$160 * f_1$	$90 * f_1$
LC 4	Waterjet unit weight accelerated as cantilever in pinching	$160 * f_1$	$90 * f_1$

f_1 is material utilisation factor:

$$f_1 = \sigma_f / 240 \tag{13}$$

Where σ_f is yield stress and it must not be greater than 70% of Ultimate Tensile Stress (UTS).

Taking into account that yield stress for aluminium 8053 H-112 is 190 MPa and UTS is 300 MPa, the yield stress, σ_f, is equal to 190 MPa. Thus, based on the formula above, the material utilisation factor, f_1, is 0.79. Therefore, Table 3 could be converted into Table 4:

Table 4. Static Load Conditions – Calculated

Material	Material utilization factor (f_1)	Allowed combined axial and bending stress (MPa)		Allowed shear stress (MPa)	
		LC1	LC2,3,4	LC1	LC2,3,4
Wrought plate 5083 H112	0.79	142.2	126.4	79	71.1

Additionally, areas with high stress must be avoided for placement of welds or other types of stress risers.

3.4.4 Fatigue causing load conditions

DNV-GL recommends considering the long-term load distributions as shown in Table 5:

Table 5. Long-term Load Distribution. Adapted from Table 4-1 of [39]

Long-term Load Distribution (LD)	Description	Assumptions	Cycles, n_i
Reversing loads, LD1 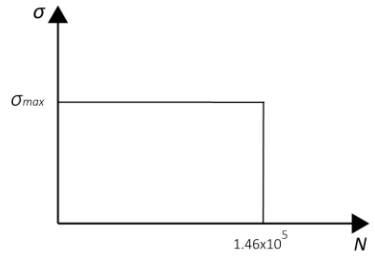	σ_{max} is taken from analysis of LC2 (Table 4)	Maximum reversing load 20 per day for 20 years.	1.46x10^5
Steering loads, LD2 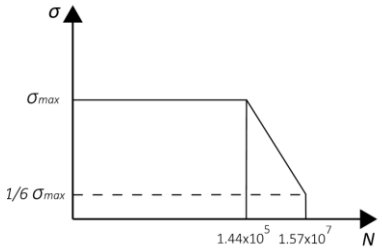	σ_{max} is taken from analysis of LC3 (Table 4)	Steering cycle of 20 seconds 12 hours per day for 20 years. Corresponding to 5° steering ($1/6\sigma_{max}$) – flat water.	1.57x10^7 (corrective steering)
		40 hours per year for 20 years. Corresponding to 30° steering (σ_{max}) – heavy seas.	1.44x10^5 (full steering)
Pitching loads, LD3 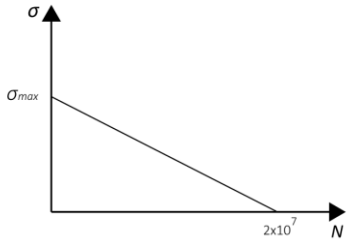	σ_{max} is taken from analysis of LC4 (Table 4). This is waterjet cyclic cantilever loads as a result of vertical stern accelerations	12-hour operation per day. Linear variation of pitching loads between 0 and maximum.	2x10^7

Additionally to steering loads (DL2), "The steering load varies with the angle ranging from corrective steering 5° (flat water) and full steering 30° (heavy seas). It may be assumed that steering at any angle varies from port to starboard at any one cycle, so that stress range at a detail is double that calculated from the static equivalent at any angle. Maximum values may be taken from the analysis of LC3 (for fatigue assessment of flanges stress range can be considered as the range from bending stresses and axial stresses when in tension to only axial stresses in compression)" [39].

The pressure distribution, as a part of all load cases, was found to be the main contributor to the roof-plate deflection. The biggest effect of the pressure application was observed in Full Ahead mode, which is not listed in Table 5 as a Load Case. However, load case LD2

(Steering loads) described in Table 5 is the *ahead* steering mode. Hence, using the conservative approach, Full Ahead mode was included to the fatigue calculations as an Ahead load case, LD4. In order to eliminate load duplications, Steering loads, LD2, were adjusted as described below.

Figure 28 shows the example of the changes in the stress range for one full steering cycle for one particular hot spot (P1.1, Figure 26). Step 1 of the cycle represents the effective stress range of 50.3 MPa (from 0.0 MPa for roof-plate in default state, to 50.3 MPa for roof-plate experiencing the maximum deflection) for full ahead mode. Step 2 corresponds to steering to the port with the effective stress range of 1.5 MPa – from 50.3 MPa for full ahead to 48.8 MPa for steering port. Step 3 is a full ahead mode during transition from starboard to port steering with effective stress range of 1.5 MPa – from 48.8 MPa for steering port to 50.3 MPa for full ahead. Step 4 corresponds to steering to starboard with the effective stress range of 0.6 MPa – from 50.3 MPa for full ahead to 49.7 MPa for steering starboard. The final step, Step 5, is the end of the cycle that corresponds to the full ahead mode with effective stress range of 0.6 MPa – from 49.7 MPa for steering port to 50.3 MPa for full ahead.

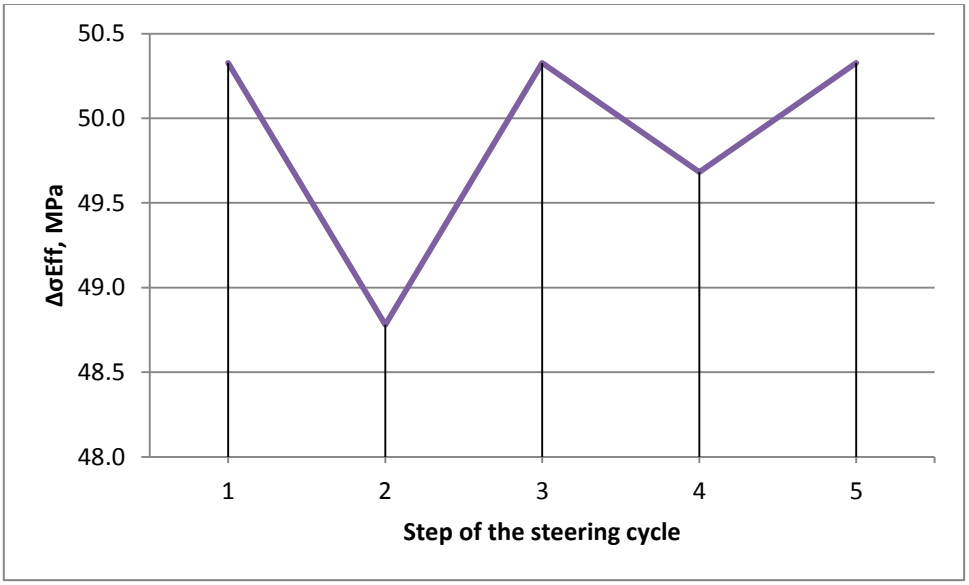

Figure 28. Stress range development during one steering cycle for the hot spot P1.1

Therefore, adjusted effective stress ranges for steering loads, $\Delta\sigma_{Eff(\text{adj})}$, can be found as:

$$\Delta\sigma_{Eff(\text{adjPORT})} = 2 * (\Delta\sigma_{Eff(full\ ahead)} - \Delta\sigma_{Eff(port\ ahead)})$$
$$\Delta\sigma_{Eff(\text{adjSTB})} = 2 * (\Delta\sigma_{Eff(full\ ahead)} - \Delta\sigma_{Eff(std\ ahead)}) \quad (14)$$

3.4.5 Fatigue assessment

DNV-GL requires performing the fatigue assessment based on the cumulative damage rule (Palmgren-Miner rule). The cumulative damage rule specifies that accumulated damage from all events must be less than a specified usage factor, η. DNV-GL specifies a usage factor equal to 1.0.

Thus, for each loading scenario the accumulated damage is:

$$D = \sum_1^i n_i/N_i \quad (15)$$

Where:

n_i is a number of cycles at stress range for each of the long distribution load case ($\Delta\sigma_{i,max}$);

N_i is a number of cycles of failure at stress range ($\Delta\sigma_{i,max}$), and it can be found using the appropriate formula below:

- For design cycles in the range 10^5 to $5 * 10^6$:

$$N_i = 2 * 10^6 \left(\frac{\Delta\sigma_c}{\Delta\sigma_i} * \frac{1}{\gamma_{Ff} * \gamma_{Mf}}\right)^{m_1} \quad (16)$$

- For design cycles in the range $5 * 10^6$ to 10^8:

$$N_i = 5 * 10^6 \left(\frac{\Delta\sigma_c}{\Delta\sigma_i} * \frac{1}{\gamma_{Ff} * \gamma_{Mf}}\right)^{m_2} * \left(\frac{2}{5}\right)^{\frac{m_2}{m_1}} \quad (17)$$

Where:

- $\Delta\sigma_c$ – reference value of fatigue strength, depending on the detail category, (Table 6)
- $\Delta\sigma_i$ – stress range for the principal stresses at the constructional detail and is constant for all cycles. It is also known as effective hot spot stress range and it can be found using the formula below.

- m_1 – inverse slope of the $\Delta\sigma$- N curve, depending on the detail category (Table 6).
- $m_2 = m_1 + 2$
- γ_{Ff} – partial factor allowing for uncertainties in the loading spectrum and analysis response (Table 6).
- γ_{Mf} – partial factor for uncertainties in material and execution (Table 6).

$$\Delta\sigma_{Eff} = max \begin{cases} 1.12 \sqrt{(\Delta\sigma_{\perp})^2 + 0.81 * \Delta\tau_{/\!/}{}^2} \\ 1.12 * \alpha \, |\Delta\sigma_1| \\ 1.12 * \alpha \, |\Delta\sigma_2| \end{cases} \quad (18)$$

Where:

- $\Delta\sigma_{\perp}$ - stress range perpendicular to the weld at the hot spot (from FEA)
- $\Delta\sigma_{/\!/}$ - stress range parallel to the weld at the hot spot (from FEA)
- $\tau_{/\!/}$ - shear stress parallel to the weld at the hot spot (from FEA)
- $\alpha = 0.9$ – for the detail type as classified under C2 (Table A-3 DNV) with stress parallel to the weld at the hot spot
- $\Delta\sigma_1$ – first principal stress (formula below)
- $\Delta\sigma_2$ – second principal stress (formula below)

$$\Delta\sigma_1 = \frac{\Delta\sigma_{\perp} + \Delta\sigma_{/\!/}}{2} + \frac{1}{2}\sqrt{(\Delta\sigma_{\perp} - \Delta\sigma_{/\!/})^2 + 4 * \Delta\tau_{/\!/}{}^2}$$

$$\Delta\sigma_2 = \frac{\Delta\sigma_{\perp} + \Delta\sigma_{/\!/}}{2} - \frac{1}{2}\sqrt{(\Delta\sigma_{\perp} - \Delta\sigma_{/\!/})^2 + 4 * \Delta\tau_{/\!/}{}^2} \quad (19)$$

Table 6. Detail categories for fillet joins between members. Extracted form Table J.7 and Table J.9 (EN 1999-3-1)

Detail type	Type of weld	$\Delta\sigma_c$, MPa	m_1	m_2	γ_{Ff}	γ_{Mf}
9.1	Double fillet partial penetration	28	3.4	5.4	1	1
7.6	Double fillet full penetration	36	3.4	5.4	1	1

Current welding technique used by HamiltonJet for stiffening plates corresponds to detail type 9.1. Therefore, initial calculations for fatigue endurance used $\Delta\sigma_c$ equal to 28 MPa.

The total damage for each hot spot of the part is a sum of the damage for all separate events and it has to be less than 1.0:

$$D_{total} = D_{reverse} + D_{steering} + D_{pitching} < \eta \quad (20)$$

Where $\eta < 1.0$

Based on the Company's existing data points the Pitching load, LD3, is negligible. Hence, the load case LD3 was excluded from the calculations for the total damage accumulations.

Therefore, the total damage for each hot spot for the stiffened roof-plate is expressed as:

$$D_{total} = D_{reverse} + D_{ahead} + D_{steering\ PORT} + D_{steering\ STB} < \eta \quad (21)$$

Additionally, it is recommended to check welded aluminium details as per following:

- Reference stress for fatigue analysis is the principal stress in the main load carrying member.
- Weld detail stress concentrations are included in the S-N curves.
- FEA should include the surface stress on the main member in the principal direction.
- European Convention for Constructional Steelwork (ECCS) S-N curves are for "in air" or "dry" environment only.
- Parts exposed to corrosion environment are to be specially evaluated.

"It is recognised that the fatigue life of steel structures is considerably shorter in freely corroding condition submerged in sea water than in air, i.e. in dry indoor atmosphere such as common laboratory air. For steel submerged in sea water and fully cathodically protected, approximately the same fatigue life as in dry air is obtained" [40]. This statement is assumed valid for aluminium material as there is no evidence to disprove this.

3.4.6 Fatigue safety factors and material definition

There are no S-N curves provided by DNV [39]. Hence, the required information is usually obtained from other DNV-GL issued documents such as CN30.7 "Fatigue Assessment of Ship Structures", PR-C203 "Fatigue design of offshore steel structures", or Eurocode 9 "Design of aluminium structures Parts-1: General structural rules". Although the CN30.7 is for steel ship structures and specifically excludes the High Speed and Light Crafts (HSLC), it is possible to

assume that the CN30.7 methodologies for fatigue analysis are equally applicable to design of waterjets for HSLC. The CN30.7 appears to differ only in allowable factors.

PR-C203 “Fatigue design of offshore steel structures” with good agreement with Eurocode 3 and Eurocode 9 describes the Load and Resistance Factor Design (LRFD) method where load and material uncertainties are compensated by safety factors. This standard defines the Design Fatigue Factor (DFF), which for the HamiltonJet type of applications, service intervals and the way the service is done can be assumed equal to 1.0. This value is found using Table 5–8 of [22], where $\eta < 1$ and 20 years of service life are used. This means that a HamiltonJet product is designed for 50% survival probability of tested material S-N curves. Additionally, two standard deviations are deducted that increase survival probability up to 97.7%. No further S-N curve offset (reduction) is needed, unless the Company decides otherwise for a reason.

S-N data (Figure 29) below is S-N curve “D” extracted from Figure 2-8 of [22]. This standard specifies “D” S-N curve to be used for FEA as it includes stress concentration or notch factors as a result of the weld. This means that during FEA there is no need to consider any local stresses caused by weld.

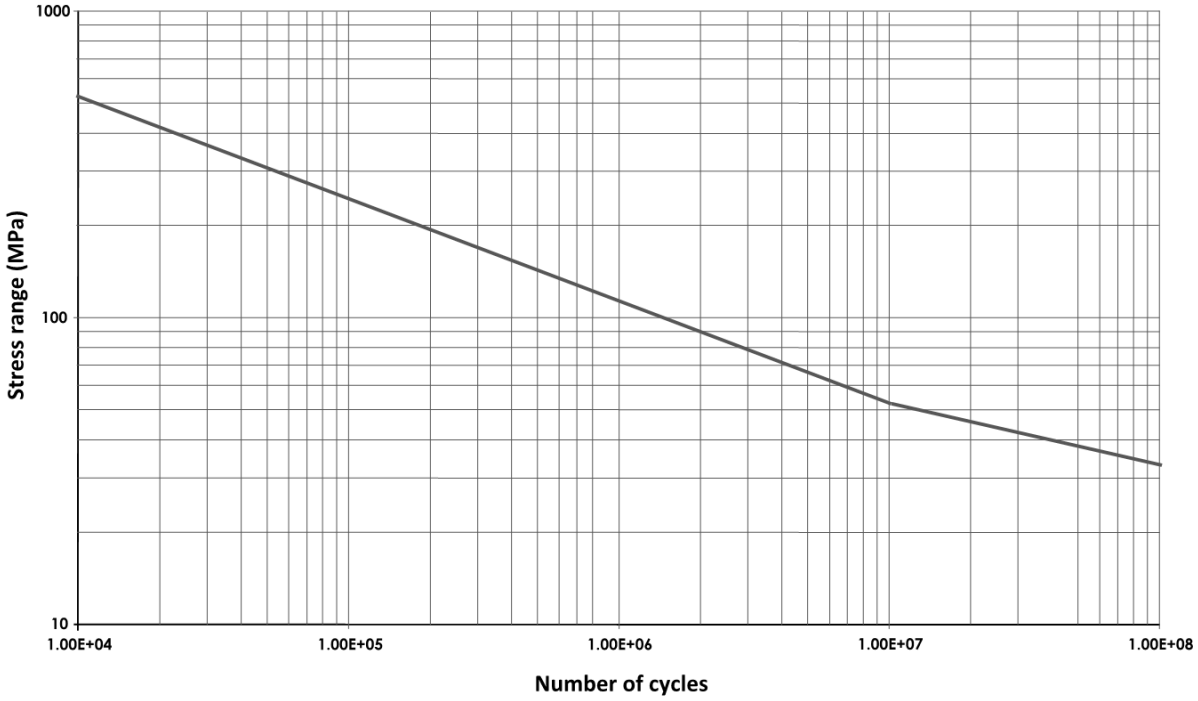

Figure 29. S-N curve “D” in air. Adopted from [22].

It is important to note that the S-N curve was taken for dry environment conditions. There are two major factors for such choice. Firstly, it is advised to use “in air” conditions when the studied structure is painted or cathodically protected [40]. Almost all HamiltonJet waterjet structures are painted with further advanced cathodic protection applied. Secondly, waterjet common installation is in such an order that the area of interest for the current study is on the dry side of the boat structure.

S-N curve above is designed as follows:

$$\log N = \log \bar{a} + m \log \Delta\sigma \tag{22}$$

$\log \bar{a}$ can be found using:

$$\log \bar{a} = \log a - 2S_{logN} \tag{23}$$

Where:

$\log \bar{a}$ = intercept of log N-axis by S-N curve

$\log a$ = intercept of mean S-N curve with the log N-axis

N = predicted number of cycles to failure for $\Delta\sigma$ (stress range)

$\Delta\sigma$ = stress range (MPa)

m = negative inverse slope of S-N curve

$2S_{logN}$ = standard deviation of $\log N$

The following values have been used for “D” S-N curve design (extracted from Table 2-1 of [22]):

- $\log \bar{a}_1 = 12.164$ for $N \leq 10^7$ and $m_1 = 3.0$
- $\log \bar{a}_2 = 15.606$ for $N > 10^7$ and $m_2 = 5.0$
- $k = 0.2$ - Thickness exponent that covers effect of the material thickness
- Structural stress concentration embedded in the detail of the S-N curve is equal 1.0

3.5 Validation approach

Validation of the solution was focused on two main aspects of this study.

3.5.1 Design for Manufacturability

The proposed solution was checked against the DFM (Design for Manufacturability) criteria such as geometry complexity of the parts, jigging, cost of materials and cost of implementation. Additionally, the possible cost for not addressing the deflection of the roof-plate was assessed using a risk management method and Company internal data.

3.5.2 Metallurgical quality assessment for the welds

In order to validate welding quality and effects of weld-on-well region two metallurgy tests were performed.

The first method was optical microscopy with grain characterisation. Grain orientation, sizing and density in the welded regions and parent material areas were compared across all samples.

The Second method was hardiness test. Values of hardiness obtained in the weld and parent material regions demonstrate changes in the rigidity of material caused by welding.

Experimental procedure and specimen preparation

For more representative results, a welded structure (Figure 30) was manufactured by HamiltonJet using the same material, techniques and procedures (Table 7) as per manufacturing of HT810 series waterjets.

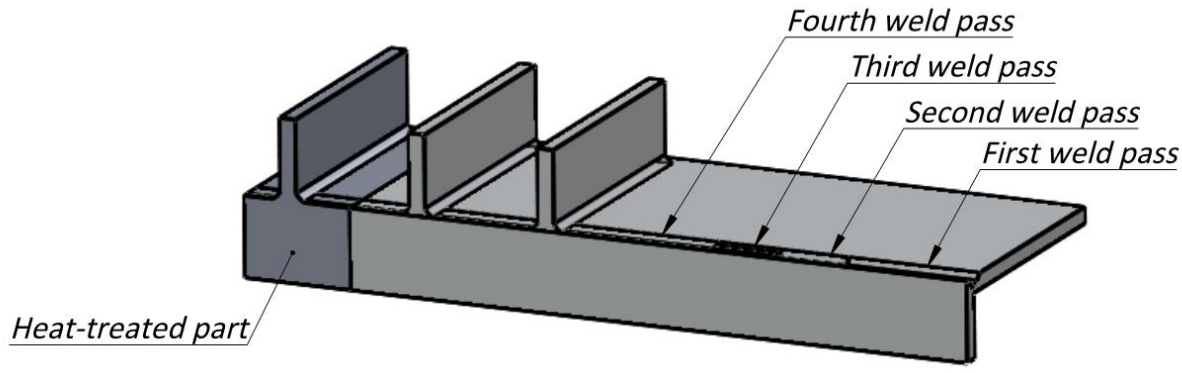

Figure 30. Welded structure (CAD representation)

Table 7. Fabrication technical data

Procedure/Technic	Specification
Base metal	Alu 5083 H112
Filler metal	5183
Weld type	GMAW
Welding voltage	24V
Shielding gases	Argon
Welding travel speed	300 mm/min
Arc temperature	4700 ^{0}C
Material temperature before each weld pass	Ambient
Heat treatment	240 ^{0}C for 4 hours

After fabrication, one part of the structure, as shown in Figure 30, was cut and placed for heat treatment at a temperature of 240 ^{0}C for 4 hours in the environment chamber. Then the heat-treated part was cooled to ambient temperature.

Specimens were cut from the structure, as show in Figure 31, using band saw. Surfaces of the interest were machined, ground by using 240–600 grid abrasive papers and then gradually fine-polished using diamond suspensions to 0.6 μm. Finally, samples were polished with aluminium oxide abrasive 15 ηm. A description of the samples is shown in (Table 8).

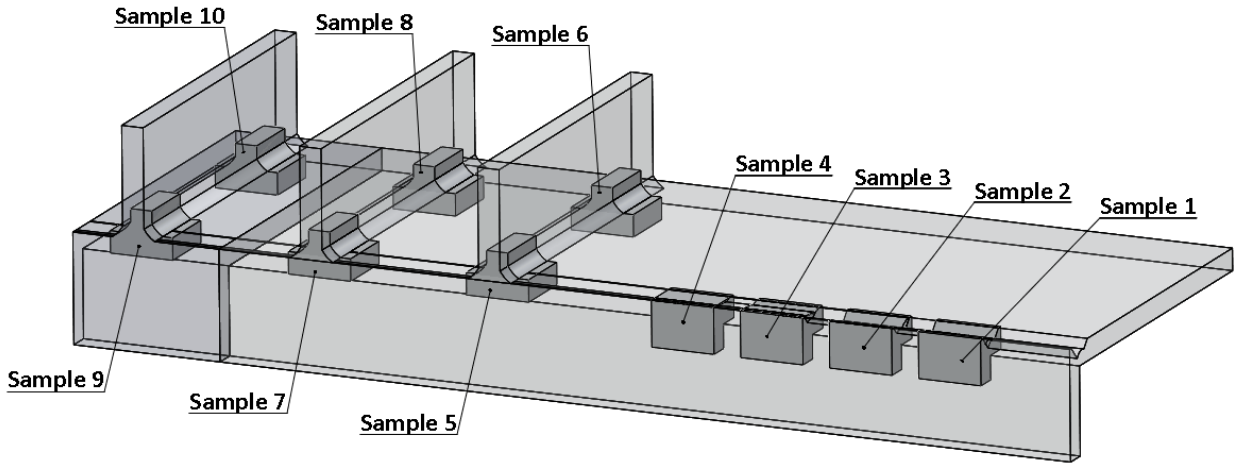

Figure 31. Test samples (CAD representation)

Table 8. Description of the cut-section

Section number	Sample	Stage of the process	Point of interest
1	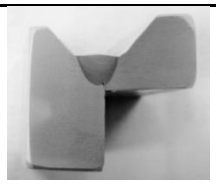	First pass of the weld applied (L1 – sample)	Base line. Property of the initial weld
2	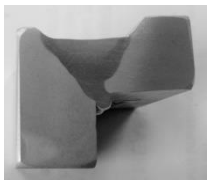	Second pass of the weld applied (L2 – sample)	Changes in properties of weld material after second pass
3	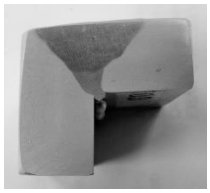	Third pass of the weld applied (L3 – sample)	Changes in material properties after third pass
4	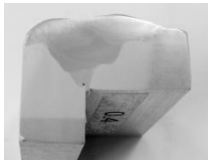	Fourth pass of the weld applied (L4 – sample)	Changes in material properties after last pass
5 – 8		Stiffener applied (T5, T6, T7, T8 – samples)	Quality and uniformity of the weld.
9 & 10	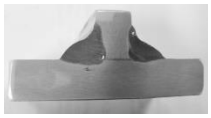	Heat treatment applied (T9 and T10 – samples)	Effect of the heat treatment on microstructure

The literature describes a number of methods for revealing the grain structure of aluminium alloys, using etchants such as Kellers, Krolls and Wecks. However, for the material under examination, AA5083-H112, none of these etchants proved to be successful. Some research such as [37] and [41] have been able to reveal microstructure using these reagents for alloy 5083 in the annealed and H12 conditions, but not for H112 temper.

Therefore the present study undertook several experimental trials using different combinations of enchants and reagents. Previous work by the research group on another difficult-to-etch aluminium, AA6082-T6, had shown that combinations of reagents and thermal soak times could be effective [38]. A similar approach was taken here to determine a suitable etchant method.

Hardness test procedure and equipment

Hardness test was done using the Vickers hardness tester (s/n HTM8874) applying the weight of 10kg and utilising the 2/3" Vickers chart. Multiple test points were determined for each weld layer and parent material region as shown in Figure 32. This approach allowed gathering of the average of the hardness results for each area.

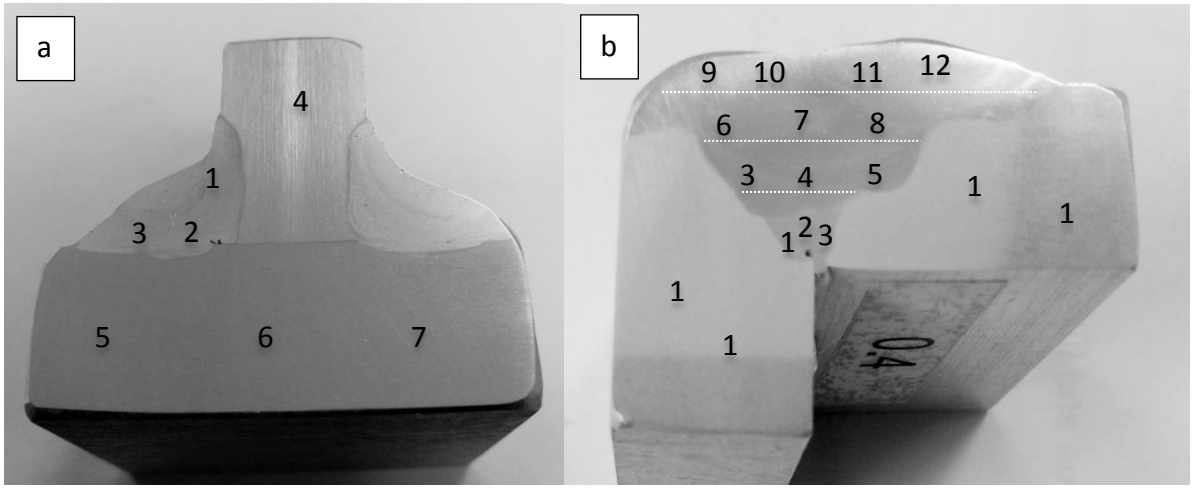

Figure 32. Test points for Vickers Hardness test: a) untreated and heat-treated tee sample; b) weld-on-weld sample

3.6 Complexities of the project

Two major challenges of the project related to stiffening of roof plate and finding a suitable etching solution have increased the overall complexity of the project in terms of time and resources required. The first problem was to find the best stiffeners arrangement that solves the problem with the roof-plate deflection. Application of the stiffening-plates introduced additional failure mode in the area of the welded joints where stress concentration points appeared. Complexity arose when performing new optimisation studies with multiple design candidates. In order to solve the deflection of the roof-plate, multiple modifications were applied to the stiffener geometry in order to reduce stresses in welded joints.

The second complex problem was the etching of the welded aluminium specimens. Although aluminium is a well-known material and multiple studies have been conducted in the past, the literature has not identified a suitable etching solution capable of revealing the microstructure under optical microscopy. Multiple trials were performed in this project to develop a new etching method.

4. Results

4.1 Analysis and localisation of load application on the waterjet model

Load cases described in sections 3.4.3 and 3.4.4 are applicable to the HT810 waterjet and include its unique set of loads (forces and pressure) acting on the different points on the jet.

Crash stop (LC1). This load case is the most extreme combination of the loads due to rapid lowering of the deflector to the bottom position while the jet provides full thrust. This act rapidly redirects a water flow underneath the boat and causes significant increase in the loads in the jet structure. However, the crash stop (LC1) is not considered in this study due to its insignificant impact on the intake roof plate as well as it not been the fatigue load due to its rare application during boat operations.

Maximum load from reverse application (LC2). Load case LC2 is a set of the static loads acting on jet (Figure 33) elements during jet operation when the deflector is fully engaged (set at the bottom position). Here and further in the study, to simplify a mesh and reduce solving time, some of the parts were removed from the model and loads acting on the missed parts were set as remote loads.

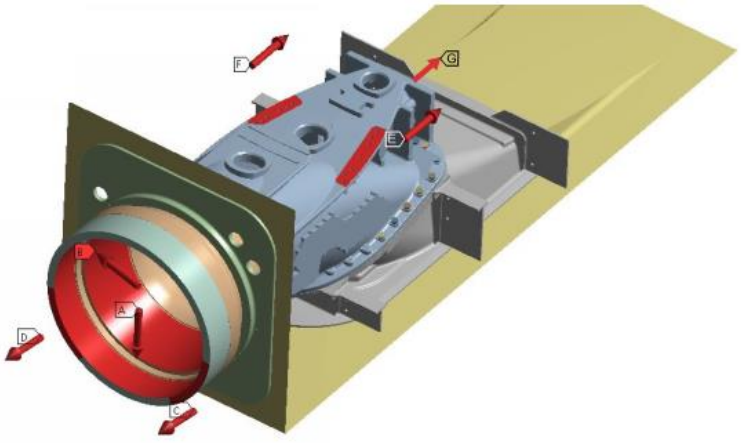

Figure 33. Reverse load case (LC2)

Loads included in the LC2 are described in Table 9.

Table 9. Loads acting to the jet for Load Case LC2

Load Description	Legend on the drawing
Axial Load on Starboard Reverse Pivot & Reverse Cylinder Load – Starboard	C
Axial load on Port Reverse Pivot & Reverse Cylinder Load – Port	D
Thrust Bearing Load	G
Reverse Cylinder Load – Port	F
Reverse Cylinder Load – Starboard	E
Vertical load on Cutlass Bearing	A
Axial load from Race & Pressure load outside Imp OD	B

Maximum load from steering (LC3). This load case is for the jet that is in the steering mode providing full thrust. Analysis for fatigue endurance must count both sub-load cases: port and starboard steering operation. LC3 for Port steering load case is shown on Figure 34 as an example. However, some load application points are the same for both and some of them are symmetrical.

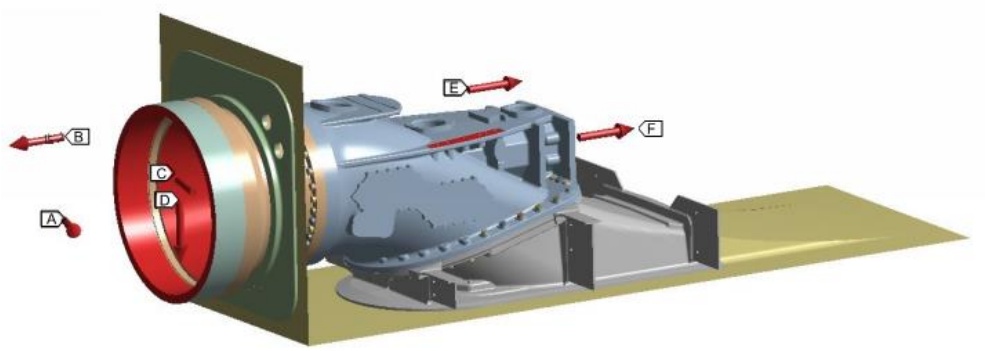

Figure 34. ***Port steering load case (LC3)***

Loads included in the LC2 are described in Table 10.

Table 10. Loads acting to the jet for Load Case LC3

Load Description	Legend in Figure 34
Axial Load from Steering Nozzle & Side Load on Tailpipe	A
Steering Cylinder Load - Starboard	E
Thrust Bearing Load	F
Steering load on the Nozzle pin	B
Vertical load on Cutlass Bearing	D
Axial load from Race & Pressure load outside Imp OD	C

Pressure distribution. It is not specified in any guidelines or rules that pressure caused by water flow must be accounted for any of the load cases described above. However, HamiltonJet experience and the current study found that the pressure on the internal surfaces of the jet exacerbates the loads as well as causing a bowing effect on the transition duct plate. Therefore, pressure distribution has been added to all load cases for more conservative results.

4.2 Finite element analysis for default roof-plate configuration

4.2.1 ANSYS setup

FEA for default jet configuration was conducting for all load cases described above.

Geometry and meshing.

Geometry of parts presented in the study were simplified or adjusted (unnecessary features such as holes and recesses removed) to allow better meshing and improve topology. Per Eurocode (EN 1999-3-1), thin shell elements were applied for sheet metal parts such as the transition duct to solve elastic structural stresses. Parabolic 8-noded elements were applied to the shell structure with mesh size equal to the plate thickness, 12 mm. Achieved quality of the mesh with 953,471 mesh elements and 1,729,336 nodes is considered as sufficient (Figure 35).

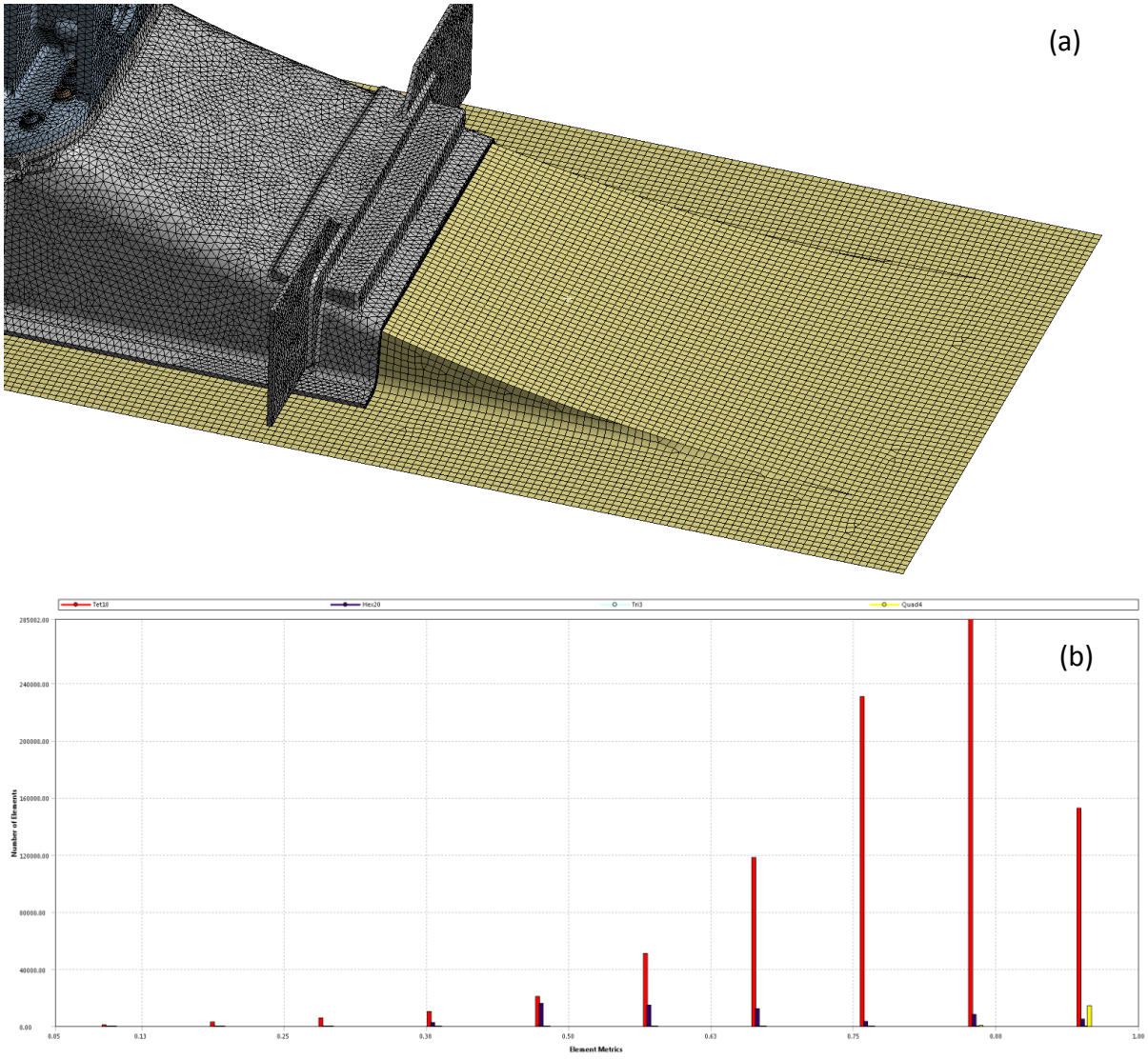

Figure 35. Mesh quality: a) Meshed body; b) Mesh metric graph

Boundary conditions and force application.

Bolt Pretention was applied to all bolts presented in the model. These bolts join the intake with the transition duct at one end and with impeller race at another. Connection for the welded joints was set as bonded contact with multi-point constraint (MPC) formulation. The fixed support was applied around the shell structure of the transition duct.

Analysis is set in two steps, where bolt pretention is applied in the first step and then outstanding forces and pressure are applied in the second step.

All load cases considered in the study are listed below:

(a) Full ahead without pressure (pressure is not applied for further comparison)

(b) Full ahead (pressure included)

(c) Pressure and ahead steering to port (LC3)

(d) Pressure and ahead steering to starboard (LC3)

(e) Pressure and full reverse (LC2)

(f) Pressure and reverse steering to port (LC2)

(g) Pressure and reverse steering to starboard (LC2)

4.2.2 FEA results for default configuration of the roof-plate

First, FEA was conducted for the load case (a) when loads acting on the jet because of full ahead mode while pressure is acting on the jet are not accounted for. This is to compare the obtained results with the load case (b) when pressure is accounted for. Such a comparison demonstrated the importance of including the pressure to all load cases. Therefore, the maximum displacement in the intake roof-plate caused by loads without the pressure is 0.75 mm whilst stresses around this area do not exceed 9 MPa (Figure 36).

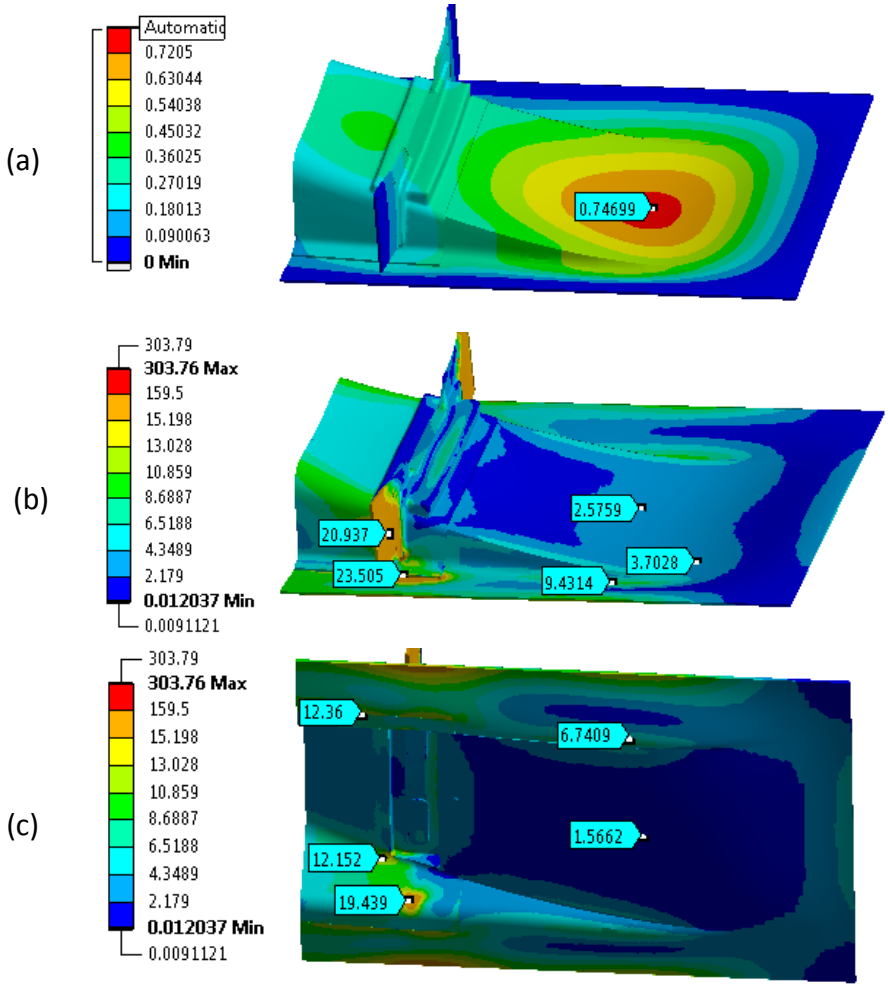

Figure 36. Graphical results of FULL AHEAD WITHOUT PRESSURE load case: a) Displacement, mm; b) Von-Mises stress, MPa (view from the bottom); c) Von-Mises stress, MPa (top view)

The next study for the same loads and applied pressure demonstrates significant differences in both displacement and stress. Hence, displacement on the roof-plate and maximum stress increased up to 3.87 mm and 26.6 MPa accordingly (Figure 37).

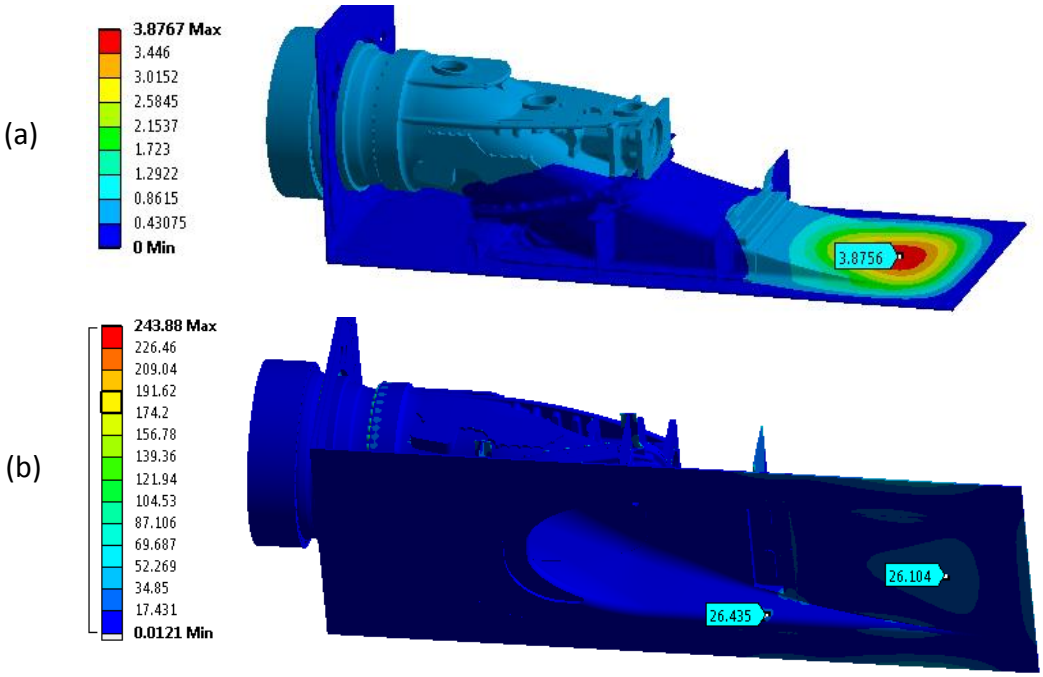

Figure 37. Graphical results for AHEAD load case: a) Displacement, mm; b) Von-Mises stress, MPa (top view)

All load cases were analysed for default jet configuration. The results are listed in Table 11.

Table 11. Deformation for the default jet configuration

LC legend	Load Description	Deformation, mm
(a)	Full ahead without pressure	0.75
(b)	Full ahead (pressure applied)	3.87
(c)	Pressure and ahead steering to the port (LC3)	3.68
(d)	Pressure and ahead steering to starboard (LC3)	3.67
(e)	Pressure and full reverse (LC2)	3.26
(f)	Pressure and reverse steering to port	3.25
(g)	Pressure and reverse steering to starboard	3.24

FEA showed that the location of the centres of deformation were consistently located in the centre line of the jet with deviation of 20mm along the centre line.

The deformation of the roof-plate appears to be independent of the side loads of the steering and reverse/steering load cases since its value appears to be similar and in a range

of 3.25–3.95 mm. Therefore, further optimisation study was based on the worst load case (b) with magnitude of the displacement of 3.87 mm.

It was initially planned to define fatigue life for the roof-plate in the default configuration. On the basis of these findings it was then planned to explore the necessity of additional reinforcement by stiffeners. However, it was found that magnitude of the displacement is too high and it may affect the flow parameters and compromise the jet efficiency. Therefore, the fatigue assessment for the roof-plate was no longer required for this load case (b) and reinforcement must be applied anyway. The acceptable value for the displacement that does not affect the flow significantly is 1.5 mm. This value is the margin of fabrication tolerance for the roof-plate.

4.3 Design optimisation for jet stiffening

The main purpose of the design optimisation of the roof-plate is an improvement of its rigidity and fatigue life. However, it is also important that the proposed solution is cost effective and practical for manufacturing and field installation. These criteria were used for the selection of the most appropriate design.

4.3.1 Stiffener orientation and positioning

Based on the established successful manufacturing practices in HamiltonJet, the distance between stiffening plates should not be less than 100 mm. This arrangement allows a fabricator to obtain an easy access to the weld region, ensuring high quality of weld pass/es while allowing welding in a fast and safe manner. Therefore, this rule was applied to all trialled solutions with two or more stiffeners.

Due to the nature of the intake design, the roof-plate is curved and stiffening plates should ideally have to be fabricated in an orientation normal to that curve. However, it adds certain complications to the job setup and can be time consuming. FEA for vertical and “normal to curve” installation of the stiffeners was conducted in order to evaluate impact on the design candidate. The study was done with pressure applied uniformly to the bottom surface and placement of the stiffeners was random but equal for both arrangements.

As shown in Figure 38, the difference in results was not significant. The Von-Mises stress for “normal to curve” ribs was 78.84 MPa and stress for vertical ribs was 78.57 MPa.

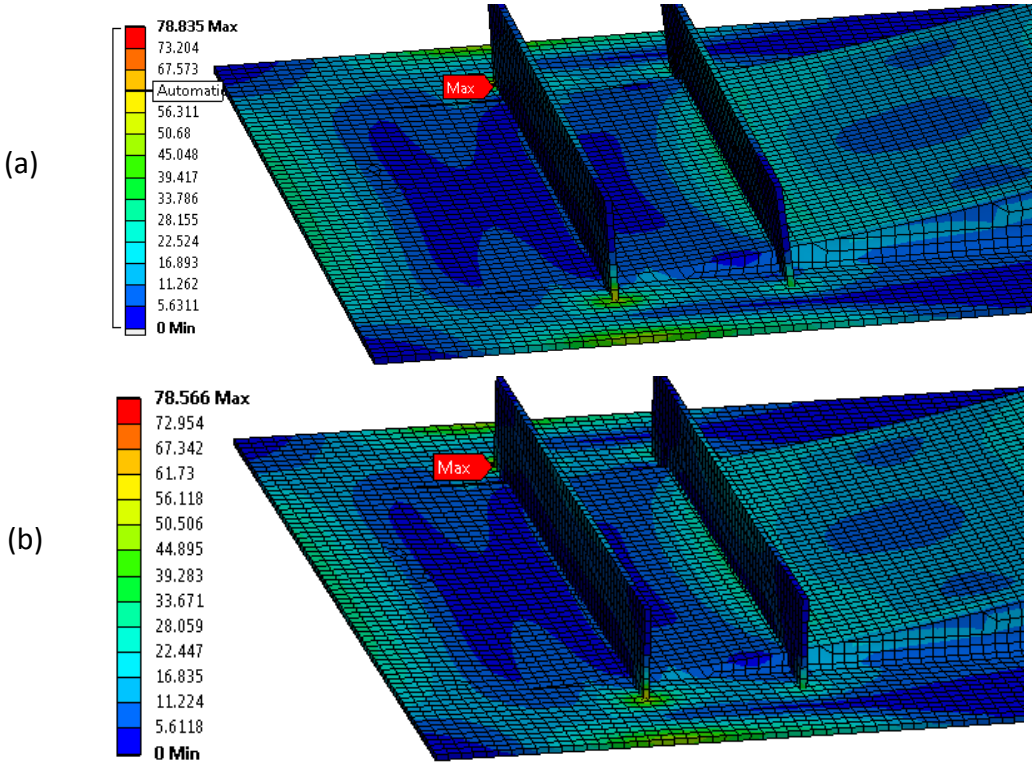

Figure 38. Stress distribution over intake for: a) ribs normal to plate; b) vertical ribs

Therefore, the rigidity of the structure is not compromised and stiffeners can be oriented vertically for manufacturing purposes.

In addition, the stiffener orientation study revealed that ribs placed *only* on top of the roof-plate (Figure 39a) tended not to prevent roof deflection. However, the extension of stiffeners was found to significantly reduce roof-plate deflection (Figure 39b).

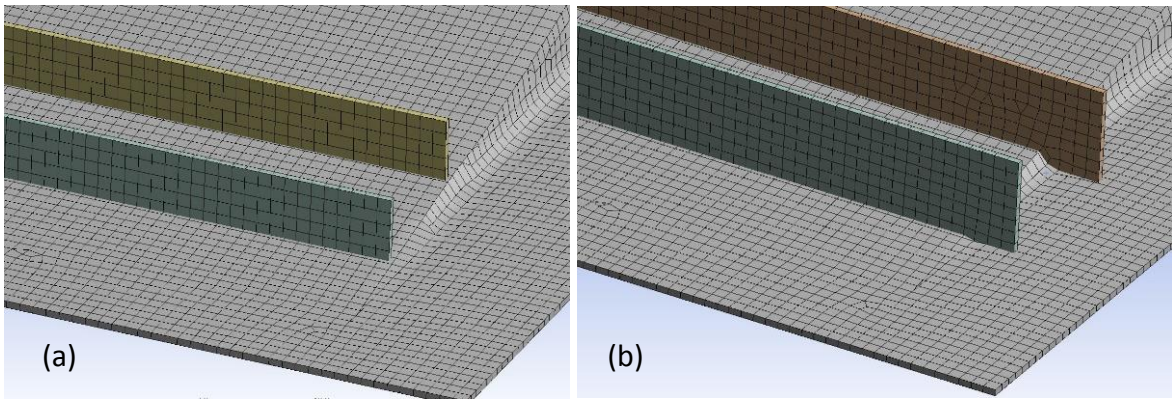

Figure 39. Stiffener types: a) basic; b) extended

Positioning the stiffeners orthogonally as described in [13] was considered as not being practical due to its high complexity.

4.3.2 Stiffener quantity

Studies with single, double and triple stiffeners were conducted in order to define the optimum solution.

Single stiffener arrangement results

Two study attempts with single stiffener showed no significant improvements in the reduction of displacement.

In the first attempt, a stiffener was placed in the point of maximum displacement (*X*=3447). This solution reduced displacement to 2.2 mm and moved the centre of the displacement further up (Figure 40).

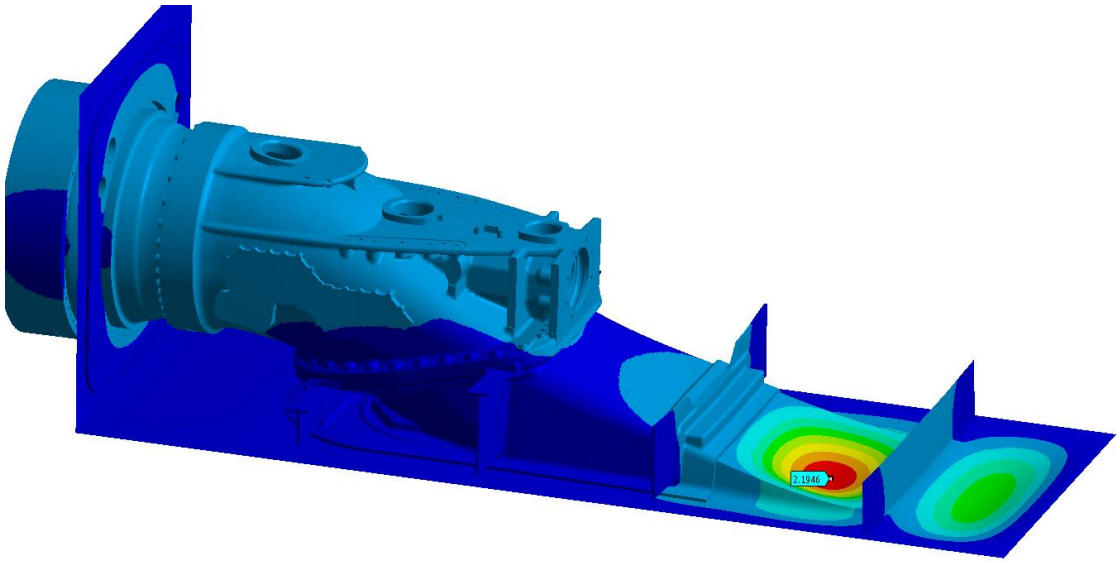

Figure 40. Graphical result of displacement for single stiffener placed in original centre of displacement

The second placement of a single stiffener was in the centre of the maximum stress on the top surface of the roof-plate that appeared 175 mm further up from the original centre of the displacement (*X*=3272). The result of this study was similar to the first attempt, with the only difference in the location of the centre of the new displacement. As shown in Figure 41, the centre of the displacement moved in the opposite direction with the magnitude of 2.3 mm.

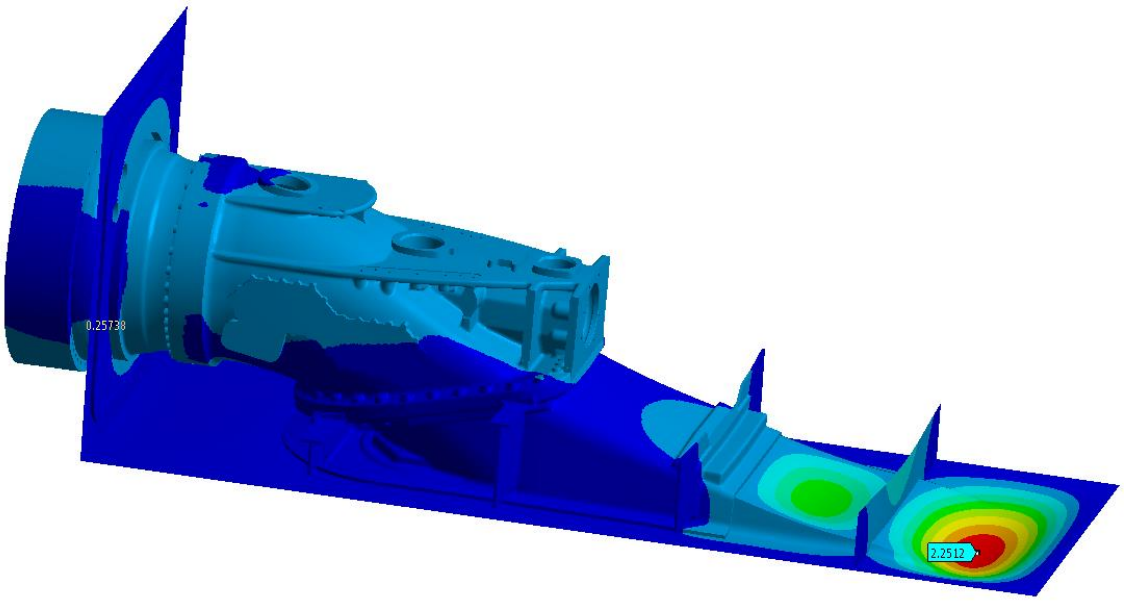

Figure 41. Graphical result of displacement for single stiffener placed in the centre of the maximum stress on top surface

Therefore, the solution with the single stiffener was not found to be acceptable and additional stiffening was required.

The next step was increasing the number of the stiffeners to two. This task significantly increased the complexity of the analysis, as multiple options of positioning the stiffeners were possible. However, in order to assist with the analysis and reduce the time of calculation, the techniques in the ANSYS such as Submodel and Design Exploration tools (optimisation) were utilised.

Using parameter optimisation in ANSYS, twenty design candidates were created. Input parameters for the study were distances of each of the stiffeners from the model origin and output parameter was Total Deformation. Distances for the stiffeners were set in order to assure the distance between them was not less than 100 mm as specified in section 4.3.1.

Double stiffener arrangement results

Optimisation study for double stiffeners with multiple design candidates and ANSYS Response Surface Tool found that the optimal displacement of 1.52 mm was achieved when stiffening plates are set in X_1 = 3120 for first rib and X_2 = 3540 for second rib (Figure 42).

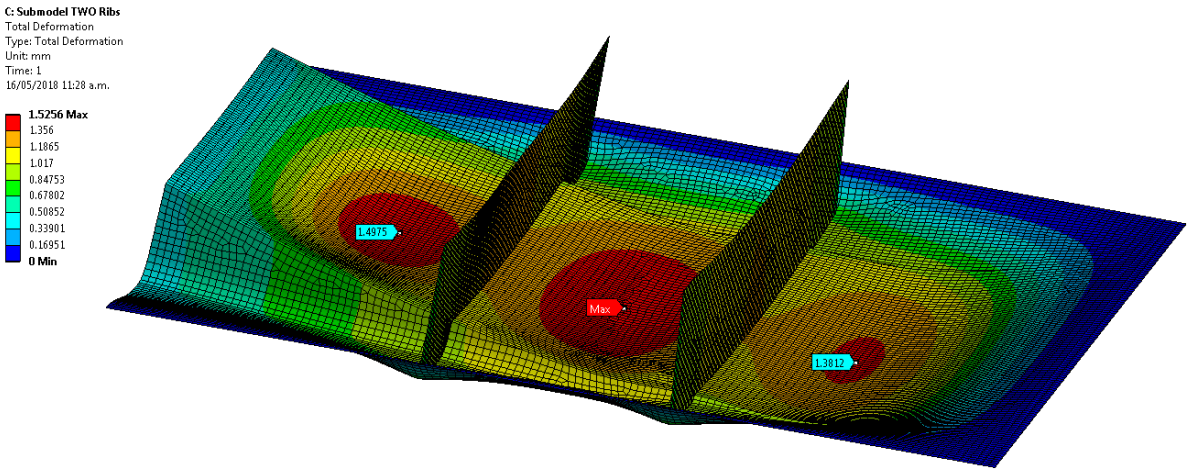

Figure 42. Double stiffeners. Displacement results (magnification x64)

The results achieved the target of 1.5 mm and were considered for the further fatigue analysis.

Triple stiffener arrangement results

The optimisation for three stiffeners included over 40 design cases. Analysis of the results (Figure 43) and the Response Surface defined the optimum location for all three stiffening plates at $X_1=3020$ for the first rib, $X_2=3280$ for the second rib and $X_3=3580$ for the third rib with displacement across ribs surrounding areas in range from 1.20 to 1.34 mm (rounded).

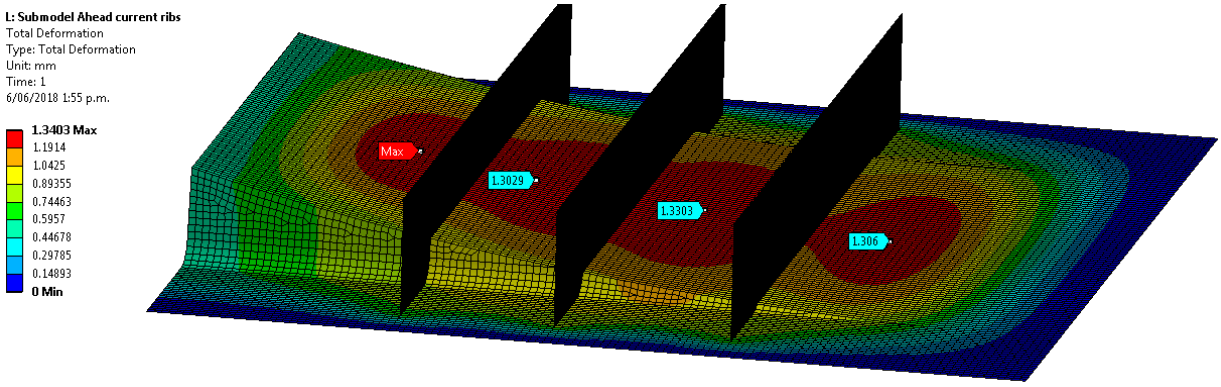

Figure 43. Transition duct stiffened by 3 stiffeners. Displacement results

Results for triple stiffeners were considered for further fatigue analysis.

4.4 Fatigue assessment for design candidate

During stiffening optimisation study, stress concentration areas (hot spots) appeared at the points where ends of the stiffeners jointed the base-plate for all design candidates (Figure 44). The values of the equivalent stress at the hot spots laid in the range from 138 MPa to 146 MPa.

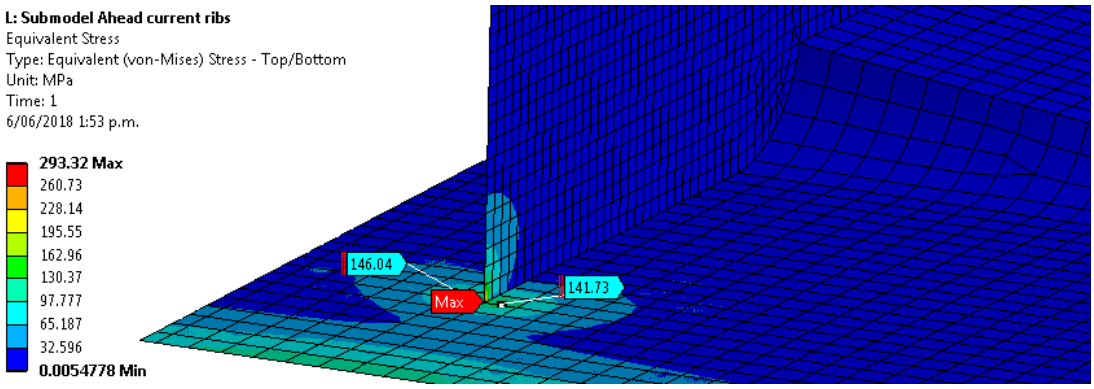

Figure 44. Stress concentration areas for the stiffener.

Fatigue calculation for weldments as per DNV-GL standard was not conducted for this design candidate due to location of the stress concentration in the weld region. Therefore, geometry of the stiffeners either needed to be optimised in order to reduce stress in the weld toe area or should be shifted to stiffeners, away from joints.

For eliminating this issue, a C-shape cut-out (Figure 45) in the stiffening plate above the weld was adopted.

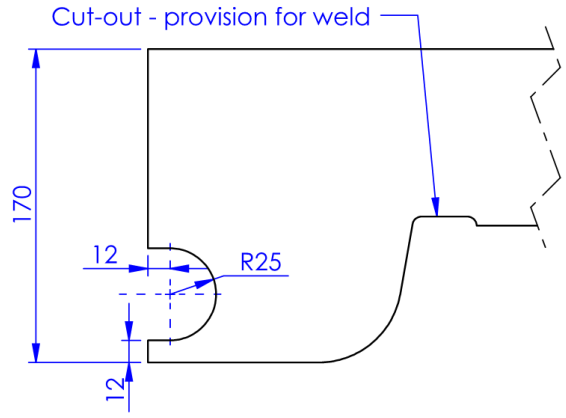

Figure 45. C-shape cut-out for stiffening plates

For this purpose, additional analysis for the stress distribution was performed on the modified stiffeners (Figure 46).

Results shown in Figure 46 demonstrate that the stress concentration area shifted from the joint to the introduced C-shaped cut-out. Stress magnitude in this region was well below the yield point with a shift to the stiffening plate. Hence, the area with stress concentration was not included in further fatigue analysis. However, the fatigue analysis for this design candidate revealed that stress range in the weld toe area, despite stress reduction, was still not sufficient due to reduced lifetime with usage, ɳ, over 3 and life expectation of 6.5 years.

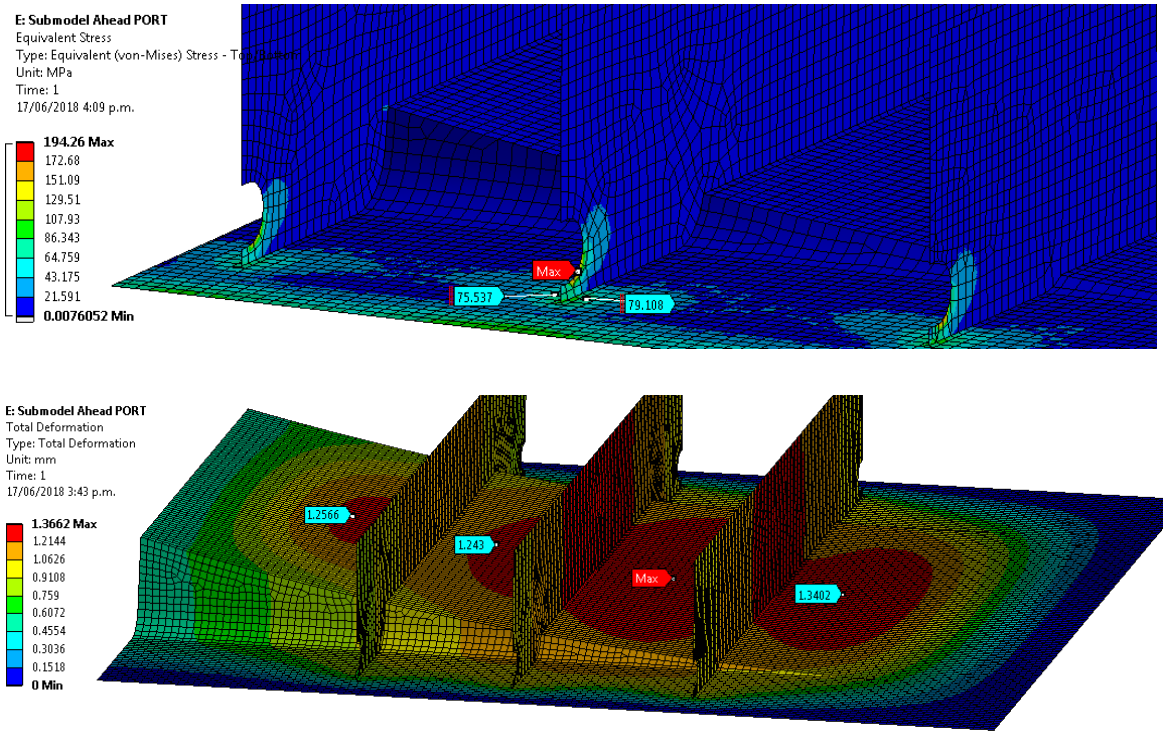

Figure 46. Transition duct stiffened by ribs with C-shape cut-out: a) Stress distribution; b) Total deformation.

Further geometry modification to stiffening plate was applied as shown in Figure 47.

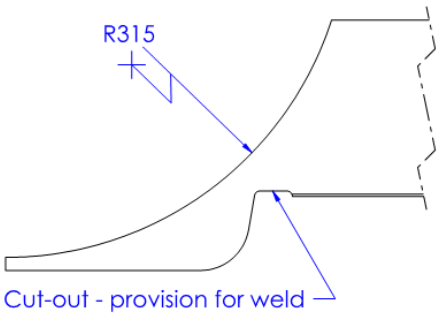

Figure 47. J-shape cut-out for stiffening plates

This shape provided better fatigue endurance results with $\eta = 0.87$ that is equal to 22.9 years of safe life (Table 19, Appendices A2) with maximum roof-plate deflection of 1.6 mm (rounded).

Further analyses with four ribs did not reveal any noticeable improvement in roof-plate displacement and fatigue life.

Therefore, the most optimal solution in relation to deflection as well as fatigue life was reinforcement with three ribs with J-shape at the end of the plate (Figure 48).

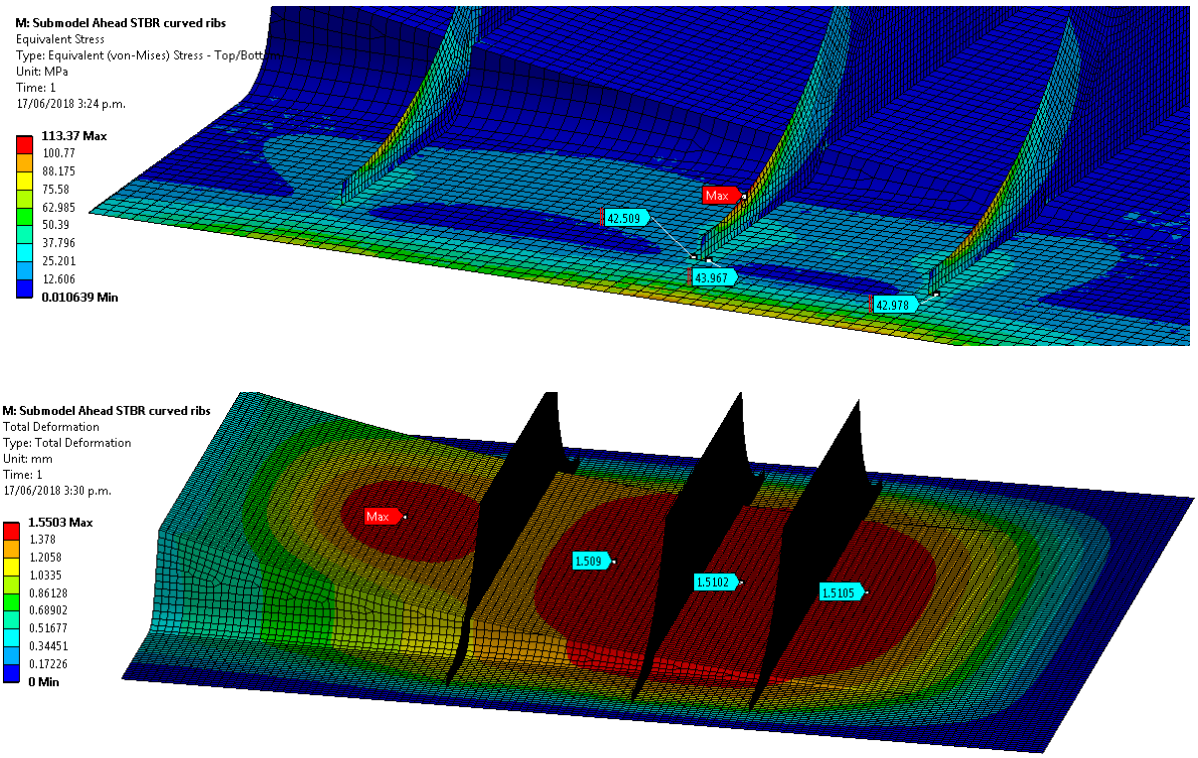

Figure 48. Intake duct stiffened by ribs with J-shape cut-out: a) Stress distribution; b) Total deformation

Although this solution still did not meet the target for the maximum deflection of 1.5 it was considered to be successful as a deviation of 0.1 mm from target is negligible.

As could be seen in Figure 48, the location of the stiffeners with J-shape cut-out is different from the location of the stiffeners without modification (Figure 43) and stiffeners with C-shape cut-out (Figure 46). This means that any modifications that were applied to the geometry of the stiffening-plates change roof-plate characteristics and arrangement of stiffeners needs additional adjustment.

4.5 Design evaluation

4.5.1 Proposed design details and requirements

Introducing stiffening plates to the jet structure will lead to changes in manufacturing process by adding additional technological steps. These steps may include:

a) Producing three stiffening plates with a defined J-shape cut-out for all three plates but with unique cut-outs that repeat transition duct geometry (Figure 49).

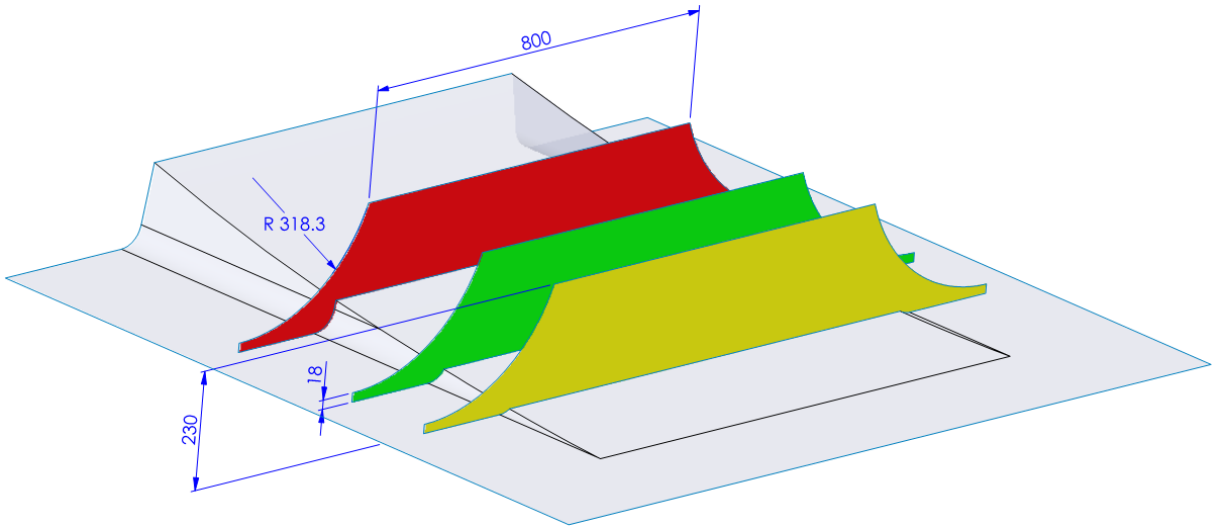

Figure 49. Stiffening details: a) Stiffeners profile details; b) Stiffener details in cross-section view

Due to the thickness of the plate (12 mm), waterjet cutting is not applicable and laser-cut manufacturing processes can be used.

b) Introducing jigging to the manufacturing. This includes: one-off cost for jig design and jig implementation; and ongoing cost for jig setting-up for every transition duct fabrication. Proposed positioning of the stiffening plates is shown in Figure 50. Cost break down is discussed below.

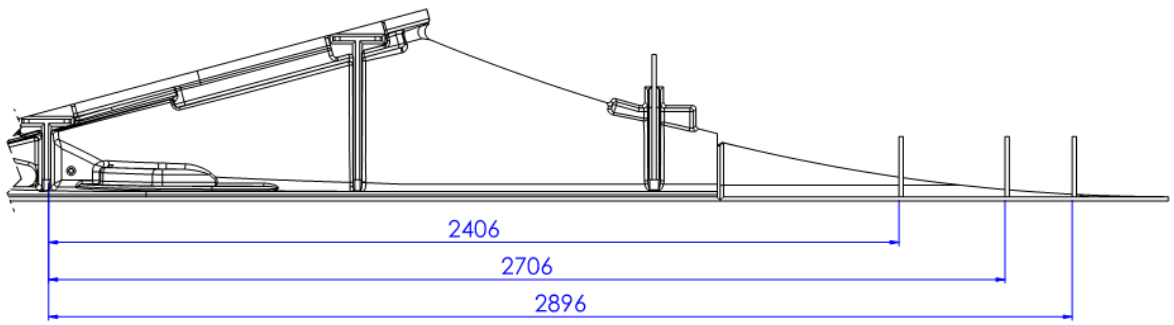

Figure 50. Proposed arrangement for the stiffening plates with J-shape cut-out

More detailed drawings for proposed solution are not included in this paper due to intellectual property constraints.

4.5.2 Cost estimation

Cost of adding the stiffeners

Cost estimation is based on the data provided by HamiltonJet for normal production workflow.

Table 12. Fabrication cost break down, NZD

	Time (h)	Cost per hour (NZD)	Operational cost (NZD)	Cost			
				Laser cut profile (each)	One rib	Two ribs	Three ribs
Material	n/a	n/a	n/a	32	32	64	96
Stock & storage	.1	20	2	n/a	2	2	2
Jigging	re-used	re-used	0	n/a	0	0	0
Welding labour	0.31	74	22.94	n/a	22.94	45.88	68.82
Setup	2	50	100	n/a	100	100	100
Post welding	0.5	50	25	n/a	25	37.5	62.5
				Total cost	**$179.94**	**$247.38**	**$327.32**

Note that welding time is calculated using estimated length of the weld path 930 mm and travel speed 300 mm/min. This estimation is based on the data collected from the fabrication department over the years and accounted for different fabricator's skills and experiences.

Cost of not adding stiffeners

The consequences of not reinforcing the roof-plate might lead to serious impact on both parties – producer and customer. HamiltonJet could be negatively affected by aspects related to lost revenue due to repairs done under warranty (20 years) as well as reputational damage, which might result in subsequent loss of sales. HamiltonJet customers can also be affected by unexpected repairs over the period of provided warranty. One other potential issue can relate to increased fuel consumption due to changes in geometry of roof plate, which in turn may result in additional costs and dissatisfaction.

The following table, which applies a risk management method, lists some common risks associated with not adding stiffeners to the roof plate.

There are no data for the consequences and likelihood, hence estimates have been made based on discussion among the engineers involved in the commissioning and experience in the shipyard processes. Regarding likelihood, no failures have been observed in the 144 units for 8 years, hence likelihoods have been estimated as low.

Table 13. Consequence risk management table

Risk	Consequence [C]	Likelihood of the consequence over the design life (20 yrs) [L]	Risk [CxL]
Cost to the customer			
Harmful modifications by customer	Potentially crack to the duct, deformation of duct shape (loss of efficiency). Remediation cost for HJ may involve a new duct, damages to loss of use of asset, or legal court costs $400,000	This has not happened yet, but cannot be discounted to zero because of inability to control the shipyard 1/100	$4,000
Repairs outside warranty	Repair cracks (dry dock, welding) $50,000	1/500	$100
Flow parameters compromised	Increased fuel consumption (over 20 years) $40000	1/10	$4000
Cost to the producer			
Repairs done under warranty	Repair cracks, leakage (dry dock, welding) $20,000	1/500	$40
Reputational damage	Loss of other sales. Loss of market shares. $2,000,000	1/500	$4,000
Total			**$600**

4.6 Metallurgical validation

4.6.1 Development of etchant method

It was found that there is no single solution that can successfully reveal grains in this particular parent material and in the weld regions. Therefore, two main methods were developed as shown in Table 14:

Table 14. Welded aluminium 5083 etching methods

	Step 1	Step 2
Base material	Wecks reagent – 12 sec	50% aq Nitric Acid with distillate water – 3 sec
Weld region	Krolls etchant – 40sec	Wecks reagent – 15 sec

Additionally, during etching trials, it was found that layers of the material in the weld regions for weld-on-weld specimen (sample 4, Table 8) response to the etching differently. Thus, more etching time is required for every weld pass. For example, for the first weld pass region method described in Table 14 is valid. For the second and third weld passes regions another 15 sec in Krolls enchant and then 10 sec in Wecks reagent are required. Additionally, the repetition of the previous step is needed for the last (fourth) welded pass.

This new "dynamic" method has its own limitations. Thus, it was observed that once the last weld layer has been etched and grain structure has been retrieved successfully, the first and second weld passes were observed to be over-etched (burnt). That means that examination of the first two layers of the specimen is not possible any more.

4.6.2 Optical microscopy with grain characterisation

Seven surfaces were examined by optical microscopy. All figures below refer to Figure 51, where weld areas are highlighted in pink and all areas of interest are numbered.

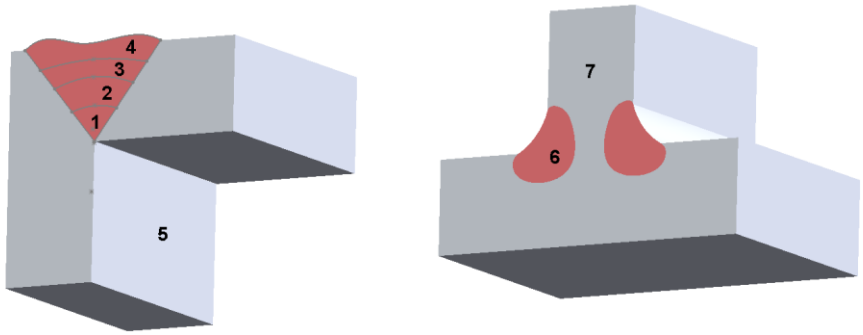

Figure 51. Areas of microscopy investigation: 1 to 4 - Weld-on-weld region; 5 - normal to rolling direction: 6 - weld region on heat treated specimen

Figure 52a below illustrates the primary microstructure of the 5083 alloy consisting of rough grains of the wrought aluminium with an average size of 150 microns (red arrow). Different colours of the grains (yellow arrows) imply the different crystallographic orientations as a result of the mechanical work during material hardening such as rolling or extrusion. The post fabrication heat treatment creates a more uniform texture (Figure 52b) with modified grain orientation. Additionally, the rough grains have been altered to a more uniform morphology with an average grain size of below 100 microns (red arrow Figure 52b).

Similar to Figure 52, the heat treatment process caused some changes in the microstructure of the alloy utilised on area 7 in Figure 51.

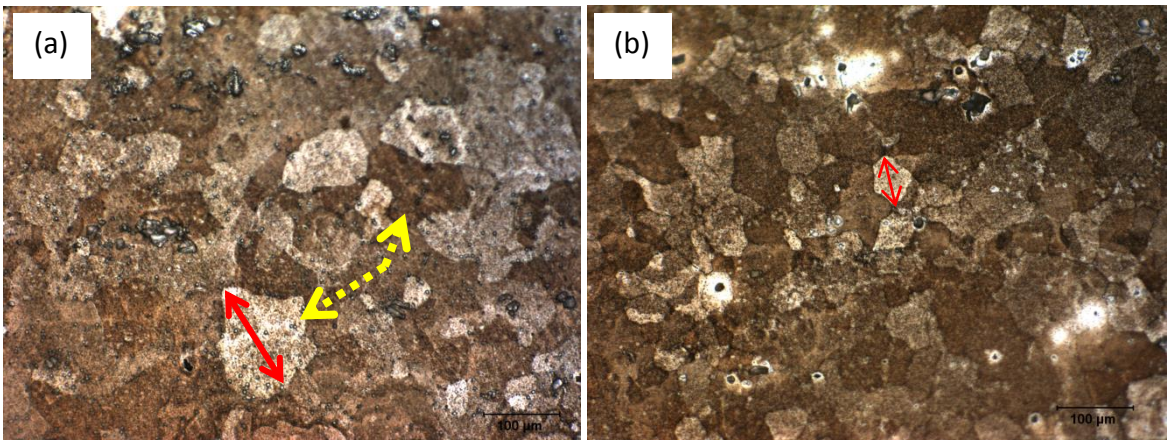

Figure 52. Optical micrographs of base material (view on area 5, Figure 51): a) raw material; b) Heat-treated material

However, these changes mainly affected precipitates (secondary phase) rather than grain morphology or size.

A comparison between Figure 53a and Figure 53b shows that the columnar grain morphology (as a result of directional rolling) and the average grain size (several hundred microns) remain unchanged before and after the heat treatment. However, it is clear that the precipitation behaviour during the heat treatment changes.

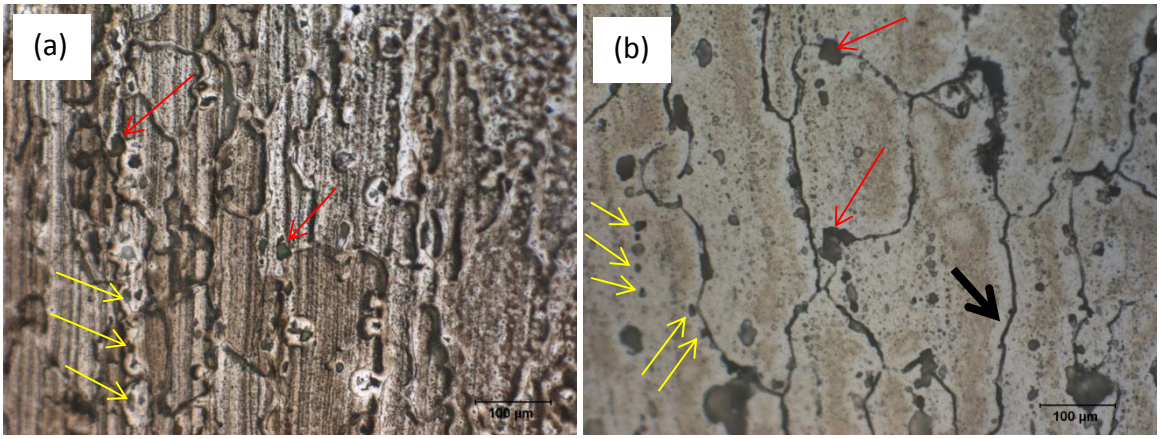

Figure 53. Optical micrographs of base material (view on area 7, Figure 51): a) Raw material; b) Heat-treated material

In general, it is found that the microstructure contains two different precipitate particles. The large precipitates, which are spherical shaped and distinctly distinguishable with a dark colour, nucleated at the position of grain boundaries (red arrows Figure 53). Another kind of small precipitates are situated inside of the grains and surrounded by the blister-like regions

at their proximity regions (yellow arrows). These bright regions around small precipitates are formed by segregation phenomena inside the grains where alloying elements migrated to the precipitate.

The microstructure of the heat-treated specimen (Figure 53b) shows that the micro-segregation areas around the secondary precipitates almost disappeared after heat treatment was applied. Moreover, it is clear that the primary precipitates (red arrows) remained stable during the heat treatment process. Additionally, these micrographs reveal that the grain boundaries of the heat-treated microstructure possess a suitable integrity and continuity (black arrow).

Figure 54 shows the microstructure of different layers of the weld passes from weld root (a) towards the weld crown (d). The first and final layers experience higher cooling rates compared to the layers that are in between. The first layer was deposited on the work piece that was a main source of the heat sink. Similarly, the final layer on top of the weld region was directly in contact with the free circulating air that provided a faster cooling rate for layer 4 in comparison with layers 2 and 3 in the middle of the weld.

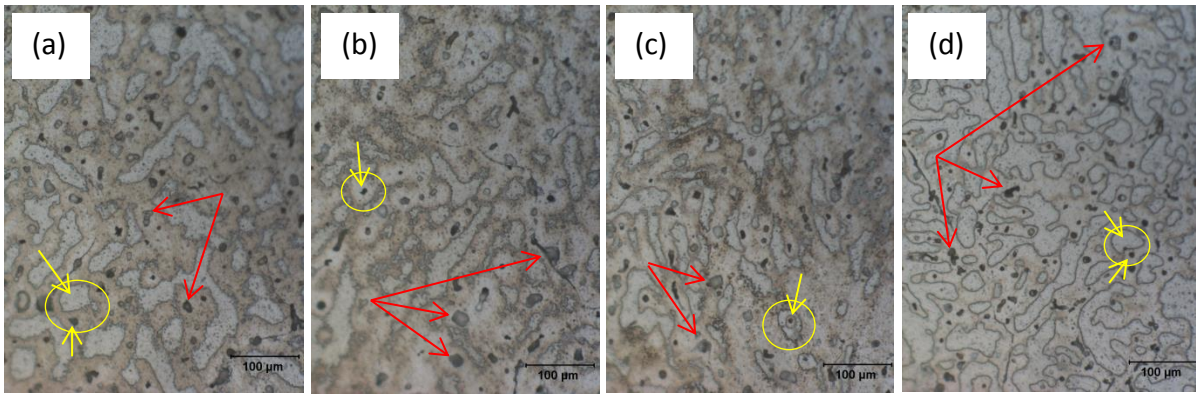

Figure 54. Optical micrographs of base material (view on points 1–4, Figure 51): a) 1st weld pass; b) 2nd weld pass; c) 3rd weld pass; d) 4th weld pass. Micrographs show primary precipitates (red arrows) and secondary (yellow).

The comparison between the precipitates shows that the quantity of primary precipitates in the middle layers (Figure 54b,c) is significantly bigger than in the outer layers (Figure 54a,d). Primary precipitates are indicated in Figure 54 by using branched arrows in red.

The comparison also shows that the secondary precipitates are also formed through the weld regions. The formation mechanism of these particles could be elucidated by a comparison between the layers. As the yellow circles on Figure 54 show, the solidification

front creates island regions and secondary precipitates (yellow arrows) across all weld passes. Due to slow release of heat flux in the middle of the weld, these solidified islands can surround the secondary precipitate particles in the inner layers as shown in Figure 54b,c. In the outer layers, the secondary precipitates do not have enough time to enter the inside of the island zones due to the high cooling rates in these regions. Hence, precipitates are deposited in the proximity of the islands (Figure 54a,d).

Figure 55 shows the micrographs of the weld region in the heat-treated sample. The distinctiveness between heat-treated and untreated samples is the existence of dendrite-like islands (black arrows) formed during the heat treatment. A close look at the border of the dendrites reveals that the primary coarse precipitates (red arrows) are laid outside of the dendrites. Such diffusional behaviour is the result of the formation of the dendrite shapes by migration of the single phase islands and then combining them together.

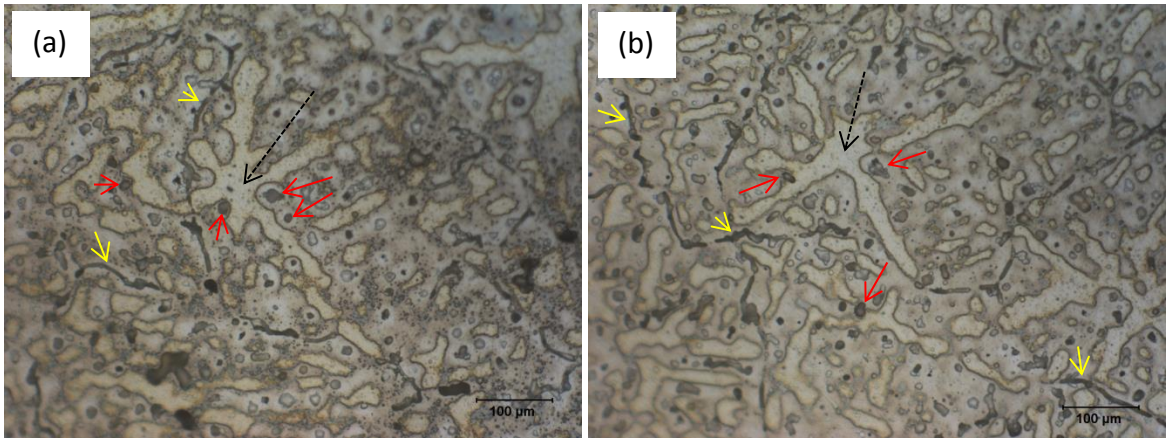

Figure 55. Optical micrographs of weld region on heat-treated specimen (view on points 6, Figure 51): a) close to the edge; b) close to parent material. Micrographs show dendrite-like islands (black arrows), primary coarse precipitates (red arrows), and needle-like dark phase (yellow arrow).

Additionally, the formation of the needle-like dark phase (yellow arrow, Figure 55) was observed in the heat-treated samples. This feature can also be related to the diffusion behaviour of the heat treatment process. Such a process results in decomposition of the secondary precipitates and ejected particles from the island zones and then joining together in a form of a transformed precipitate phase in the shortest diffusional path (linear) as the preferred direction of the precipitation and growth.

As all metallographic micrographs were examined in dark-field illumination, it might be that these dark spots are some pitting result of etching, which causes a misunderstanding for

presented metallurgical interpretation. Figure 56 shows an examination of the distribution of precipitates under a bright-field illumination, which distinguishes precipitates from pitting voids.

As shown in Figure 56, the precipitate phases (dark arrows) appear in the same size and morphology as in the previous micrographs. However, the etching pits also revealed bright-field (red arrows) in a uniform distribution through the background, which were not observed before in dark-field micrographs. This confirms that initial interpretation was not affected by mistaking the precipitate particles with corrosion pitting features.

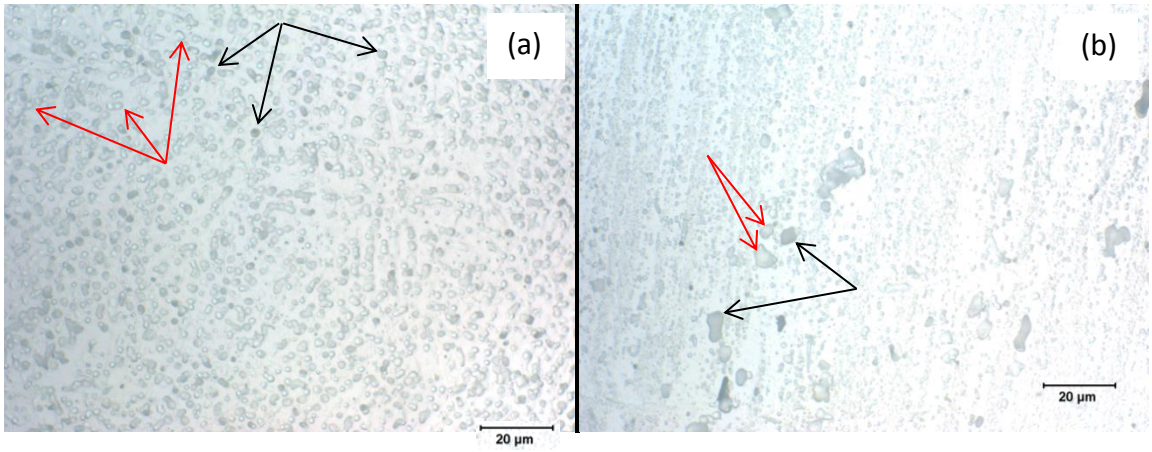

Figure 56. Optical micrographs of precipitance: a) Weld region, view on points 6, Figure 51; b) Base material, view on points 7, Figure 51. Micrographs show the precipitate phases (dark arrows), and etching pits (red arrows).

Morphological analysis of the welded samples confirms the sufficient quality of the welds. Detailed optical examination of the weld-on-weld areas did not reveal any porosities or defects in the material.

4.6.3 Hardness Test results

It was found that hardness of the first weld pass decreases after an application of the second pass (sample L2, Table 8) but increases for the next two weld passes (samples L3 and L4). Similar behaviour was seen for the second weld pass in samples L3 and L4. However, the third pass showed opposite results and slight increase in hardness was presented (Table 15, Appendices A1).

The average of the hardness for welded regions is 72.3HV_{10} and it is calculated using results from L4, T5, T6, T7 and T8 samples (Table 15 and Table 16, Appendices A1).

The hardness of the weld regions in the L4-sample material can be represented as a chart (Figure 57).

Figure 57 shows that hardness of the material in the first and fourth weld passes was higher than in the middle of the welled specimen. This corresponded well to the material microstructure shown in Figure 54 and described above in section 4.6.2.

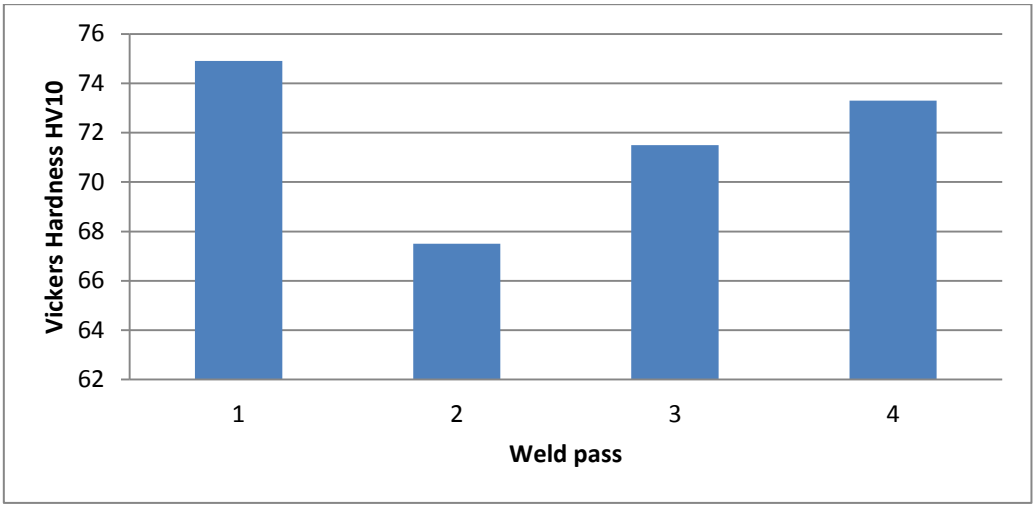

Figure 57. Hardness of the material across 4 weld passes (L4-sample)

Parent material regions were also investigated across all untreated specimens (Table 17, Appendices A1), including T-shape and L-shape samples. The average of the hardness for the parent material region is 76.6HV_{10} with standard deviation equal to 1.82.

Heat-treatment applied to the welded joints improved hardness of the weld region from 72.3 to 74.1HV_{10} but did not make any significant difference to the parent material with magnitude of 76.7 HV_{10} (Table 18, Appendices A1). The parent material is cold-form hardened (H112) and heat treatment could not make any better precipitation.

Based on the empirical data obtained from the tests on heat-treated specimens (Table 18) the loss of the hardness in the welded region is 3.4%.

5. Discussion

There is a need to determine the optimum arrangement for the stiffeners that are required to reinforce the transition duct, considering all loads, ship Classification Society requirements for stress, installation constraints and manufacturing considerations such as weld types, weld access and stiffener profiles.

5.1 Outcomes

The current study aimed to evaluate the default arrangement of the roof-plate of the transition duct and apply stiffening ribs if it is necessary. During evaluation using FEA and DNV-GL and Eurocode methodology, it was found that stiffening ribs are necessary for the roof-plate. Loads and pressure applied to the roof-plate lead to bowing of the plate with magnitude of 3.86 mm. Hence, the flow characteristics are likely to deteriorate and the designed jet efficiency may be compromised. However, the exact impact on the water flow through the jet was not studied in detail.

5.1.1 Stiffening the roof-plate

There was a need to stiffen the roof-plate. Due to complex geometry of the roof-plate and non-uniform pressure distribution it was not possible to utilise any of recommendations from the existing literature such as [12] or [13]. From considerations of manufacturability, it was decided to adopt a general design concept of welded stiffening plates (ribs).

The present project determined the number of ribs and the spacing thereof to reduce the deflection to 1.5 mm, which is the manufacturing tolerance. The large potential solution space was searched using an FEA optimisation study.

Number of ribs

It was found that the optimum number of the stiffeners required to reinforce the plate is three. The deflection magnitude is reduced from 3.87 mm to 1.6 mm after stiffening in this way (Figure 58).

This solution does not fully eliminate the bowing effect of the roof-plate but discussions within the firm confirm that it is likely to be sufficient. The residual deflection is close to the target, and is within the manufacturing tolerances of the setup jigs and fixtures, i.e. is within

existing quality tolerances. It would be possible to reduce the deflection further by the addition of more ribs. However, the reduced deflection would not be measured by the existing quality systems, and more precise fixtures would be required. It is not clear that this would add any value. Furthermore the additional ribs would increase the manufacturing cost, via increased material and time. It would also potentially cause more difficult welding conditions, hence introduce other defects and require additional quality checks to exclude these.

Spacing of ribs

The optimum distances between ribs were obtained by FEA, using ANSYS Optimisation Tools.

The coordinates of first, second and third ribs along X-axis from model origin (refer to Figure 20 for more details) are X_1=3120, X_2=3420 and X_3=3610 respectively.

Additionally, distances between the ribs were found to be not equal. As an example, the distance between the first and second ribs is 300 mm, and between second and third it is 190 mm. This means that regardless of the jet size, any reinforcements by stiffening plates for a roof-plate with complex geometry need to be carefully calculated. This calculation should account for multiple parameters such as pressure distribution, geometry of transition duct, and impact of operation loads.

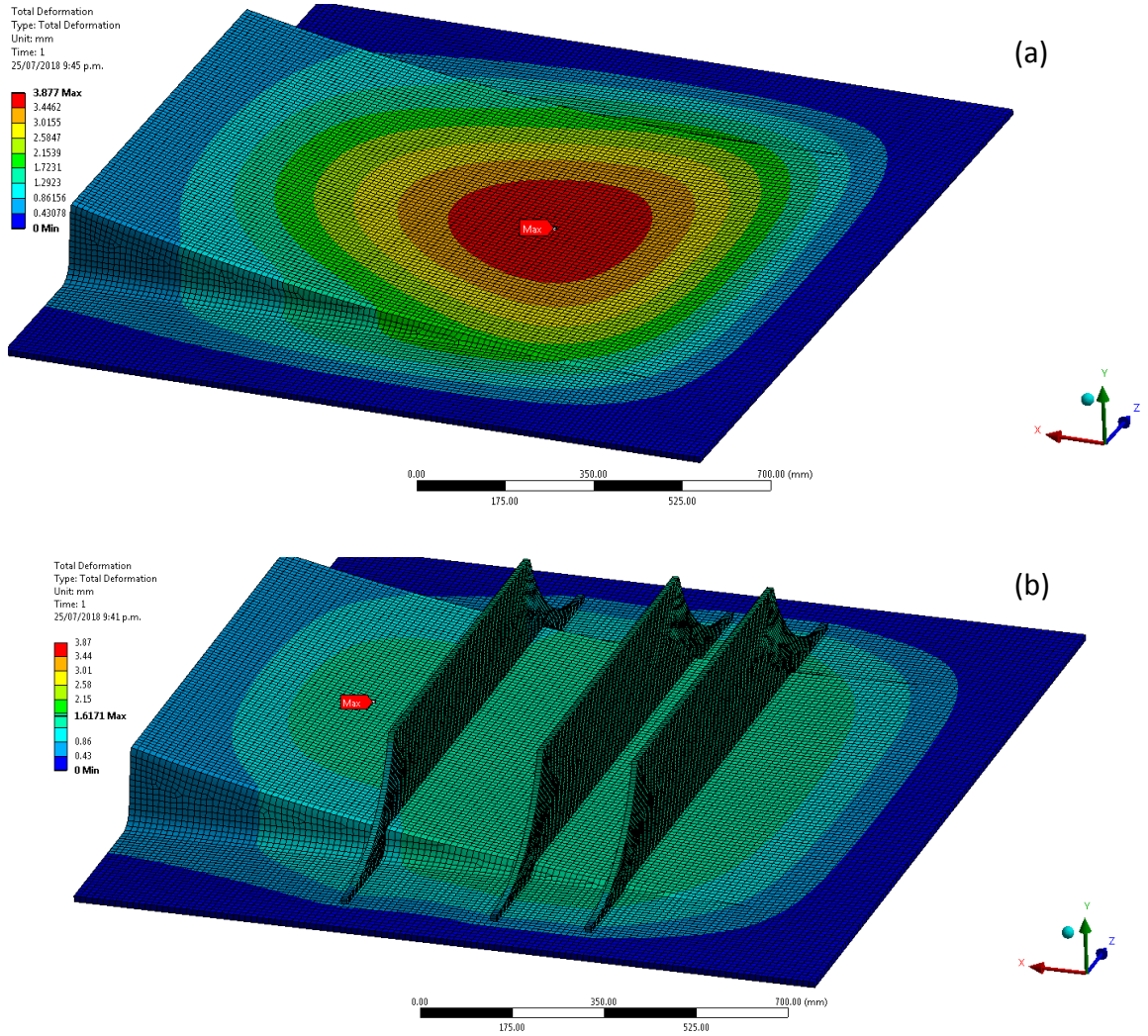

Figure 58. Deflection of the roof-plate: a) before stiffening; b) after stiffening

Orientation of ribs

Vertical orientation of the ribs was found to be acceptable due to its negligible effect (0.27 MPa) on the stress values. This approach simplifies the manufacturing of the stiffened transition duct by providing a straightforward setup, better access for a fabricator, etc.

Lateral extension of plates

Another significant finding of the project was that the stiffening plates must be extended beyond the roof-plate and welded to the bottom plate of the transition duct. Non-extended stiffening plates were proven to have negligible reinforcing effect. However, extension of the ribs should not exceed 140 mm from the side of roof-plate to provide opportunity to an end-customer to trim bottom of the transition duct if it is dictated by hull design or geometry. However, the optimisation study revealed that rib extension resulted in a high

stress concentration area at the joint, which, in turn, appeared to compromise fatigue endurance of the entire transition duct structure.

Shape of termination of rib

Another important contribution of this study was an optimisation of the shape of the stiffening plates in order to reduce, shift or eliminate high stress concentration areas from the joint. Whilst the rectangular shape of the plate (Figure 59a) showed the best results for compensation of the bowing effect (with the maximum displacement of 1.3 mm), the stress concentration at the weld toe was unacceptable with principal stress of 148 MPa.

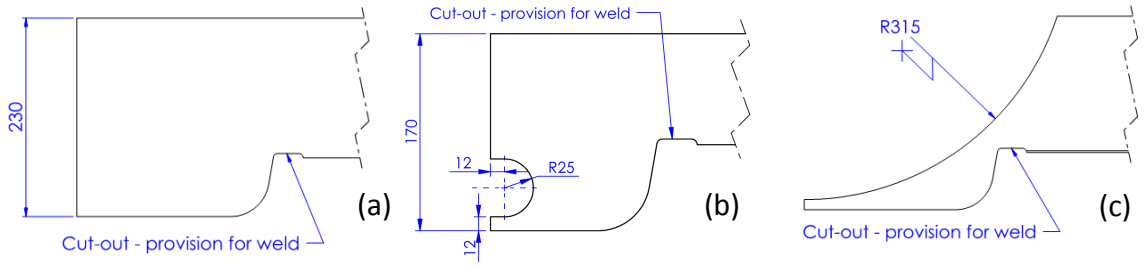

Figure 59. Trialled cut-out for stiffening plates: a) Rectangular shape; b) C-shaped cut-out; b) J-shaped cut-out

Stiffening plate with a C-shaped cut-out (Figure 59b) was also examined. With this type of cut-out, a high stress concentration shifted from welded joints to the curve of the stiffening plate. Although stress concentration was not present at the weld toe anymore, the principal stress in this area was found to be still unacceptably high (70 MPa) to provide sufficient fatigue life. Estimated fatigue life for this solution was below 7 years.

Finally, stiffening plate with J-shape cut-out for the stiffening plate (Figure 59c) was analysed. Similar to C-shape cut-out, stress concentration moved to the curve of the stiffening plate but the maximum stress at the weld toe was reduced to 39 MPa (rounded). This solution showed adequate estimated fatigue life of 22 years and was considered successful.

The shape optimisation study for stiffener plate revealed that any modifications of the stiffening plate geometry have impact on the roof-plate displacement. Hence, every time a shape of the stiffener was adjusted in order to minimise stress distribution around the welds, a new optimisation study was required to find out the optimal stiffening plates

arrangement. As result, the optimum arrangement for stiffening plate with J-shaped cut-out was observed, with dimensions listed in Figure 60:

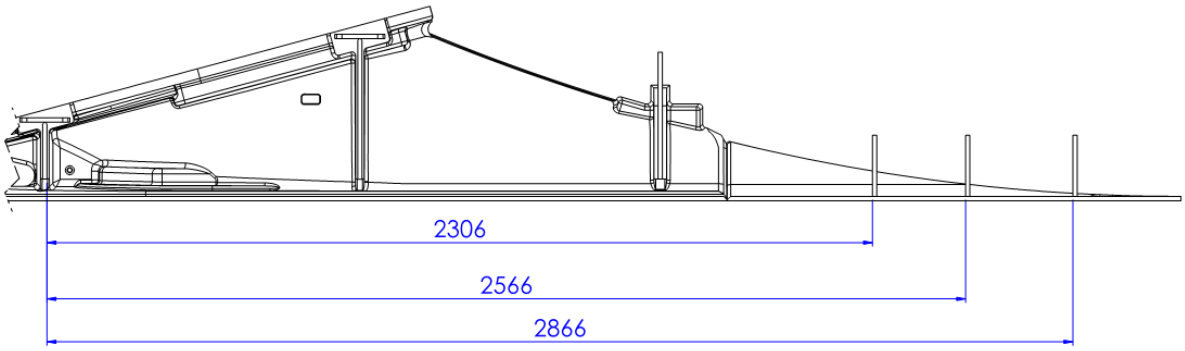

Figure 60. Proposed position of the stiffening plates.

5.1.2 Fatigue life expectation

The expected fatigue life for the roof-plate, which is reinforced by stiffeners with J-shape cut-out was found to be more than 22 years. This value was obtained by using an extremely conservative approach where data for pressure and other loads acting on the roof-plate, were based on extreme jet operational modes. Whilst vessels with such big jets intend to avoid daily operations using maximum power or extreme jet operational modes, it is still important for the manufacturer to cover the worst case scenarios in the endurance calculations.

Additionally, it must be mentioned that the FEA assumption of a rigid fixed support around transition duct led to an artefact of higher stresses at the ends of the stiffeners. Most jet installations in the dockyard tend to join the transition duct directly to the hull membrane. This provides additional stress compliance that reduces the stresses around the welds.

It is likely that life endurance for reinforced roof-plate will exceed 22 years for the majority vessels with HM810 jets.

5.1.3 Weld quality and sample preparation techniques

Validation of the quality of the welds was done by optical microstructure and hardness test. It was found that both areas of interest – fillet type of weld and weld-on-weld region (Figure 61) do not show any abnormalities or defects. Microstructure of welded regions, and shape, orientation and size of the grains were consistent across all samples. These results appeared to be in line with existing literature such as [32].

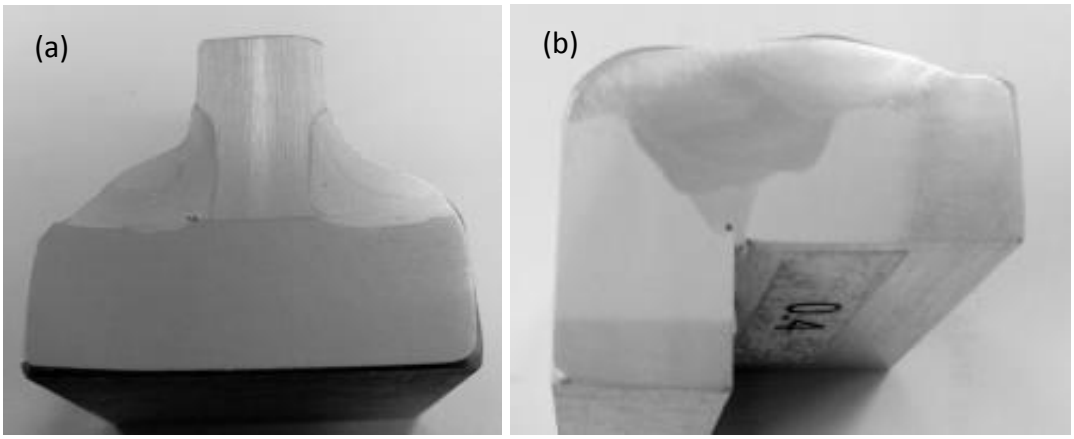

Figure 61. Weld details: a) Fillet weld; b) Weld-on-weld

However, during preparations for optical microstructure it was found that none of the etching methods described in the literature show acceptable results. Hence, the etching techniques were developed for fillet-weld region, which is described in the Table 14, and "dynamic" etching method, which is described in section 3.5.2, for weld-on-weld region.

Similar to microstructure test, the results of hardness were also consistent across all samples. The material hardness of 74.1HV_{10} in weld regions was found to be about 3.4% less than the hardness of parent material with magnitude of 76.6 HV_{10}. Such deterioration of the hardness in the weld region was considered acceptable due to its negligible effect on the welded joints. However, it was noticed that obtained value of the hardness for the base material is 4.25% less than value 80HV (magnitude converted from 75 Brinell hardness scale) specified by BS 485-2:2008. Such difference in base material hardness may be either a result of variances in production and treatment of the material or occur due to measurement errors caused by uncalibrated equipment. Therefore, further structural tests for base material may be recommended to ensure the material complies with the standard.

5.2 Implications of the study

The current study resulted in a number of significant implications for HamiltonJet production practices as well as for installation techniques for the shipyards. The first implication includes regular monitoring of the weld quality at the HamiltonJet production line. It might be done by performing the microstructural testing of the weld regions using techniques developed in this study. Additionally to this implication, quality of the welded structure might be improved by applying the weld toe grinding as advised by DNV-GL

guidelines. This method provides reliable fatigue endurance improvement as well as increasing the reliability of inspection during service life.

The second implication is the importance of obtaining and analysing of the detailed pressure distribution for each jet model. This study revealed that optimum solution for the stiffening roof-plate that includes location, orientation, quantity and geometry of the stiffening plates, directly depends on the knowledge of pressure characteristics that are unique for each jet model.

The third implication of the study is elimination of the additional stiffening of the roof-plate by shipyards at the installation stage. This means, that stiffening plates reliably solve the roof-plate deflection issue and further reinforcement by either joining the ribs with vessel constructional ribs or applying additional ribs, is not required. Furthermore, any unauthorised modifications for the transition duct need to be prohibited as they might deteriorate the fatigue endurance of the duct structure. HamiltonJet defined the locations and features on the jet that need to be used for joining the jet and hull. The only exception to this rule is installation of the jet at the area where vessel bulkhead crosses the jet roof-plate. In this scenario, all necessary modifications must be analysed.

Finally, the hardness test revealed the differences in the hardness properties between samples and technical data for this material. All material used in the production is certified. However, regular re-checking of material quality could benefit the company by eliminating the errors with material supply, stock mix-up, etc.

5.3 Limitations of the work that has been done

The current study had several limitations. Whilst the solution was considered successful, it is important to take into account that all results were based on FE analysis. Validation of the solution by testing real jet structures on the load cycling test rig is very complex and expensive due to jet size and its geometry. Instead, the obtained results were reviewed in detail by the chief engineers and checked against similar studies for other jet models. In parallel, quality of the welding was examined in order to validate material microstructural properties and exclude defects that may cause the failure of the transition duct.

Welded samples were fabricated by highly experienced welders who applied the same techniques and used the Company's current fabrication procedures. The study found that quality of all welds analysed by optical microstructure and hardness tests were appropriate. However, relying on samples produced by one particular welder has its limitations. Whilst Company welders are all ISO 9606-1:2013 certified they could perform welding differently, even following the same procedures. For example, welding travel speed may vary from welder to welder as the procedure does not control welding travel. Another example is control of the temperature of the existing weld pass when the next weld pass is applied. Weld-on-weld techniques on investigated samples were done where temperature of every previous weld pass was ambient (15–22°C). However existing procedures do not prescribe inter-pass temperature control. Therefore, there were no data for what the temperature of the previous weld is before the next weld pass application, in the case of other welders. Additionally, the optimum temperatures for this application as well as minimum or maximum temperature, at which weld quality becomes degraded, were not investigated in the current study.

Finally, there were no CFD data available for the exact effect of roof-plate deflection on the overall jet efficiency. However, based on existing knowledge of the R&D team, the effect from a 4 mm deflection of the roof-plate was considered as significant and required reinforcements.

5.4 Implications for future research

The current study has identified several knowledge gaps and opportunities for further improvement in design and production. One such knowledge gap to be addressed in future research related to the need of obtaining the CFD data for all ranges of the jets for different load cases and jet operation modes. This can strengthen the accuracy of fatigue analysis for the outstanding jet models and optimisation studies for the stiffening of the roof-plate. This, however, can be a time and resource consuming process due to the nature of CFD analysis. It might involve multiple studies that cover all jet models with a variety of load cases, as guided by classifications bodies such as DNV-GL and ABS.

Further studies may also address another knowledge gap related to jet usage. Currently, there appears to be no available data reporting the exact number of cycles of jet for

different operation modes. One of the possible reasons for this knowledge gap is absence of global jet monitoring programmes as jets can be used in many different fields of marine industry. For example, large jets are normally installed on vessels that operate: (a) as ferries with busy steering and rapid speed changes; (b) wind farm service boats with continuous high speed operations; (c) lifesaving and firefighting boats with the jet modes unique for their applications; and (d) coastguard and military vessels, etc. Therefore, collecting of usage data although challenging, could provide a good opportunity to analyse the rigidity of a jet structure in finer details, optimise jet design and provide better service to the end user.

Additional potential research could include studies addressing the production variability of the welding. Current production practices do not always control for (or measure) some potentially important variables such as weld travel speed and material temperature before weld application. This may lead to significant variability of the weld quality. A potential study investigating these variables could analyse current welding practices across all fabrication departments. Key independent variables to include are: travel speed; material pre-heat temperature; operator. Other welding parameters (current, type of weld, etc.) are already set and may not need further consideration. Output variables could be microstructure, particularly grain size and morphology. The necessary etchants have been developed as part of the present study; see section 4.6.1. A design of experiments (DoE) approach might be considered. The benefits of this could be the production of guidelines and weld procedures for improvement of weld quality in critical locations.

6. Conclusion

The original purpose for this study was to determine the optimum arrangement for the stiffeners required to reinforce the transition duct, taking into consideration all loads, ship Classification Society requirements for stress, installation constraints, and manufacturing variables such weld types, weld access and stiffener profiles. Consideration of the duct design by use of FEA shows that the application of three stiffening plates is necessary to reduce deflection. This will also be adequate from a fatigue perspective. The risk of metallurgical damage due to weld-on-weld has been investigated by examination of grain morphology. Results confirm that the microstructure is not significantly adversely affected.

This was confirmed by measurements of hardness. The financial costs have been estimated using a risk management method, and although the input data are highly uncertain, the results favour implementation of the stiffeners solution as it has the potential to avoid risks of warranty claims, boat safety issues, etc.

Original contributions to this work were: (a) application of fluid outputs onto a FEA model in the specific area of transition duct; (b) proof of acceptance of vertical orientation of the stiffeners on curved roof-plate; (c) optimisation of stiffeners arrangement and stiffener geometry that met required fatigue life; (d) development of new etching techniques to reveal microstructure of the aluminium specimens for further optical microstructure examinations.

The study findings also indicate the importance of conducting fatigue analysis for welded joints, and the influence of stiffener geometry on fatigue endurance of the structure.

Additionally, there is a need to better understand to what extent changes in weld practices can contribute to further strengthening of the overall fabrication quality.

It is hoped, therefore, that this study will generate further inquiry into current HamiltonJet practice of the roof-plate stiffening arrangement and geometry.

Summary of design solution

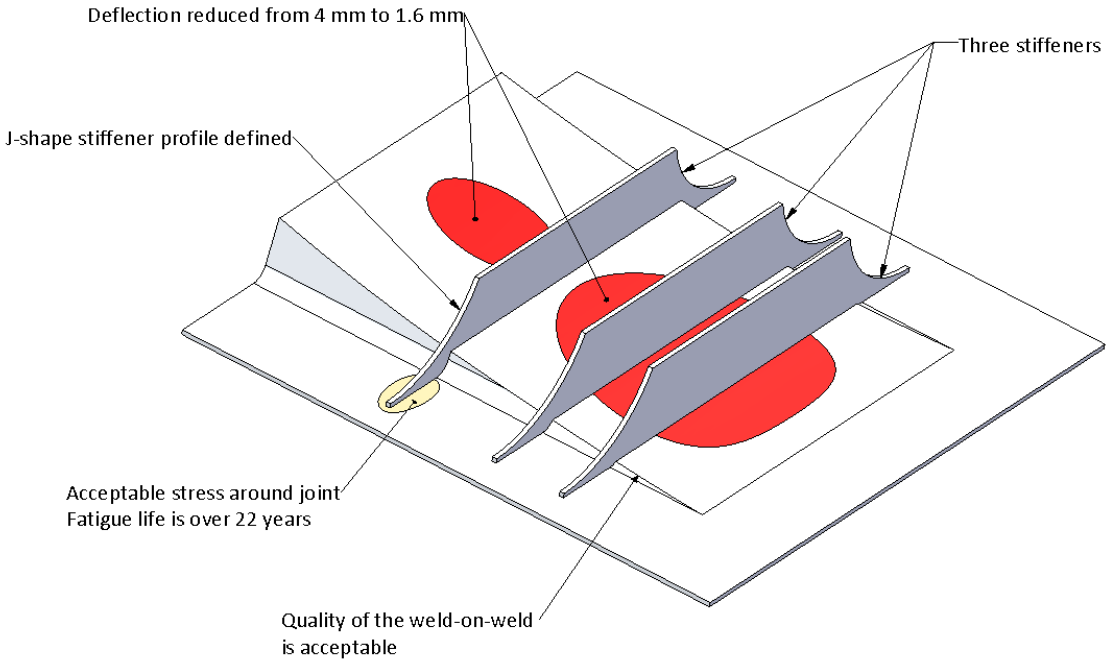

7. Appendix A

7.1.1 A1. Hardness test results

Table 15. Vickers hardness test results for welded region of L-shape samples

	L-sample, HV_{10}			
	L1	**L2**	**L3**	**L4**
1st weld pass (across all samples)	75.2	75.4	73.3	74.5
	76.9	73.0	75.7	73.0
	75.4	75.7	76.3	77.2
Average	***75.8***	***74.7***	***75.1***	***74.9***
2nd weld pass	-	71.3	69.9	68.8
	-	72.4	71.6	68.1
	-	72.1	68.1	65.5
Average	**-**	***71.9***	***69.9***	***67.5***
3rd weld pass	-	-	68.1	68.1
	-	-	65.3	73.6
	-	-	63.6	72.7
Average	**-**	**-**	***65.7***	***71.5***
4th weld pass	-	-	-	67.3
	-	-	-	74.8
	-	-	-	75.4
	-	-	-	75.7
Average	**-**	**-**	**-**	***73.3***

Table 16. Vickers hardness tests results for welded region of T-shape samples

	Tee-untreated sample			
	T5	**T7**	**T6**	**T8**
Weld region	73.9	69.6	75.1	73.9
	68.6	65.3	74.2	71.3
	71.0	68.6	71.6	71.3
Average		***71.2***		

Table 17. Vickers hardness tests results for parent material region across all untreated samples

Parent material region	77.6	76.3	72.9	76.6
	77.9	75.7	75.4	76.6
	79.3	76.6	76.3	78.5
	80.5	75.7	78.5	75.4
	77.5	75.7	75.6	76.6
	77.2	75.4	76.0	75.7
	76.0	77.2	80.3	78.7
	77.2	74.5	76.0	73.9
	79.5	77.3	75.4	73.3
	79.8	77.5	74.8	74.2
Average		***76.6***		

Table 18. Vickers hardness tests results for heat treated samples

Tee - Heat treated samples				
	Weld region		**Parent material region**	
	TH9	**TH10**	**TH9**	**TH10**
	74.2	76.9	76.0	80.5
	72.7	76.3	75.7	75.1
	72.4	71.9	77.2	75.4
	73.1	75.0	77.2	76.6
Average	***74.1***		***76.7***	

7.1.2 A2. Fatigue calculation results

Table 19. Fatigue calculation summary table for proposed solution

Detail		$\Delta\sigma_C$	m_1	m_2	Y_{Ff}	Y_{Mf}	Ahead (b) LD4			Ahead PORT (c) LD2						Ahead STB (c) LD2						Reverse (e), LD1			Usage	Safe Life
										Full Steering			Correction Steering			Full Steering			Correction Steering							
							n_i=	1.46E+05		n_i=	1.44E+05		n_i=	1.57E+07		n_i=	1.44E+05		n_i=	1.57E+07			n_i=	1.46E+05			
							$\Delta\sigma_{Eff}$, (MPa)	N_i	η	$\Delta\sigma_{Eff}$, (MPa)	N_i	η	$\Delta\sigma_{Eff}$, (MPa)	N_i	η	$\Delta\sigma_{Eff}$, (MPa)	N_i	η	$\Delta\sigma_{Eff}$, (MPa)	N_i	η	$\Delta\sigma_{Eff}$, (MPa)	N_i	η	$\Sigma\eta$	Ts
1st Stiffener	P1.1	28	3.4	5.4	1	1	50.3	2.7E+05	5.4E-01	1.5	3.8E+10	3.8E-06	8.1	9.3E+08	1.7E-02	0.6	7.4E+11	1.9E-07	8.3	8.4E+08	1.9E-02	42.5	4.8E+05	3.0E-01	0.87	**22.9**
	P1.2	28	3.4	5.4	1	1	50.3	2.7E+05	5.4E-01	0.4	2.6E+12	5.6E-08	8.3	8.2E+08	1.9E-02	1.8	2.4E+10	6.0E-06	8.1	9.5E+08	1.7E-02	42.5	4.8E+05	3.0E-01	0.87	**22.9**
	P1.3	28	3.4	5.4	1	1	3.5	2.3E+09	6.3E-05	0.2	7.5E+13	1.9E-09	0.6	1.1E+15	1.5E-08	0.2	4.1E+13	3.5E-09	0.6	1.0E+15	1.6E-08	4.8	8.0E+08	1.8E-04	0.00	**81535**
	P1.4	28	3.4	5.4	1	1	3.0	4.0E+09	3.7E-05	0.2	5.0E+13	2.9E-09	0.5	4.6E+15	3.4E-09	0.1	3.0E+15	8.1E-06	0.5	2.9E+15	5.4E-09	2.5	7.1E+09	2.1E-05	0.00	**306016**
2nd Stiffener	P2.1	28	3.4	5.4	1	1	3.0	3.9E+09	3.8E-05	0.0	0.0E+00	0.0E+00	0.5	3.0E+15	5.2E-09	0.0	2.0E+16	0.0E+00	0.5	3.3E+15	4.8E-09	2.9	4.3E+09	3.4E-05	0.00	**279278**
	P2.2	28	3.4	5.4	1	1	3.1	3.7E+09	4.0E-05	0.0	0.0E+00	0.0E+00	0.5	3.0E+15	5.2E-09	0.0	5.8E+18	2.5E-14	0.5	2.8E+15	5.5E-09	3.0	4.1E+09	3.5E-05	0.00	**266847**
	P2.3	28	3.4	5.4	1	1	1.2	1.0E+11	1.5E-06	0.0	0.0E+00	0.0E+00	0.2	5.3E+17	3.0E-11	0.0	6.4E+16	2.3E-12	0.2	6.0E+17	2.6E-11	1.1	1.2E+11	1.2E-06	0.00	**7451887**
	P2.4	28	3.4	5.4	1	1	8.7	1.1E+08	1.4E-03	0.6	9.2E+11	1.6E-07	1.3	1.5E+13	1.0E-06	0.1	1.6E+15	8.8E-11	1.5	9.9E+12	1.6E-06	6.8	2.5E+08	5.9E-04	0.00	**10216**
3nd Stiffener	P3.1	28	3.4	5.4	1	1	43.7	4.4E+05	3.3E-01	2.6	6.3E+09	2.3E-05	6.8	2.3E+09	6.7E-03	0.6	9.6E+11	1.5E-07	7.2	1.8E+09	8.7E-03	32.5	1.2E+06	1.2E-01	0.47	**42.7**
	P3.2	28	3.4	5.4	1	1	43.7	4.4E+05	3.3E-01	0.3	1.2E+13	1.2E-08	7.2	1.7E+09	9.0E-03	3.0	4.0E+09	3.6E-05	6.8	2.5E+09	6.3E-03	32.4	1.2E+06	1.2E-01	0.47	**42.9**
	P3.3	28	3.4	5.4	1	1	18.7	7.9E+06	1.9E-02	0.1	3.9E+14	3.7E-10	3.1	1.7E+11	9.3E-05	0.1	4.3E+14	3.4E-10	3.1	1.7E+11	9.3E-05	18.0	8.9E+06	1.6E-02	0.04	**569**
	P3.4	28	3.4	5.4	1	1	18.3	8.5E+06	1.7E-02	1.7	3.0E+10	4.8E-06	2.8	3.1E+11	5.1E-05	0.2	1.9E+13	7.5E-09	3.1	1.7E+11	9.1E-05	13.3	2.5E+07	5.8E-03	0.02	**866**

For all formulation refer to section 3.4.2

References:

1. Park, W.-G., et al., *Numerical flow and performance analysis of waterjet propulsion system.* Ocean Engineering, 2005. 32(14): p. 1740-1761.

2. Verbeek, R. and N. Bulten. *Recent development in waterjet design*. in Proceedings Rina Waterjet Propulsion Conference. 1998.

3. Allison, J., et al., *Marine waterjet propulsion. Discussion. Author's closure.* Transactions-Society of Naval Architects and Marine Engineers, 1993. 101: p. 275-335.

4. Okamoto, Y., H. Sugioka, and Y. Kitamura, *On the Pressure Distribution of a Water Jet Intake Duct in Self Propulsion Conditions*. 1993.

5. Park, W.-G., et al., *Numerical flow simulation of flush type intake duct of waterjet.* Ocean Engineering, 2005. 32(17): p. 2107-2120.

6. Batchelor, A., *Design and Analysis of Waterjet Intakes: A Thesis Submitted in Partial Fulfilment of the Requirements for the Degree of Master of Engineering in the University of Canterbury*. 2003, University of Canterbury.

7. Griffith-Jones, G.J., *Investigation of incompressible flow through an intake duct with applications to waterjet propulsion*. 1994.

8. Cave, R.L., *CFD Analysis of a Waterjet Intake: A Thesis Submitted in Partial Fulfilment of the Requirements for the Degree of Master of Engineering in the University of Canterbury*. 1998, University of Canterbury.

9. Mununga, L. and I. Huntsman. *Intake Studies for a Waterjet Propulsion System. in IPENZ Conference 98: The sustainable city; Volume 4; Mechanical; IHRAC; general; engineering education.* 1998. Institution of Professional Engineers New Zealand.

10. Takai, T., *Simulation based design for high speed sea lift with waterjets by high fidelity URANS approach*. 2010: The University of Iowa.

11. Eslamdoost, A., L. Larsson, and R. Bensow, *A pressure jump method for modeling waterjet/hull interaction.* Ocean Engineering, 2014. 88: p. 120-130.

12. Kadid, A., *Stiffened plates subjected to uniform blast loading.* Journal of Civil Engineering and Management, 2008. 14(3): p. 155-161.

13. Tavakoli, H.R. and F. Kiakojouri, *Numerical dynamic analysis of stiffened plates under blast loading.* Latin American Journal of Solids and Structures, 2014. 11(2): p. 185-199.

14. Neuberger, A., S. Peles, and D. Rittel, *Scaling the response of circular plates subjected to large and close-range spherical explosions. Part I: Air-blast loading. International Journal of Impact Engineering*, 2007. 34(5): p. 859-873.

15. Crupi, V., et al., *Fatigue analysis of butt welded AH36 steel joints: thermographic method and design S–N curve. Marine Structures*, 2009. 22(3): p. 373-386.

16. Crupi, G., et al., *Fatigue assessment of welded joints using critical distance and other methods.* Engineering Failure Analysis, 2005. 12(1): p. 129-142.

17. El Haddad, M., et al., *J integral applications for short fatigue cracks at notches.* International Journal of Fracture, 1980. 16(1): p. 15-30.

18. Taylor, D., N. Barrett, and G. Lucano, *Some new methods for predicting fatigue in welded joints.* International Journal of Fatigue, 2002. 24(5): p. 509-518.

19. La Rosa, G. and A. Risitano, *Thermographic methodology for rapid determination of the fatigue limit of materials and mechanical components. International journal of fatigue*, 2000. 22(1): p. 65-73.

20. Wang, X., et al., *Quantitative Thermographic Methodology for fatigue assessment and stress measurement. International Journal of Fatigue*, 2010. 32(12): p. 1970-1976.

21. Fargione, G., et al., *Rapid determination of the fatigue curve by the thermographic method.* International Journal of Fatigue, 2002. 24(1): p. 11-19.

22. Veritas, D.N., *Fatigue design of offshore steel structures.* No. DNV-RP-C203, 2010. 30.

23. American Bureau of Shipping, *Fatigue assessment of offshore structures*, A.B.S. Editor. 2003, American Bureau of Shipping Incorporated by Act of Legislature of the State of New York 1862.

24. Bruder, T., et al., *Evaluation of nominal and local stress based approaches for the fatigue assessment of seam welds. International Journal of Fatigue*, 2012. 34(1): p. 86-102.

25. Radaj, D., *Review of fatigue strength assessment of nonwelded and welded structures based on local parameters. International Journal of Fatigue*, 1996. 18(3): p. 153-170.

26. Hobbacher, A., *Recommendations for fatigue design of welded joints and components*. 2009: Springer.

27. Radaj, D., C. Sonsino, and W. Fricke, *Recent developments in local concepts of fatigue assessment of welded joints.* International Journal of Fatigue, 2009. 31(1): p. 2-11.

28. Remes, H. and W. Fricke, *Influencing factors on fatigue strength of welded thin plates based on structural stress assessment. Welding in the World*, 2014. 58(6): p. 915-923.

29. Sonsino, C., et al., *Notch stress concepts for the fatigue assessment of welded joints–Background and applications. International Journal of Fatigue*, 2012. 34(1): p. 2-16.

30. International, A., A.I.H. Committee, and A.I.A.P.D. Committee, *Metals Handbook: Properties and selection*. Vol. 2. 1990: Asm International.

31. Kaufman, J.G., *Introduction to aluminum alloys and tempers*. 2000: ASM international.

32. Liu, Y., et al., *Microstructure and mechanical properties of aluminum 5083 weldments by gas tungsten arc and gas metal arc welding. Materials Science & Engineering* A, 2012. 549: p. 7.

33. L-E, S., et al., *Microstructure and mechanical properties of friction stir welded aluminium alloys with special reference to AA 5083 and AA 6082. Science and Technology of Welding & Joining*, 2000. 5(5): p. 285-296.

34. Behnagh, R.A., M.K. Besharati Givi, and M. Akbari, *Mechanical Properties, Corrosion Resistance, and Microstructural Changes during Friction Stir Processing of 5083 Aluminum Rolled Plates. Materials and Manufacturing Processes*, 2012. 27(6): p. 636.

35. Svensson, L.E., *Microstructure and mechanical properties of friction stir welded aluminium alloys with special reference to AA 5083 and AA 6082. Science and technology of welding and joining*, 2000. 5(5): p. 285-296.

36. Zhang, P., S. Li, and Z. Zhang, *General relationship between strength and hardness.* Materials Science and Engineering: A, 2011. 529: p. 62-73.

37. Mohammadtaheri, M., *A new metallographic technique for revealing grain boundaries in aluminum alloys.* Metallography, Microstructure, and Analysis, 2012. 1(5): p. 224-226.

38. Tamadon, A., et al., *Development of metallographic etchants for the microstructure evolution of A6082-T6 BFSW welds. Metals*, 2017. 7(10): p. 423.

39. Veritas, N., *Strength Analysis of Hull Structures in High Speed and Light Craft*. 1996: Det Norske Veritas.

40. Veritas, D.N., *Classification notes No. 30.7: Fatigue assessment of ship structures.* 2014, Norway.

41. Ghaffarpour, M., et al., *Friction stir welding parameters optimization of heterogeneous tailored welded blank sheets of aluminium alloys 6061 and 5083 using response surface methodology. Proceedings of the Institution of Mechanical Engineers, Part B: Journal of Engineering Manufacture*, 2012. 226(12): p. 2013-2022.